

## REVIEW

# Ferromagnetism of ZnO and GaN: A Review

C. LIU, F. YUN, H. MORKOÇ

*Department of Electrical Engineering and Physics Department, Virginia Commonwealth University, Richmond, VA 23284-3072, USA*

The observation of ferromagnetism in magnetic ion doped II–VI diluted magnetic semiconductors (DMSs) and oxides, and later in (Ga,Mn)As materials has inspired a great deal of research interest in a field dubbed “spintronics” of late, which could pave the way to exploit spin in addition to charge in semiconductor devices. The main challenge for practical application of the DMS materials is the attainment of a Curie temperature at or preferably above room temperature to be compatible with junction temperatures. Among the studies of transition-metal doped conventional III–V and II–VI semiconductors, transition-metal-doped ZnO and GaN became the most extensively studied topical materials since the prediction by Dietl *et al.*, based on mean field theory, as promising candidates to realize a diluted magnetic material with Curie temperature above room temperature. The underlying assumptions, however, such as transition metal concentrations in excess of 5% and hole concentrations of about  $10^{20} \text{ cm}^{-3}$ , have not gotten as much attention. The particular predictions are predicated on the assumption that hole mediated exchange interaction is responsible for magnetic ordering. Among the additional advantages of ZnO- and GaN-based DMSs are that they can be readily incorporated in the existing semiconductor heterostructure systems, where a number of optical and electronic devices have been realized, thus allowing the exploration of the underlying physics and applications based on previously unavailable combinations of quantum structures and magnetism in semiconductors.

This review focuses primarily on the recent progress in the theoretical and experimental studies of ZnO- and GaN-based DMSs. One of the desirable outcomes is to obtain carrier mediated magnetism, so that the magnetic properties can be manipulated by charge control, for example through external electrical voltage. We shall first describe the basic theories forwarded for the mechanisms producing ferromagnetic behavior in DMS materials, and then review the theoretical results dealing with ZnO and GaN. The rest of the review is devoted to the structural, optical, and magnetic properties of ZnO- and GaN-based DMS materials reported in the literature. A critical review of the question concerning the origin of ferromagnetism in diluted magnetic semiconductors is given. In a similar vein, limitations and problems for identifying novel ferromagnetic DMS are briefly discussed, followed by challenges and a few examples of potential devices.

© 2005 Springer Science + Business Media, Inc.

## 1. Introduction

Diluted magnetic semiconductors (DMS), or sometimes referred to as semimagnetic semiconductors, are semi conducting materials in which a fraction of the host cations can be substitutionally replaced by magnetic ions or appropriate rare earths. Much of the attention on DMS materials is due to its potential application in what is now called “spintronics” devices, which exploit spin in magnetic materials along with charge of electrons in semiconductors. Transition metals that have partially filled *d* states (Sc, Ti, V, Cr, Mn, Fe, Co, Ni, and Cu) and rare earth elements that have partially filled *f* states (e.g. Eu, Gd, Er) have been used as magnetic atoms in DMS. The partially filled *d* states

or *f* states contain unpaired electrons, in terms of their spin, which are responsible for them to exhibit magnetic behavior. There are many mechanisms that could be responsible for magnetic ordering. Many of these processes could be in play simultaneously making full scale *ab initio* calculations a must. However, discussion of individual processes, particularly the dominant ones are instructive. In DMS materials the delocalized conduction band electrons and valence band holes interact with the localized magnetic moments associated with the magnetic atoms. Generally, when 3*d* transition-metal ions are substituted for the cations of the host, the resultant electronic structure is influenced by strong hybridization of the 3*d* orbitals of the magnetic ion and

mainly the  $p$  orbitals of the neighboring host anions. This hybridization gives rise to the strong magnetic interaction between the localized  $3d$  spins and the carriers in the host valence band [1]. Due to the necessity that the DMS materials must exhibit ferromagnetism with a critical temperature above room temperature in order to have practical applications in spintronics devices, that temperature, i.e., Curie temperature ( $T_C$ ), is naturally deemed to be the bottleneck issue.

II–VI compounds (such as CdTe, ZnSe, CdSe, CdS, etc.) doped with transition metal ions substituting their original cations are the most common DMSs studied in the early period of this field [1]. The low critical temperatures and to some extent the difficulty in doping these II–VI-based DMSs  $p$ - and  $n$ -type made these materials less attractive for applications. The conventional III–V semiconductors, on the other hand, have been widely used for highspeed electronic devices and optoelectronic devices. The discovery of hole-mediated ferromagnetism in (Ga,Mn)As [2] and heterostructures based on it paved the way for a wide range of possibilities for integrating magnetic and spin-based phenomena with the mainstream microelectronics and optoelectronics as well as taking advantage of the already established fabrication processes. The highest Curie temperature  $T_C$  reported in (Ga,Mn)As grown by molecular beam epitaxy (MBE), however, is  $\sim 170$  K, which sets  $T_C$  higher than room temperature as the major challenge for GaAs-based DMS.

GaN and ZnO have attracted intense attention in the searching for high  $T_C$  ferromagnetic DMS materials since Dietl *et al.* [3] predicted that GaN- and ZnO-based DMSs could exhibit ferromagnetism above room temperature upon doping with transition elements such as Mn (on the order of 5% or more) in  $p$ -type (on the order of  $10^{20} \text{ cm}^{-3}$ ) materials. This in simple terms is in part due to the strong  $p$ - $d$  hybridization, which involves the valence band in the host, owing to small nearest neighbor distance and small spin dephasing *spin-orbit* interaction. Even though the common wisdom indicates hole exchange to be dominant, Sato *et al.* [4] predicted that the ferromagnetic state  $\text{Co}^{2+}(d^7)$  in Co-doped ZnO could be stabilized by  $s$ - $d$  hybridization, pointing to the possibility that high-Curie-temperature ferromagnetic materials could be realized in  $n$ -type ZnO as well. Das *et al.* [5] showed by first-principles calculations that Cr-doped GaN can be ferromagnetic regardless whether the host GaN is of the form of bulk crystal or clusters. These types of predictions, in addition to that by Dietl *et al.*, set off a flurry of intensive experimental activity for transition metal doped GaN and ZnO as potential DMS materials with applications in spintronics.

A number of approaches have been explored to synthesize single-phase (Ga,Mn)N, among which are ion implantation [6], epitaxial growth [7–12], CVD growth of Mn-doped GaN nanowires [13], and diffusion of Mn into GaN templates [14]. Many of the reports indicated ferromagnetic behavior above room temperature for (Ga,Mn)N, and attributed the observation of room temperature ferromagnetism to spin-charge double exchange interaction. On the other

hand, there are also studies [6, 15, 16] which acknowledged the possible presence of some other phases due to the low solubility of magnetic ions in GaN such as ferromagnetic Ga-Mn and ferromagnetic Mn-N alloys, as being responsible for the observations of ferromagnetism. Depending on the various preparation techniques of (Ga,Mn)N, these precipitates might in fact be the major contributors to the total magnetic moment of the samples investigated. Besides Mn-doped GaN, there are also reports on the doping with other transition metal ions in III-nitride materials, such as Mn-doped AlN [17], Cr-doped GaN [18–20], Cr-doped AlN [18, 21, 22], Co-doped GaN [23], Fe-implanted  $p$ -type GaN epilayer [24], Gd-doped GaN films [25], and Vanadium (V) -doped GaN [23]. The solubility of TM elements in GaN is about  $\sim 10\%$  to form single phase solid solution. Most of the reports discussed observation of ferromagnetism or ferromagnetic-like behavior with apparent Curie temperatures near or above room temperature, primarily based on magnetic hysteresis measurements.

For the ZnO family, the solubility of TM elements especially Mn and Co, can reach up to 35% into ZnO. Despite the weight of the predictions supporting only  $p$ -type (Zn,Mn)O leading to ferromagnetism, experimental observations of ferromagnetism for insulating (Zn,Mn)O [26] and  $n$ -type (Zn,Mn)O [27, 28] have been reported by different research groups. Values of  $T_C$  above room temperature have been reported for insulating Co-doped ZnO films [29]. Ando *et al.* [30, 31] reported a large magneto-optical effect in  $\text{Zn}_{1-x}\text{Co}_x\text{O}$  thin films as measured by magnetic circular dichroism (MCD) spectra, suggesting  $\text{Zn}_{1-x}\text{Co}_x\text{O}$  to be suitable as a DMS material, although the  $p$ - $d$  exchange interaction is antiferromagnetic in the samples being studied. By using the same method, a paramagnetic behavior has been observed from a  $\text{Ga}_{1-x}\text{Mn}_x\text{N}$  thin film which showed ferromagnetic hysteresis loop in superconducting quantum interference device (SQUID) measurement [32]. The author postulated that the observed ferromagnetism of the sample arose from an unidentified phase which may not be detectable by the X-ray diffraction. MCD relies on the optical transitions allowed under various optical polarizations involving split off bands due to Zeeman effect which is enhanced by  $sp$ - $d$  exchange interaction, and is discussed in the section dealing with optical properties of ZnO-based DMSs. Ferromagnetism with  $T_C > 300$  K was also observed in  $\text{Zn}_{1-x}(\text{Co}_{0.5}\text{Fe}_{0.5})_x\text{O}$  thin films prepared by magnetron co-sputtering and post annealing in vacuum [33]. However, bulk  $\text{Zn}_{1-x}\text{Co}_x\text{O}$  has been found to be antiferromagnetic in polycrystalline powder samples prepared by both solid-state and liquid-phase reactions [34]. This antiferromagnetic behavior is likely to be associated with the formation of Co clusters observed in  $\text{Zn}_{1-x}\text{Co}_x\text{O}$  powder films, together with the existence of interstitial Co atoms instead of substitutional Co on Zn sites. There are also suggestions based on experimental data [35] which show that homogeneous films of  $\text{Zn}_{1-x}\text{Co}_x\text{O}$  which are preferred for device applications tend to exhibit spin-glass behavior, whereas inhomogeneous  $\text{Zn}_{1-x}\text{Co}_x\text{O}$  films are more

likely to demonstrate room-temperature ferromagnetism, suggesting perhaps that Co clusters might be the source of the purported high  $T_C$  ferromagnetism in  $\text{Zn}_{1-x}\text{Co}_x\text{O}$ .

The mechanisms responsible for ferromagnetism, particularly early on, have not been fully understood and appreciated. The theory dealing with ferromagnetism driven by the exchange interaction between carriers and localized magnetic ions was first proposed by Zener [36–38]. The theory indicates that direct superexchange between the magnetic ions is not ferromagnetic but the indirect superexchange involving carrier mediation is. Therefore, the features of DMS are induced by the exchange interaction between localized  $d$  shell electrons of the magnetic ions and the delocalized band carrier states ( $s$  or  $p$  origin). Only in recent years have a large number of theoretical efforts have been undertaken to explain the detailed exchange mechanisms. Models based on the mean-field theory, first principle calculations, and bound magneton polaron, etc., all have been developed to account for the magnetic properties observed experimentally, although each has its own limitations. Due to the complexity of the DMS systems based on GaN and ZnO and especially the possible presence of secondary phase precipitates, it is still difficult to find a universal theory, other than possibly full blown numerical *ab initio* calculations, to explain all the phenomena, such as the wide range of  $T_C$ , i.e. 10 to 940 K, observed in (Ga,Mn)N. It also should be mentioned that although both GaN and GaAs are III–V systems, the location of Mn  $d$  state levels are quite different in these two host materials. The Mn  $d$  levels are below the valence band minimum of GaAs, but are deep in the GaN band gap. This would require substantial modifications to existing simple theories in order for them to successfully describe ferromagnetism in GaN and also in ZnO, since the nature of the hybridization of the Mn  $3d$  states and host  $p$ -states strongly depends on their relative position in the band structure. It is fair to state that, the state of transition metal-doped GaN and ZnO systems is still in its infancy, and it is too early to give a definitive description of the exact mechanism(s) governing the experimental observations regarding the origin of reported magnetization behavior. In addition, it is just as equally fair to state that the more stringent methods need to be brought to bear for supporting the conclusions reached on the experimental side.

This review describes the basic theories forwarded for the mechanisms involving DMS, delving into the theoretical results specific to ZnO and GaN. A good deal of the body of this review is devoted to reviewing the structural, optical, and magnetic properties of ZnO- and GaN-based DMSs reported in the literature. A critical review of the question of the origin of ferromagnetism in dilute magnetic semiconductors is given. In a similar vein, limitations and problems for identifying novel ferromagnetic DMS are discussed, followed by challenges and potential devices. Even though an earnest effort was made to be self sufficient, it had to be assumed that the reader has the basic background in the field of semiconductors and magnetic properties

of transition metal doped semiconductors. If needed, additional basics and background knowledge can be found in several text books [39, 40]. Additional data and discussion can also be found in other reviews on DMS [1, 41, 42] and its applications to spintronics [43–45]. Some of the reviews cover areas spanning from the fundamental physics of DMS to spin-related device operation principles expected of the well-known DMS systems as well as novel materials. This current review focuses only on GaN and ZnO, and aims at providing the *present status* of these exciting DMS systems still under development, including their synthesis, magnetic properties, microstructural analyses, and electrical properties pertaining to spin-related applications. For a semblance of completeness a tutorial section of the theoretical models dealing with the mechanisms of ferromagnetism in these DMS material systems is also presented. Only a few prototype devices utilizing the spin transport characteristics of III-nitride and ZnO DMS systems are briefly discussed, followed by some words on the future possibility of monolithic integration of spintronics and microelectronics.

## 2. A synopsis of DMS theory

In dilute magnetic semiconductors a sizable portion of atoms (as much as 36% of Mn in ZnO) is randomly substituted by transition-metal (TM) elements, giving rise to localized magnetic moments in the semiconductor matrix. The presence of magnetic ions affects the free carrier behavior through the  $sp$ - $d$  exchange interaction between the localized magnetic moments and the spins of the itinerant carriers [1]. TM elements have valence electrons corresponding to the  $4s$  orbital, and have partially filled  $3d$  shells, thus the name  $3d$  transition metals (i.e. Mn with the shell structure of  $1s^2 2s^2 2p^6 3s^2 3p^6 3d^5 4s^2$ ). Both GaN and ZnO are of wurtzite structure which is formed by tetrahedral ( $s$ - $p^3$ ) bonding. Generally,  $3d$  transition-metal ions substitute for the cations of the host semiconductors, i.e., Zn sites in ZnO and Ga sites in GaN. In ZnO, the particular transition-metal element, for example, Mn, contributes its  $4s^2$  electrons to the  $s$ - $p^3$  bonding, and can therefore substitutionally replace the Zn in the tetrahedral bonding to form a  $\text{TM}^{2+}$  charge state. In GaN, the bonding configuration requires 3 electrons which can be satisfied with the transition-metal elements contributing three electrons and form  $\text{TM}^{3+}$  ( $3d^4$  for Mn) charge states. However, depending on the position of the Fermi level, which is generally near the conduction band in GaN, the third electron may be obtained from a donor site resulting in a large binding energy without leaving any corresponding hole in the valence band. This means that both  $\text{TM}^{2+}$  ( $3d^5$  for Mn) and  $\text{TM}^{3+}$  ( $3d^4$  for Mn) states might be possible and co-exist in GaN. Photoluminescence (PL) and PL excitation (PLE) spectra bear this out as discussed in the section dealing with experimental results in GaN.

The  $3d$  band of the  $\text{Mn}^{2+}$  ion is exactly half-filled with 5 electrons among the 10 available states, with an energy gap between the up-spin ( $\uparrow$ ) occupied states and

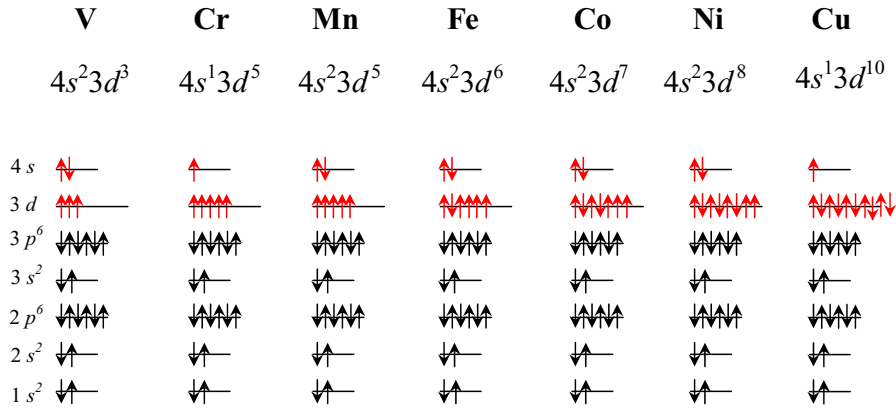


Figure 1 Electronic configuration of the 3d-states and 4s-states of transition metal elements (from V to Cu).

empty down-spin ( $\downarrow$ ) states. For other transition metals, such as Fe, Co, Ni, one of the bands is usually partially filled (up or down), as shown in Fig. 1. Table I shows the oxidation and charge states for some of the transition metals in ZnO and GaN [46]. The TM- $d$  bands of the transition metal hybridize with the host valence bands (O- $p$  bands in ZnO and N- $p$  bands in GaN) to form the tetrahedral bonding. This hybridization gives rise to the exchange interaction between the localized 3d spins and the carriers in the host valence band. In this simple picture, the  $s$  band of the conduction band does not mix with the TM- $d$  bands, but it is still influenced by the magnetic ion.

The important characteristic of a ferromagnetic material is the spontaneous magnetization below the Curie temperature, also referred to as the critical temperature. As shown in Fig. 2 in ferromagnetic materials [47], the  $d$

band is divided into spin-up and spin-down sub-bands, and the up and down states are displaced in energy with respect to one another, so that the spin-up band is filled first, and the spin-down states contain the remaining, if any, electrons. The difference in the number of spin-up and spin-down electrons gives rise to the observed spontaneous magnetic moment. Above  $T_C$ , the ferromagnetic material loses its permanent magnetism due to thermal agitations. In order to have practical applications in functional devices, it would be desirable to have a Curie temperature well above room temperature. Further for some device applications, it is also desirable to have the ferromagnetism to be due to carrier-induced ferromagnetism, so that the magnetic properties of the DMS can be manipulated by external means such as through manipulation of the hole concentration. A better understanding of the underlying mechanisms will certainly provide the much needed guidance for material design. In order to gain insight to the processes involved, a brief tutorial of the recently proposed mechanisms for ferromagnetism in DMS materials is presented in this section. A more detailed treatment of the theoretical results from recent literature about the mechanism of ferromagnetism in TM-doped ZnO and GaN then follows.

In a nutshell, the mechanisms pertinent to magnetism are direct superexchange (antiferromagnetic), indirect superexchange (could be ferromagnetic), carrier-mediated exchange (ferromagnetic) including the much celebrated double exchange mechanism, and magnetic polarons, to cite a few.

In the Zener model, the direct interaction between  $d$  shells of the adjacent Mn atoms (*superexchange*) leads to an antiferromagnetic configuration of the  $d$  shell spins because the Mn- $d$  shell is half-filled. On the other hand, the indirect coupling of spins through the conduction electrons tends to align the spins of the incomplete  $d$  shells in a ferromagnetic manner. It is only when this dominates over the direct superexchange coupling between adjacent  $d$  shells that ferromagnetism is possible. Accordingly, the mean-field approach assumes that ferromagnetism occurs through interactions between the local moments of the Mn atoms mediated by free holes in the material. The spin-spin coupling is also assumed to be a long-range interaction, allowing the use of a mean-field approximation. The mean-field

TABLE I Expected oxidation and charge state of some candidate transition metals in ZnO and GaN. Neutral state is referred as the same charge state as that of the cation in the host material, such that  $\text{Mn}^{2+}$  is the neutral state in ZnO, whereas  $\text{Mn}^{3+}$  is the neutral state in GaN. The electron configuration for each charge state is given in the first row (after T. Graf *et al.*, ref. 46)

ZnO	$3d^3$	$3d^4$	$3d^5$	$3d^6$	GaN
Acceptor (negative charge)			$\text{Cr}^+$	$\text{Mn}^+$	
Neutral		$\text{Cr}^{2+}$	$\text{Mn}^{2+}$	$\text{Fe}^{2+}$	Acceptor
Donor (positive charge)	$\text{Cr}^{3+}$	$\text{Mn}^{3+}$	$\text{Fe}^{3+}$		Neutral
Double donor ( $2^+$ charge)	$\text{Mn}^{4+}$	$\text{Fe}^{4+}$			Donor

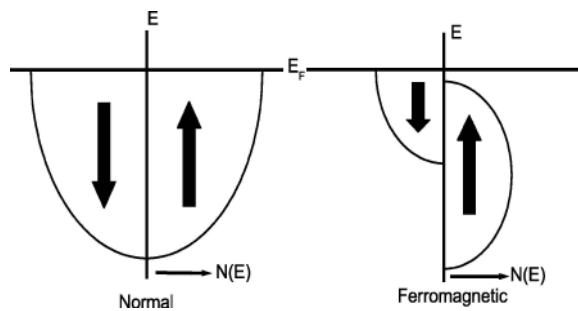


Figure 2 A schematic representation of the density of electronic states available to electrons in a normal metal and in a ferromagnetic metal whose majority spin states are completely filled.  $E$  is the electron energy;  $E_F$  is the Fermi level; and  $N(E)$  is density of states. (Reprinted with permission from ref. 47. Copyright 1998 AAAS.)

model calculates the effective spin-density due to the Mn ion distribution. The direct Mn-Mn interactions are antiferromagnetic so that the Curie temperature, for a given material with a specific Mn concentration and hole density (derived from Mn acceptors and/or intentional shallow level acceptor doping), is determined by a competition between the ferromagnetic and antiferromagnetic interactions.

Early attempts to understand the magnetic behavior of DMS systems are based on models in which the local magnetic moments are assumed to interact with each other via Ruderman-Kittel-Kasuya-Yoshida type (RKKY) interactions. The basic idea behind the RKKY interaction is based on the exchange coupling between the magnetic ion and the conduction band electrons. It should be mentioned that *s* and *d* wavefunctions are orthogonal and would not lead to any interaction in perfect one electron system. The conduction electron is magnetized in the vicinity of the magnetic ion, with the polarization decaying with distance from the magnetic ion in an oscillatory fashion. This oscillation causes an indirect superexchange interaction (RKKY) between two magnetic ions on the nearest or next nearest magnetic neighbors. This coupling may result in a parallel (ferromagnetic) or an anti-parallel (antiferromagnetic) setting of the moments dependent on the separation of the interacting atoms. The RKKY interaction between Mn spins via delocalized carriers has been used to explain the ferromagnetism observed in PbSnMnTe [48]. However, if the carriers come from Mn-*d* states and are localized, which are far from being free-electron-like, the RKKY interaction may not be realistic.

The mean-field Zener model proposed by Dietl *et al.* [3] has been successful in explaining the transition temperatures observed for *p*-(Ga,Mn)As and (Zn,Mn)Te. The meanfield Zener theory is based on the original model of Zener [36] and the RKKY interaction. As compared to the RKKY interaction, the mean-field Zener model takes into account the anisotropy of the carrier-mediated exchange interaction associated with the spin-orbit coupling in the host material. In the process it reveals the important effect of the spin-orbit coupling in the valence band in determining the magnitude of the  $T_C$  and the direction of the easy axis in *p*-type ferromagnetic semiconductors. Based on this model, it was predicted that TM-doped *p*-type GaN and ZnO, as shown in Fig. 3, are the most promising candidates for ferromagnetic DMS with high Curie temperature. However, these predications are made on the incorporation of some 5% transition metal element and hole concentrations of above  $10^{20} \text{ cm}^{-3}$ . Notwithstanding these seemingly yet to be demonstrated high hole concentration (may in fact never be attainable) this prediction stimulated a plethora of activity to achieve high Curie temperature ferromagnetism by using ZnO and GaN-based DMSs.

Sato and Katayama-Yoshida [49] performed first principles *ab initio* calculations of the electronic structures of TM-doped ZnO and proposed the double exchange mechanism for the carrier-induced ferromagnetism. The double exchange mechanism has been

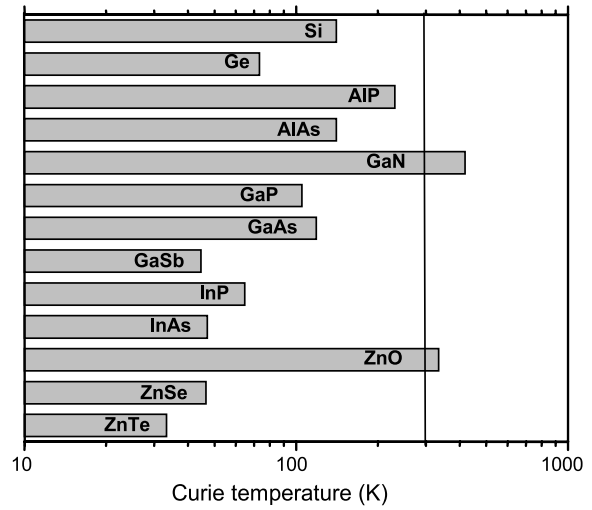


Figure 3 Predicted Curie temperatures as a function of the band gap. Computed values of the Curie temperature  $T_C$  for various *p*-type semiconductors containing 5% of Mn and  $3.5 \times 10^{20}$  holes per  $\text{cm}^3$ . (Reprinted with permission from ref. 3.)

successfully used to explain the ferromagnetism observed in (In,Mn)As [50, 51]. In the double exchange mechanism originally proposed by Zener [37] magnetic ions in different charge states couple with each other by virtual hopping of the 'extra' electron from one ion to the other. In the DMS material, if neighboring TM magnetic moments are in the same direction, the TM-*d* band is widened by the hybridization between the up-spin states. Therefore, in the ferromagnetic configuration the band energy can be lowered by introducing carriers in the *d* band. In these cases, the 3*d* electron in the *partially* occupied 3*d*-orbitals of the TM is allowed to hop to the 3*d*-orbitals of the neighboring TM, if neighboring TM ions have parallel magnetic moments. As a result, the *d*-electron lowers its kinetic energy by hopping in the ferromagnetic state. This is the so-called double exchange mechanism. The detailed mechanism of double exchange will be revisited in the discussion of theoretical studies in TM-doped GaN. Table II gives a brief comparison of the main features of the above mentioned magnetic interactions.

TABLE II A comparison of magnetic interactions

Interaction	Definition
RKKY	Indirect exchange coupling of magnetic moments over relatively large distance via band electrons due to the Coulomb exchange. It becomes efficient when a high concentration of free carriers is present such as in metals for which it was developed.
Direct superexchange	Direct coupling of magnetic ions through overlap of magnetic orbitals
Indirect superexchange	Spins of two magnetic ions are correlated due to the exchange interaction between each of the two ions and the valence <i>p</i> -band.
Double exchange	Couples magnetic ions in different charge state by virtual hopping of the 'extra' electron from one ion to the other through interaction with <i>p</i> -orbitals.

With due reverence and deference to the models mentioned above, it is becoming increasingly clear that a true picture can only be obtained by performing first principles calculations. For example, it is stated that the mean-field theory overestimates the critical temperature substantially when the magnetic ion density is small. It is also becoming clear that in Mn doped GaN magnetic ion concentration has a profound effect on the way the Mn levels split and whether the ferromagnetic or antiferromagnetic state is stable. Having made the case for *ab initio* calculations, in the first principles approach the total energy and electronic structures is calculated by using the density functional theory (DFT). At temperature  $T = 0$  K, the ground state structure of the system corresponds to a minimum of the total energy. DFT [52, 53] is a successful approach for the description of ground state properties of metals, semiconductors, and insulators. Implementation of DFT is based on approximations for the exchange-correlation potential, which arises from the overlap of the electron wave functions due to chemical bond formation. One effective and common approximation is the local (spin) density approximation (LDA) which locally allows substitution of the exchange-correlation energy density of an inhomogeneous system by that of an electron gas evaluated at the local density, and generalized gradient approximation (GGA) which locally substitutes the exchange-correlation energy density by that of an electron gas evaluated at the local density and its gradient and higher terms. The magnetic state of the DMSs can be investigated by calculating the electronic structure of a ferromagnetic DMS (all the magnetic moments of TMs are parallel to each other) and that of a spin glass like (or antiferromagnetic, when magnetic moments of TM point randomly with respect to each other) DMS. The total energy (TE) is calculated for both states as a function of transition-metal density. Then,  $\Delta E = \text{TE}(\text{spin glass}) - \text{TE}(\text{ferromagnetic state})$  is calculated to determine the stability of the ferromagnetic state, i.e., when  $\Delta E$  is positive, the ferromagnetic state is more stable than the spin glass state.

The first principles calculations predict that transition metals V, Cr, Fe, Co, and Ni-doped ZnO [54] showed ferromagnetism with concentration from 5 to 25%, whereas the Mn-doped ZnO shows spin glass state at ground state because of the exact half-filled  $d^5$  state of Mn ions [49]. For comparison,  $\text{V}^{2+}$ ,  $\text{Cr}^{2+}$ ,  $\text{Fe}^{2+}$ ,  $\text{Co}^{2+}$ , and  $\text{Ni}^{2+}$  have  $d^3$ ,  $d^4$ ,  $d^6$ ,  $d^7$  and  $d^8$  electronic configurations, respectively. The ferromagnetic state in Mn-doped ZnO is stabilized by hole doping shown schematically in Fig. 4, due to the double exchange mechanism. The calculated total energy difference between the spin glass state and the ferromagnetic state obtained for 25% V-doped ZnO is 1.36 mRy, which is very large compared to that of 0.12 mRy for 5% Mn-doped GaAs. Suppose the total energy difference is a good estimate for  $T_C$ , and taking the experimental  $T_C$  of 110 K in 5% Mn-doped GaAs into consideration, high- $T_C$  is suggested for V-, Cr-, Fe-, Co-, and Ni-doped ZnO [54].

In addition to the models mentioned above, an alternative model considers whether ferromagnetic ordering

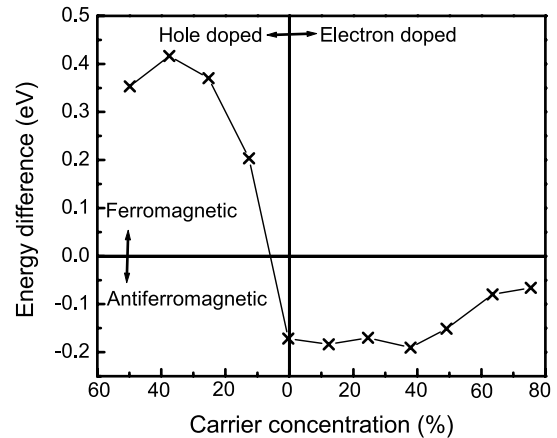


Figure 4 Stability of the ferromagnetic ordering of Mn magnetic moments in ZnO. The energy difference of  $\Delta E = \text{TE}(\text{spin glass}) - \text{TE}(\text{ferromagnetic})$  is plotted as a function of carrier concentration. The carrier concentration means  $N$  (hole doping) and Ga (electron doping) concentration in the supercell (after ref. 49).

of the Mn moments could originate from carriers (holes) that are present in the material, but localized at the transition-metal impurity [55, 56]. Furthermore, ferromagnetism in DMS has been accounted for by the formation of bound magnetic polaron (BMP) [55–62]. The bound magnetic polarons are formed by the alignment of the spins of many transition-metal ions with that of much lower number of weakly bound carriers such as excitons within a polaron radius. The basic idea is schematically illustrated in Fig. 5. The localized holes of the polarons act on the transition-metal impurities surrounding them, thus producing an effective magnetic field and aligning all spins. As temperature decreases the interaction distance (boundary) grows. Neighboring magnetic polarons overlap and interact via magnetic impurities forming correlated clusters of polarons. One observes a ferromagnetic transition when the size of such clusters is equal to the size of the sample. This model is inherently attractive for low carrier density systems such as many of the electronic oxides.

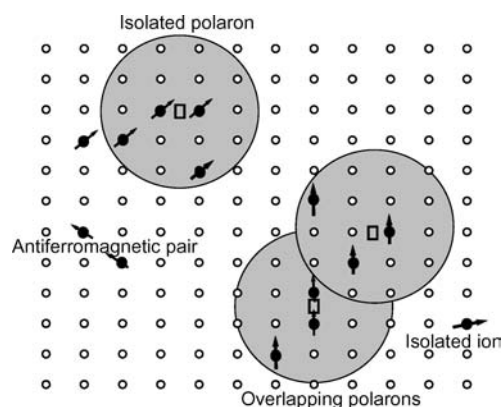


Figure 5 Representation of magnetic polarons. A donor electron couples its spin antiparallel to impurities with a half-full or more than half-full 3d shell. The figure is drawn for magnetic cation concentration  $x = 0.1$  and when the orbital radius of the magnetic cation is sufficiently large. Cation sites are represented by small circles. Oxygen is not shown; the unoccupied oxygen sites are represented by squares. (Reproduced with permission from ref. 61. Copyright 2005 Nature Publishing Group.)

The polaron model is applicable to both *p*- and *n*-type host materials [58]. Even though the direct exchange interaction of the localized holes is antiferromagnetic, the interaction between bound magnetic polarons may be ferromagnetic for sufficiently large concentrations of magnetic impurities. This enables ferromagnetic ordering of the Mn ions in an otherwise insulating or semi-insulating material.

### 3. Theoretical results of TM-doped ZnO and GaN

The critical temperature in the III-arsenide DMSs is still low to have significant substantial practical impact, fuelling the quest for room-temperature ferromagnetism which has been reported in most of magnetically doped nitrides and oxides semiconductors as reviewed in the subsequent section. It should be mentioned that the process is rather complex and the experiments are not quite as clear cut as one would like them to be which breeds some degree of controversy. Recent theoretical treatments have yielded useful insight into fundamental mechanisms involved in ferromagnetism, but there is still inconsistency between the theoretical and experimental results, and also among the various theories as well as among the experiments. From both the theoretical and experimental points of view, this field is still at the beginning of the road toward understanding and controlling magnetism in these systems. There seems, however, to be agreement that first principles calculations are more definitive.

As mentioned in the synopsis section regarding various theories, there are a number of existing models for the observed magnetism in diluted magnetic semiconductors. Mean-field theory assumes ferromagnetic correlations mediated by holes from shallow acceptors in a matrix of localized spins. Dietl *et al.* [3, 63–65] have applied the Zener model with a proper description of the valence band structure to determine the value of the Curie temperature in GaAs:Mn. The model takes

into account the anisotropy of the carrier-mediated exchange interaction related to the spin-orbit coupling in the host material. The Curie temperature is proportional to the density of Mn ions and hole density. This model suggests that GaN and ZnO might exhibit critical temperatures above 300 K due to the small spin-orbit coupling, provided that a sufficiently high hole density can be achieved ( $10^{20} \text{ cm}^{-3}$ ), which is much higher than that achieved so far or achievable in both semiconductors. The source of holes does not necessarily have to be the TM ions. However, the need to incorporate as many magnetic ions as possible is not consistent with adding other acceptor like impurities as both compete for the same cation site and end up reducing the magnetic ion concentration. According to mean-field theories it is difficult to achieve ferromagnetism in *n*-type semiconductors due to the generally smaller *s-d* interaction. Mean-field theory usually overestimates the stability of ordered phases, which may lead to overly optimistic predictions of the critical temperature [66].

In addition to Dietl *et al.*'s predictions, ferromagnetism in magnetic ion doped ZnO has been theoretically investigated by density functional theory calculations. The various methods, i.e., different approximation used for the exchange and correlation energies, are listed in Table III.

Sato *et al.* first applied *ab initio* calculations based on the local density approximation [49, 54, 67–70] to study TM-doped ZnO. With the exception of Mn, transition metals V, Cr, Fe, Co, and Ni-doped ZnO show ferromagnetism with concentration ranging from 5 to 25%, as shown in Fig. 6 [54]. The magnetism in the ZnO-based DMSs under both *n*- and *p*-type carrier doping treatment has been investigated [4, 71]. The results show that ferromagnetism was induced by hole doping in the Mn-doped ZnO, but found no effect of electron doping. In (Zn,Mn)O, the Mn impurity has a  $d^5$  electron configuration due to the substitution of  $\text{Zn}^{2+}$  by  $\text{Mn}^{2+}$  ion, so that there is no itinerant carrier. In this case, it is suggested that the antiferromagnetic superexchange

TABLE III A comparison of different methods in DFT calculation to approximate exchange-correlation energy

Method	Definition	Assumptions	Advantages	Limitations
DFT	Density functional theory	Uses the charge density as the fundamental system variable, and describes the ground state properties by using certain functional of the charge density	Simply the many body problem by using the electron charge density as fundamental variable rather than the wavefunction	Applicable only for the ground state, needs approximation for exchange-correlation energy functional
Approximation for exchange-correlation energy				
LDA	Local density approximation	For regions of a material where the charge density is slowly varying, the local charge density can be considered to be the density of an equivalent uniform homogeneous electron gas.	Simple and produces moderately accurate results in most cases.	Underpredict atomic ground state energies and ionization energies, and overpredicts binding energies
GGA	Generalized gradient approximation	Locally substitutes the exchange-correlation energy density by that of an electron gas evaluated at the local density and its gradient and higher terms	Yield improvement over LDA in the description of finite systems	Overcorrects the lattice constant for semiconductor systems compared to LDA
B3LYP	Becke three parameter Lee-Yang-Parr	Uses hybrid exchange energy functionals and gradient-corrected correlation functionals	The most popular DFT method. Produces more accurate results	Occasional large errors



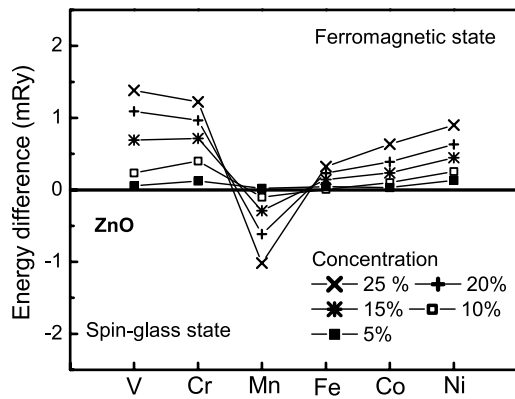


Figure 6 The stability of the ferromagnetic states in ZnO-based DMSs. V, Cr, Mn, Fe, Co or Ni is doped as a magnetic impurity. The vertical axis is the energy difference per one formula unit between the ferromagnetic and the spin glass state. A positive energy difference indicates that the ferromagnetic state is more stable than the spin glass state. (Reprinted with permission from ref. 54. Copyright 2001 Elsevier.)

interaction between Mn ions stabilizes the spin glass state. On the other hand,  $V^{2+}$ ,  $Cr^{2+}$ ,  $Fe^{2+}$ ,  $Co^{2+}$ , and  $Ni^{2+}$  have  $d^3$ ,  $d^4$ ,  $d^6$ ,  $d^7$  and  $d^8$  electronic configurations, respectively. In the case of Cr, one  $4s$  electron and one  $3d$  electron precipitate in bonding in the II–VI divalent environment and is therefore left in the  $Cr^{2+}(d^4)$  state. Therefore, the  $3d$ -band of up-spin states or down-spin states in these elements is not fully occupied. In mean-field theory and other theories, ferromagnetism arises from a competition between the double exchange interaction and the antiferromagnetic superexchange interaction in these materials. When ZnO:Mn is doped with nitrogen ( $1s^2 2s^2 2p^3$ ), holes are itinerant in keeping with their  $d$ -character due to the large hybridization of the N- $2p$  states with the Mn- $3d$  states. Therefore, the kinetic energy is lowered so efficiently that the ferromagnetic state is stabilized by the double exchange mechanism. On the other hand, when the system is doped with donors, the doped electrons never go into the Mn- $3d$  states but into the host conduction band, therefore, the double exchange mechanism does not act to stabilize the ferromagnetism in (Zn,Mn)O.

Other first-principle calculations suggested that the  $n$ -type doping in ZnO can increase the Curie temperature of Fe-, Co- and Ni-doped samples when the effects of disorder are taken into account by the coherent potential approximation (CPA) [71]. This reference has a detailed review of the first principles calculations of II–VI compound-based and III–V compound-based DMSs as well. Considering that the  $n$ -type ZnO is readily available and the intrinsic defects such as O-vacancies and Zn-interstitials form donor states, it is concluded that (Zn,Fe)O, (Zn,Co)O and (Zn,Ni)O are promising candidates for high- $T_C$  ferromagnets. The authors [71] also suggested that (Zn,Mn,Fe)O, (Zn,Mn,Co)O, or (Zn,Mn,Ni)O may show carrier-induced ferromagnetism with electron doping by tuning the ratio of Mn to Fe, Co or Ni. This point might warrant experimental investigations and requires specific designs for ferromagnetism. Recently Sharma *et al.* [72] reported on the *ab initio* total energy calculations within GGA, and predicted a ferromagnetic ground state for

(Zn,Mn)O with Mn composition of 4.2%, and antiferromagnetic ground state for Mn composition above 5%, which is consistent with the results obtained by Sato *et al.* [71]. The ferromagnetism above room temperature was also observed experimentally in both bulk and thin film forms of  $Zn_{1-x}Mn_xO$  with  $x < 4\%$  [72].

The local spin density approximation and coherent potential approximation used in the first principles calculation may not be adequate to handle the strong correlation and lattice relaxations. This is particularly so for thin films prepared by different deposition techniques under non-equilibrium conditions. In (Zn,Mn)O, the  $3d$  electron on-site Coulomb interaction  $U$  is estimated to be 5.2 eV, which is comparable to the 6.0 eV value in MnO [73]. This means that the correlation effects should be taken into account in the theoretical treatments, which leads to the generalized gradient +  $U$  (GGA+ $U$ ) scheme, or the local spin density approximation +  $U$  (LSDA+ $U$ ) scheme.

Ferromagnetism in  $3d$  transition metal-atom-doped ZnO has been investigated by *ab initio* electronic structure calculations based on the GGA and GGA +  $U$  approximations [74]. The results are quite different from those reported by Sato *et al.* [49] in that Mn, Co, or Cu-doped ZnO are ferromagnetic semiconductors with Mn-doped ZnO having the maximum magnetic moment, while other TM-doped ZnO are metallic. The electronic structures and magnetism of several  $3d$  and  $4d$  transition metal-doped ZnO ( $TM_{0.25}Zn_{0.75}O$ : TM = Ti, Cr, Mn, Fe, Co, Ni, Ru, Pd, and Ag) have been calculated using the full potential linearized augmented plane wave (LAPW) method based on GGA for exchange correlation potential [75]. The calculation shows Mn has the largest magnetic moment  $4.93\mu_B$ . A Bohr magneton is defined as  $\mu_B = (e\hbar)/2mc$  in cgs system and  $\mu_B = (e\hbar)/2m$  in the SI system. The  $3d$  TM-doped ZnOs show half-metallic behavior except for the Co-doped case, whereas the  $4d$ TM-doped ZnO showed normal metallic behavior with finite density of states (DOS) at the Fermi level for both the minority and majority spin states. Based on the first-principles spin-density functional calculations, Lee and Chang [76] also found that electron doping stabilizes the ferromagnetic ordering in Co-doped ZnO, but the ground state is spin glass without doping due to the short range interactions between the transition metal atoms. High electron concentrations and high Co concentrations are necessary to induce ferromagnetism in (Zn,Co)O.

Wang *et al.* [77, 78] used first principles calculations based on the density functional theory and GGA for exchange and correlation to calculate the total energies of a (Zn,Mn)O (10 $\bar{1}$ 0) thin film with Mn substituted at the Zn site. The thin film was modeled by a slab consisting of eight layers. Different configuration of Mn substitution of Zn sites were chosen so that the Mn-Mn separation as well as their nearest neighbor environment vary. In the dilute limit when Mn atoms are far apart, the system will display paramagnetic behavior. As the Mn concentration increases, Mn atoms tend to come close to each other and cluster around the O atom. This leads to exhibition of antiferromagnetic behavior. The ground state of Mn doped ZnO (10 $\bar{1}$ 0) thin film changes from



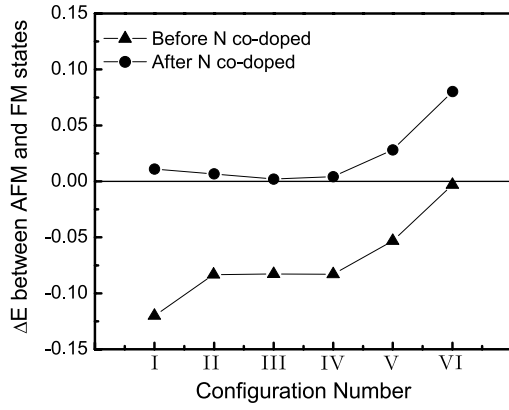


Figure 7 The energy difference  $\Delta E = E(\text{AFM}) - E(\text{FM})$  eV/Mn atom] between AFM and FM states for the six different configurations for Mn and N substitution. The solid triangle is for the  $\text{Zn}_{28}\text{Mn}_4\text{O}_{32}$  supercell, and the solid circle is for the  $\text{Zn}_{28}\text{Mn}_4\text{O}_{24}\text{N}_8$  supercell (after ref. 79. Courtesy of Q. Wang).

antiferromagnetic to ferromagnetic when codoped with N [79]. The calculation of the density of states (DOS) showed the distinct overlap between Mn 3d and N 2p states in the spin-up bands which leads to significant DOS at the Fermi energy and hence to the half-metallic character of N codoped (Zn,Mn)O system. Doping with N atoms introduces carriers, and Mn and N atoms prefer to exist as nearest neighbors in ZnO. The magnetic moment of Mn polarizes the spins at the neighboring N sites antiferromagnetically, which results in a ferromagnetic coupling between the Mn atoms. The spin alignments of the Mn atoms and the interlocking N atoms can be shown as  $\text{Mn}(\uparrow)\text{-N}(\downarrow)\text{-Mn}(\uparrow)$ , indicating that ferromagnetism is mediated through the  $p$ - $d$  exchange interaction between the carriers and Mn atoms. The energy difference between the antiferromagnetic state (AFM) and ferromagnetic (FM) state due to N doping is shown in Fig. 7. The maximum energy difference for 25% N doping is  $\sim 0.10$  eV/Mn atom. The high N concentration used in the model, i.e., from 6.25 to 25%, however, may be a challenge from a synthesis standpoint.

Feng [80] employed the Becke three parameter Lee-Yang-Parr (B3LYP) hybrid density functional method in the GGA approximation to study the electronic structure and possible ferromagnetic ordering in Co- and Mn-doped ZnO. The results indicate that in  $n$ -type ZnO electrons would occupy the empty Cu 3d states leading to  $\text{Cu}^{1+}$  states instead of  $\text{Cu}^{2+}$  ions because the unoccupied Cu 3d state is lower than the host conduction band states, which leads to a decrease in the number of  $n$ -type carriers. This means that the free electron concentration in the conduction band is reduced. If the sample is even marginally  $p$ -type then addition of Cu would tilt the balance in favor of  $p$ -doping. This may be the mechanism for increased holes in ZnO codoped with Cu and other TM elements [81, 82]. On the other hand, the unoccupied Mn 3d state is well above the lowest host conduction band states due to the large exchange splitting, so that no hole-providing mechanism is found in Mn-doped ZnO. Similarly, the calculation on the effect of Cu + Co codoping in ZnO also showed the  $p$ -type doping from Cu induce ferromagnetic inter-

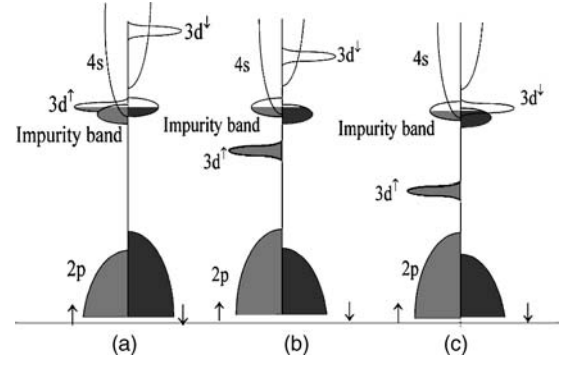


Figure 8 Schematic density of states for (a) TM = Ti, (b) TM = Mn, and (c) TM = Co. The Fermi level lies in a spin-split donor impurity band (after ref. 85).

actions between Co ions [83]. The experimental results will be discussed in detail in the next section.

Continuing on with co-doping, the electronic structures and magnetic properties of ZnO-based potentially diluted magnetic semiconductor co-doped with transition metals such as  $\text{Zn}_{1-2x}(\text{FeCo})_x\text{O}$  and  $\text{Zn}_{1-2x}(\text{FeCu})_x\text{O}$  were investigated by Park and Min [84]. Their results show that the double exchange mechanism is not effective in  $\text{Zn}_{1-2x}(\text{FeCo})_x\text{O}$ , but Fe and Cu ions in (Fe, Cu) doped ZnO have a tendency to form Fe-O-Cu clusters, and the much sought after double exchange-like interaction is expected to induce ferromagnetism in (Fe,Cu) doped ZnO.

Venkatesan *et al.* [85] used a spin-split donor impurity-band model to explain the observed systematic variation of magnetic moments across the TM-doped ZnO series, where V and Co showed much larger magnetic moment than other TM metals. For the light 3d elements, the  $3d\uparrow$  states lie high in the  $2p(\text{O})$  and  $4s(\text{Zn})$  gap, overlapping the donor impurity band which is spin split as shown in Fig. 8. In the middle of the series, there is no overlap with the 3d levels and exchange is weak, but towards the end of the series the  $3d\downarrow$  states overlap the impurity band, which then has the opposite spin splitting for the same occupancy. High Curie temperatures are found whenever unoccupied 3d states overlap the impurity band, but not otherwise. The likely origin of the donor impurity band in ZnO films is lattice defects, such as oxygen vacancies. Detailed studies are needed for the role of different defects. The authors found no relationship between conductivity and magnetic properties.

The first principles approach has also been used to elucidate magnetism in GaN-based DMS materials. As compared to the shallow acceptor Mn level in (Ga,Mn)As, the addition of Mn to GaN produces a deep impurity band within the GaN band gap. Litvinov and Dugaev [86] questioned the RKKY interaction employed in mean-field theory, and proposed that ferromagnetism in DMS systems is due to localized spins in the magnetic impurity acceptor level of the semiconductor crystal, and these localized spin excite band electrons due to  $p$ - $d$  exchange interaction. Their model provided a detailed and quantitative prediction of the dependence of the Curie temperature on the Mn concentration for various wurtzite III-N alloys.

Katayama-Yoshida *et al.* studied GaN with 5% of various transition metals [87] and  $\text{Ga}_{1-x}\text{Mn}_x\text{N}$  with  $x = 0.25$  [88]. For half-filled or less than half-filled  $d$  shell such as that in Mn, Cr, and V ferromagnetic state in GaN is stable. For a low concentration of Mn, ferromagnetism is favored whereas for the high concentration, the spin-glass phase is stable [71]. Based on local spin-density approximation functional calculations, Van Schilfgaarde and Myrasov [89] reported that for zinc blende GaN doped with 1 to 5% concentrations of Mn, Cr, and Fe, the exchange interactions are anomalous and behave quite differently from simple models such as RKKY [3, 90]. The strong attraction between the magnetic elements tends to group them together in small nanoclusters of a few atoms. The magnetic coupling between doped Mn atoms in clusters and crystals of GaN has been found to be ferromagnetic by Das *et al.* [91] using first principles calculations within GGA. Mn atoms tend to cluster and bind more strongly to N atoms than to Ga atoms, which suggest that the Mn concentration in GaN may be increased by using a porous substrate to offer substitutional surface sites. Their calculation also showed that the Fermi level passes right through the broadened impurity band (majority spin), thereby confirming that the impurity level acts as an effective mass acceptor. In a follow up investigation, Wang *et al.* [92] examined two different cases where Mn atoms are bonded in bulk GaN as well as (11 $\bar{2}$ 0) thin film forms by allowing full structural relaxation within GGA. The study shows that in the (Ga,Mn)N system, the Mn-Mn separation plays a critical role in their magnetic coupling. If the Mn atoms are incorporated into the GaN bulk, they couple ferromagnetically with or without structural relaxation. On the contrary, the coupling in unrelaxed thin film is ferromagnetic which then converts antiferromagnetic after relaxation. This may explain some controversial experimental observations for bulk and thin film (Ga,Mn)N.

Sato *et al.* [93] calculated the magnetic properties of (Ga,Mn)N from first-principles using the KKR-CPA method. It is found that the range of the exchange interaction in (Ga,Mn)N, being dominated by the double exchange mechanism, is very short ranged due to the exponential decay of the impurity wave function in the gap. (Ga,Mn)N shows no hightemperature ferromagnetism for low Mn concentrations, so that the experimentally observed very high  $T_C$  values in GaN should be attributed to small ferromagnetic MnN clusters and segregated MnN phases. The calculated  $T_C$  for (Ga,Mn)N is very low as compared with that obtained from mean-field theory which overestimates  $T_C$ .

Kronik *et al.* [94] reported the *ab initio* calculations for the electronic structure of (Ga,Mn)N with  $x = 0.063$ . The introduction of Mn results in the formation of a 100% spin polarized  $\sim 1.5$  eV wide impurity band, due to the hybridization of Mn 3d and N 2p orbitals (Fig. 9). This result is qualitatively different from the case of GaAs due to the different Mn level position: in GaAs the shallow acceptor, is  $\sim 0.1$  eV above the valence band maximum (VBM) in the isolated impurity limit; while in GaN deep acceptor level, is  $\sim 1.4$  eV above VBM. So in GaAs Mn hybridizes primarily with

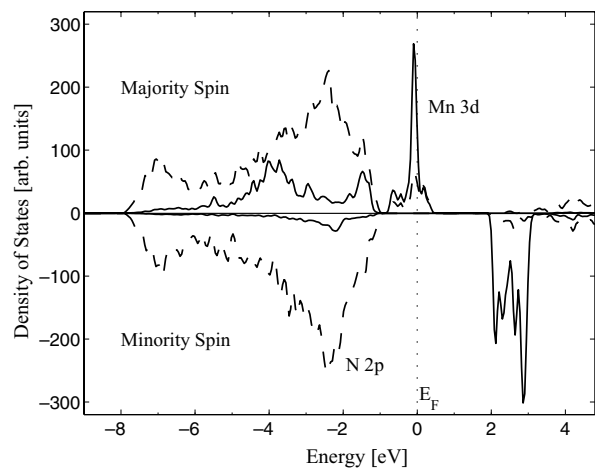


Figure 9 Partial density-of-states curves for wurtzite  $\text{Mn}_{0.063}\text{Ga}_{0.937}\text{N}$ . Solid lines: Mn 3d. Dashed lines: N 2p (after ref. 94. Courtesy of L. Kronik).

the valence band. However, in GaN its interaction with the valence band is therefore much smaller and the introduction of Mn barely polarizes the valence band. For a Mn composition of 6.3%, the impurity band does not hybridize to an extent sufficient for merging with the valence band. The impurity band renders the material half metallic and supports the effective-mass transport within it, which implies that (Ga,Mn)N is a highly suitable material for spin injectors.

Kulatov *et al.* [95] studied the electronic structure and the properties of zinc blende (Ga,Mn)N with Mn concentration ranging from 1.56 to 12.5%. The calculations showed that the ferromagnetic state is lower in energy than those for the paramagnetic and antiferromagnetic states. The magnetic interaction of Mn atoms is short ranged. Their results also showed the important difference between GaAs and GaN in the energy position and localization of the Mn spin-majority states, as in Ref. 94. Codoping of O for N and Zn for Ga in (Ga,Mn)N shows that the atoms of O and Zn change the occupation of Mn bands and strongly affects both the magnetic moments and conductivity. In addition, O codoping drastically enhances the ferromagnetic state, and also causes a significant increase in the Curie temperature of (Ga,Mn)N. Further, Zn codoping causes strong hybridization of the  $e_g$  states of Mn with VB and decrease the FM.

Sanyal *et al.* [96] investigated the effect of varying Mn concentration on the electronic and magnetic properties in wurtzite (Ga,Mn)N by using a first-principles planewave method. They showed that the  $d$  states of Mn form an impurity band completely separated from the valence band states of the host GaN for dilute Mn concentration. Up to  $x = 0.25$ , the Fermi level lies only in the spin-up density of states, as there is no state at the Fermi level for the spin-down channel, so that the system is half-metallic with a high magnetic moment. For  $x = 0.5$ , the system behaves like a ferromagnetic metal with a reduced magnetic moment due to the partially filled spin-down channel. The authors also showed that the DOS for a zinc blende structure is similar to that of a wurtzite structure.

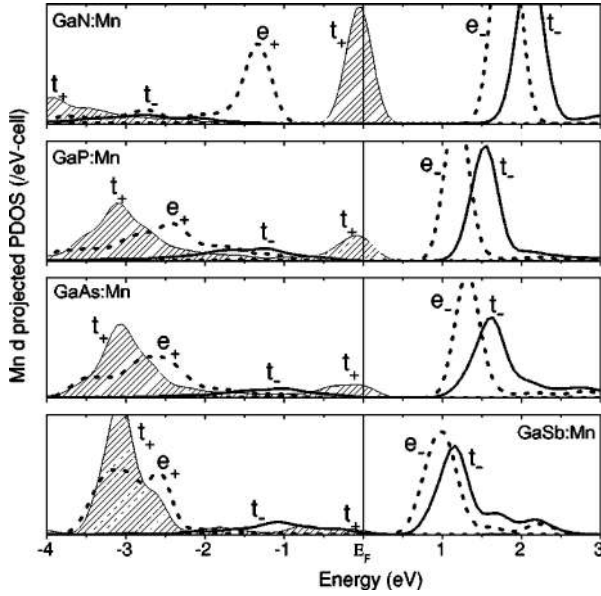


Figure 10 Mn  $d$  projected partial density of states for a single Mn in GaN, GaP, GaAs, and GaSb, where the symmetry ( $t_2$  and  $e$ ) as well as the spin (+ and -) have been indicated. The shaded region represents the  $t_2^+$  states (after ref. 97).

Mahadevan and Zunger [97] used first-principles total-energy calculations to study the trends of Mn in GaN, GaP, GaAs, and GaSb. Fig. 10 shows the calculated Mn  $d$  projected local density of states for neutral substitutional Mn ( $\text{Mn}^{3+}$ ) in four GaX compounds. As can be seen, the antibonding  $t_2$  level, which in the neutral state of the impurity is occupied with two electrons (and therefore one hole) and strongly Mn-localized. Moreover, the degree of Mn-localization of the hole level decreases along the series GaN  $\rightarrow$  GaP  $\rightarrow$  GaAs  $\rightarrow$  GaSb. The acceptor level of  $\text{Mn}^{2+}$  is shown to be very deep in the (Ga,Mn)N,  $\sim 1.4$  eV, and it becomes progressively shallower as the anion X becomes heavier. They predicted a strong ferromagnetic stabilization in (Ga,Mn)N due to the  $p$ - $d$  interaction which couples the  $t_+$  level of Mn ions to the  $p$ -like dangling bond states of the Ga vacancy, despite the fact that the hole orbital is a highly localized deep acceptor. This is in contrast to the model provided by Dietl [65] which assumes a host-like delocalized hole for all materials. In another study, Mahadevan and Zunger [98] explained the electronic structures of Cr and Mn in GaN as follows: introduction of a transition-metal impurity in III-V semiconductor introduces a pair of levels with  $t_2$  symmetry—one localized primarily on the transition-metal atom, referred to as crystal-field resonance (CFR), and the other localized primarily on the host anion atoms next to the impurity, referred to as the dangling bond hybrid (DBH). In addition, a set of nonbonding states with  $e$  symmetry, localized on the transition-metal atom, are also introduced. Each of the levels is also spin split. Considering Mn in GaN shown in Fig. 11, the  $3d$  levels are well above the host cation dangling bonds. The dangling bond states are shown on the right hand side, and the crystal field and exchange split Mn  $d$  levels are shown on the left hand side. The  $t_2(p)$  levels of the anion dangling bond hybridize with the  $t_2(d)$  levels of the transition metal.

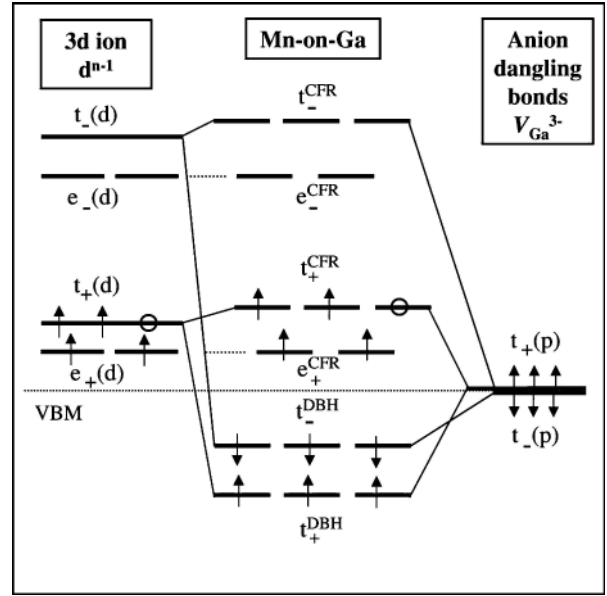


Figure 11 The schematic energy level diagram for the levels (central panel) generated from the interaction between the crystal-field and exchange-split levels of the  $3d$  transition metal ion (left panel) with the anion dangling bond levels (right panel), when the TM  $d$  levels are energetically shallower than the dangling bond levels (after ref. 98).

The levels generated after hybridization are shown in the central panel. The hybridization in the  $t_2$ -channel creates bonding, transition-metal localized CFRs:  $t_{+}^{CFR}$ , and  $t_{-}^{CFR}$ , as well as the host-anion localized antibonding DBHs  $t_{+}^{DBH}$  and  $t_{-}^{DBH}$ , whereas the  $e$  channel creates the nonbonding  $e_{+}^{CFR}$  and  $e_{-}^{CFR}$  states. The hole resides in the  $t_{+}^{CFR}$  level deep in the band gap. The symmetry ( $e$  vs.  $t_2$ ) and the character (DBH vs CFR), as well as the occupancy of the gap level, determine the magnetic ground state favored by the transition-metal impurity.

Recent *ab initio* band structure and total energy calculations [94–97] seem to agree that Mn  $3d$  levels are located in the gap, and that the interaction between substitutional Mn ions is ferromagnetic, at least in the not so high Mn concentration range. Based on these understandings and by using a band structure approach and level repulsion model, Dalpian *et al.* [99, 100] proposed a unified picture to explain the magnetic ordering in Mn doping III-V and II-VI semiconductors. The schematic model of the host  $p$  states (VBM) and Mn  $d$  levels and level repulsion caused by  $p$ - $d$  exchange coupling and  $d$ - $d$  coupling between them in ferromagnetic and antiferromagnetic configuration is shown in Fig. 12. In (Ga,Mn)N the Mn  $d$  levels are above the VBM. In the ferromagnetic (FM) configuration, the majority spin state of neighboring Mn atoms couple to each other: the spin-up channel of one Mn atom couples to the spin-up channel of neighboring Mn atom. In the spin-up channel, step (a) to (b) and step (a') to (b') describe the  $p$ - $d$  exchange coupling, which results in pushing the  $t_{2d}$  state upward by  $2\Delta_{pd}^1$  and pushing down the  $t_{2d}$  state by the same amount. Steps (b) or (b') to (c) describes the  $d$ - $d$  coupling between the two  $t_{2d}$  states of neighboring Mn atoms. As a result, the holes are placed at a high energy level and electrons are at an energy level lowered by  $2\Delta_{dd}^1$ . The net energy gain in the spin-up channel is derived to be  $-2n_h\Delta_{pd}^1 - n_h\Delta_{dd}^1$ , where  $n_h$  is the

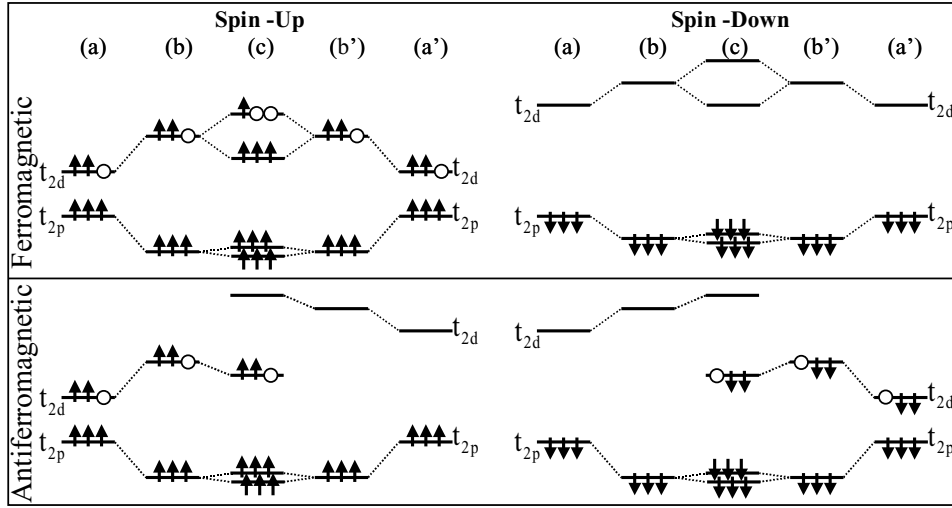


Figure 12 Schematic model showing the position of the  $p$  and  $d$  levels and level repulsion between them in FM and AFM configurations. In this case, the Mn  $d$  levels are above the VBM. Note that in (b), (b'), and (c), the states have mixed  $pd$  characters (after ref. 99. Courtesy of G. M. Dalpian).

number of holes in the VBM. In the spin-down channel, the  $p$ - $d$  coupling lowers the energy of occupied  $t_{2p}$  spin-down state by  $2\Delta_{pd}^2$ . The net energy gain in the spin-down channel is  $-12\Delta_{pd}^2$  for the six electrons in the  $t_{2p}$  state. The total net energy gain in the FM configuration is  $-2n_h\Delta_{pd}^1 - n_h\Delta_{dd}^1 - 12\Delta_{pd}^2$ . In the antiferromagnetic (AFM) configuration, the majority spin state of one Mn atom couples only to the minority spin states of the other Mn atom with opposite moment. The situation can be analyzed similarly as in the FM configuration. The total net energy gain in the AFM configuration is  $-(6 - n_h)\Delta_{dd}^{1,2} - 2n_h\Delta_{pd}^1 - 12\Delta_{pd}^2$ , where  $\Delta_{dd}^{1,2}$  is the level repulsion caused by the coupling between the majority spin  $d$  state and the minority spin  $d$  state. The energy difference between the FM and AFM state is  $(6 - n_h)\Delta_{dd}^{1,2} - n_h\Delta_{dd}^1$ . This indicates that when the system has holes at the  $t_{2d}$  level instead of VBM, the stabilization of the FM or AFM state is not directly related to the  $p$ - $d$  exchange splitting, but to the  $d$ - $d$  coupling term  $\Delta_{dd}^1$  (double exchange) and  $\Delta_{dd}^{1,2}$ . In the case of (Zn,Mn)O, there is no hole, so AFM state is more stable. The detailed *ab initio* band structure and total energy analysis revealed that the FM is stable for (Ga,Mn)N for moderate Mn concentration (for example, 6.25% Mn), but it is transferred to AFM state when Mn concentration increases due to the increase of the AFM stabilization energy  $\Delta_{dd}^{1,2}$  caused by a stronger  $p$ - $d$  repulsion [100]. The magnetic order can also be altered by applying pressure or with charge compensation.

In addition to Mn-doped GaN, theoretical work has also been reported for other transition metals such as Cr [5, 88, 101], Co [102], and Vanadium (V) [23, 88] in GaN. Das *et al.* [5] studied the electronic structure, energy bands, and magnetic properties of Cr-doped GaN from first principles with GGA. The coupling between Cr atoms was found to be ferromagnetic in both crystal and small clusters. Kim *et al.* [101] reported the electronic structure of Cr-doped GaN observed by hard X-ray photoemission spectroscopy and first-principle calculations. They proposed that the ferromagnetic interaction between distinct Cr atoms may be mediated by the Cr  $3d$ -N  $2p$ -Ga  $4s$  hybridization, but this sugges-

tion needs to be confirmed by more data from magnetic and optical characterization. 6.25% Co-doped GaN was calculated for its magnetic properties by Hong and Wu [102] using the full potential linearized augmented plane wave (LAPW) method. Co atoms were found to prefer to remain close to each other in GaN and form ferromagnetic ordering. In a similar fashion, Vanadium (V) was predicted [88] to be ferromagnetic when doped in GaN, based on *ab initio* calculations within the local spin density approximation, which gives the electronic structure of the  $3d$ -metal doped GaN by the KKR-CPA method. However, at least in one experiment, V-implanted GaN showed paramagnetic behavior up to 320 K [23].

Dalpian and Wei [103] studied the magnetic properties of cubic  $\text{Ga}_{1-x}\text{Gd}_x\text{N}$  by using *ab initio* band structure calculations and symmetry arguments. The  $4f$  orbitals in the rare earth elements are more localized, thus the direct coupling between the  $4f$  ions is expected to be weak. As compared to the  $3d$  transition metal elements, the  $4f$  rare earth elements can have larger magnetic moments and can couple strongly with the host  $s$  electrons. It is found that (Ga,Gd) in the zinc-blende phase is more stable in antiferromagnetic state. Introducing electrons in (Ga,Gd)N can stabilize the ferromagnetic state, so that electron-mediated ferromagnetism is induced. Based on the polarization of donor electrons in the very diluted limit, the authors also explained the colossal magnetic moment observed in (Ga,Gd)N by Dhar *et al.* [25].

Experimental observations of ferromagnetism in both  $p$ -type and  $n$ -type GaN DMS materials have been reported in spite of the bulk of the theoretical discussions, centered around non *ab initio* calculations, which require  $p$ -type GaN as a result of stronger  $p$ - $d$  interaction in heavily as compared to  $s$ - $d$  interaction. The discrepancy between these theories and experiments could perhaps be better understood by invoking the possibility that perhaps some observations might be clouded by magnetic contamination, imperfections of material quality specific to growth techniques, such as dislocations and deep-level defects of host materials [104], clusters [105, 106], precipitates [107, 108],

anti-site defects [109], and nonsubstitutional impurity sites [110]. On the theory side, it may be that *ab initio* calculations, which are comprehensive by nature in terms of being inclusive of all the mechanisms that may take place, are needed for an accurate determination of whether the material is FM and if so what the Curie temperature is. Already, mean-field theory appears to overestimate the Curie temperature substantially for lower magnetic ion densities.

We must not lose sight of the fact that the results from different theoretical approaches do not agree well to say the least. Presumably, no single model is capable of explaining the properties of a wide class of dilute magnetic semiconductors including ZnO and GaN with their many variants. This being the case, multi-sourced possible explanations may have to be taken into consideration at this stage [111]. In particular, if the solubility limit of the magnetic dopant is exceeded, uniform ferromagnetic behavior or precipitates exhibiting ferromagnetism may form. Naturally, the magnetic properties of any such precipitates will depend on the growth conditions. In general, the contribution by precipitates to the overall magnetic properties of the bulk DMS cannot be excluded. There is a clear need for further research in this field if clarity is to be obtained. In this vein, extended X-ray absorption fine structure (EXAFS) studies of DMS can shed light on the detailed microscopic structure of the lattice which is more complicated than assumed in at least some of the theoretical approaches discussed here. Such careful structural investigations have been undertaken in several II–VI compounds [112]. It is believed that with more progress in the synthesis and characterization techniques for DMS materials, improvements in various theories to understand the underlying mechanism will follow. What is certain is that in due time, science will correct its course.

#### 4. Experimental results of TM-doped ZnO

Experimental research on TM-doped ZnO attracted much interest after the prediction that ZnO is a promising candidate for realizing high Curie temperature ferromagnetic DMS [3, 49, 67]. ZnO is a direct band gap semiconductor with  $E_g \sim 3.3$  eV at 300 K. ZnO normally has a hexagonal (wurtzite) crystal structure with  $a = 3.25$  Å and  $c = 5.12$  Å. ZnO thin film is usually *n*-type due to electron doping via defects originating from Zn interstitials, O vacancies in the ZnO lattice, or impurities including hydrogen. High electron carrier density can also be realized via group III substitutional doping. On the other hand, *p*-type doping remains a challenge. Recently, Tsukazaki *et al.* [113] reported *p*-type doping by N in ZnO layers grown on high quality ZnO. If indeed, these results could be confirmed and if the hole mediated ferromagnetism is the dominant mechanism, attainment of *p*-type ZnO could pave the way for a promising potential of TM-doped ZnO and devices. For more detailed information of ZnO properties, the reader is referred to a comprehensive review of ZnO [114].

Continuing with experimental investigations, Fukumura *et al.* [115] reported (Zn,Mn)O by pulsed laser deposition (PLD). In this particular work up to 35% Mn was incorporated into ZnO without affecting much the crystallographic quality of the DMS, whereas about 5% is tolerable for III–V-based hosts. A relatively higher solubility might be expected in II–VI hosts owing to  $Mn^{2+}$  nature, which can be achieved easily by having the  $4s^2$  electrons participate in the bonding process. The  $4s$  electrons are much closer to the O atom which lacks 2 electrons in its  $2p$  shell and Mn has exactly half filled  $3d$  shell depicted by  $Mn^{2+}d^5$  [1]. It will cost a considerable amount of energy to add an electron with the opposite spin to the  $3d^5$  orbit. The gist of this discussion is that the Mn behaves in much the same way as Zn and thus high solubility should be expected, although the fact that Zn being a relatively larger atom must not be ignored. The report of high solubility of Mn in ZnO [115] triggered intensive research in TM-doped ZnO by many other groups employing various thin film growth techniques. Growth of these ferromagnetic materials by thin film techniques, such as MBE [116], metalorganic chemical vapor deposition (MOCVD) [117], and pulsed laser deposition (PLD) [118], provides excellent control of the dopant concentration and the ability to grow single-phase layers. However, the results concerning the existence of ferromagnetism have been rather controversial. While some groups have reported ferromagnetism in (Zn,TM)O systems with  $T_C$  ranging from 30 to 550 K [26, 28, 29, 33, 72, 81, 119–121], others reported observations of antiferromagnetic and spin-glass behavior [35, 122–126]. The distribution of TM elements in the host ZnO is also an important issue to be addressed. The term DMS refers to the fact that some fraction of the atoms in an otherwise non-magnetic semiconductor host like ZnO are replaced by magnetic ions. A key unanswered question is whether the resulting material indeed contains uniformly distributed transition-metal elements or contains clusters, precipitates or second phases that are responsible for the observed magnetic properties. Table IV summarizes recent reports of magnetic properties of transition-metal-doped ZnO.

Most probable reason of the controversy in the magnetic properties of ZnO-based DMS as stated above might in part have its roots in the insufficient characterization of the samples [137]. As discussed in the theory tutorial section, the mechanism for the observed magnetic behavior is complex and appears to depend on a number of factors, including Mn-Mn spacing, and the carrier density and type. These parameters will affect the band and electronic structure of the material, which strongly affect its magnetic properties. Depending on the growth conditions employed for growing the DMS material, the properties of DMSs can be very different. Therefore, it might be necessary to decide on a case-by-case basis which mechanism is dominant. This can only be achieved by a careful correlation of the measured magnetic properties with materials analysis methods that are capable of detecting other phases and precipitates.

TABLE IV List of recently reported magnetic properties of ZnO-based DMS. The TM content listed corresponds to the magnetic property and Tc in the "Note" and " $T_C$ " columns. Magnetic moment per TM atom is listed when it is available. *c*-sapphire, *a*-sapphire, and *r*-sapphire means the substrate surface is perpendicular to [0001], [11 $\bar{2}$ 0], and [1 $\bar{1}$ 02] direction, respectively

Compound	TM content	Substrate (for thin film) or bulk	Fabrication method	Growth temperature (°C)	Oxygen pressure (Torr)	Post-annealing	$T_C$ (K)	Notes	Reference
(Zn,Mn)O	<0.35	<i>c</i> -sapphire	PLD	600	$5 \times 10^{-5}$			Spin glass	115
(Zn,Mn)O	0.36	<i>c</i> -sapphire	PLD	600	$5 \times 10^{-5}$				122
(Zn,TM)O		<i>c</i> -sapphire	PLD	500–600	$1 \times 10^{-9}$ to $10^{-6}$				123
(Zn,Mn)O	0.01 ~ 0.36	<i>c</i> -sapphire	PLD	610	$5 \times 10^{-5}$			Paramagnetic	124
(Zn,Mn)O	0–0.3	<i>c</i> -sapphire	PLD				> 30–45	0.15–0.17 $\mu_B$ /Mn	26
(Zn,Mn)O	<0.04		Sintered pellets	500–700	Air, 1 atm		> 425	0.16 $\mu_B$ /Mn	72
(Zn,Mn)O	0.0221	Fused quartz	PLD	400	0.2		> 425	0.05 emu/g single phase	72
(Zn,Mn)O	0.04–0.09	<i>c</i> -sapphire	Reactive sputtering	200–380			> 400	3 $\mu_B$ /Co	127
(Zn,Mn)O	0.07	<i>a</i> -sapphire	Sputtering	400	0.06			Paramagnetic	128
(Zn,Mn)O	0.03 & 0.2	GaAs (001)	Sputtering	500–600	$8 \times 10^{-4}$ in Ar				129
(ZnO@Mn,Mn,Sn)	0–0.3	Bulk ZnO	Implantation			700 °C, 5 min RTA in N <sub>2</sub>	250	Ferromagnetic	28
(ZnO@Mn,Sn)	Mn 0.03 Sn <0.1	<i>c</i> -sapphire	PLD	400–600	0.02		> 300	Ferromagnetic	130
ZnO@Co, (Mn, Cr, or Ni)	0.05 ~ 0.25	<i>c</i> -sapphire	PLD	350–600	$2-4 \times 10^{-5}$		280–300	2 $\mu_B$ /Co	119
(ZnO@Mn,Co)	0.02–0.15		Crystalline precursor					Antiferromagnetic	125
(ZnO@Mn,Co)	<0.05		Melt-growth					Paramagnetic	126
(Zn,Co)O	0.03–0.05	Bulk ZnO	Ion implantation			700 °C, 5 min, in O <sub>2</sub>	> 300	Co nanocrystals	131
(Zn,Co)O	0–0.25	<i>c</i> -sapphire	Sol-gel	<350		RTA 700 °C, 1 min in O <sub>2</sub>	> 350	0.56 $\mu_B$ /Co	29
(Zn,Co)O	0.015		PLD	650	$5 \times 10^{-5}$		> 300	Ferromagnetic	132
ZnO@Co,Al)	0.04–0.12	Glass	rf sputtering	300–700	$1 \times 10^{-2}$ in Ar		> 350	0.21 $\mu_B$ /Co	133
(Zn,Co)O	0.02–0.5	<i>c</i> -sapphire	PLD		$1 \times 10^{-6}$ to $10^{-1}$			Spin glass	35
ZnO:Co	0.1	face ZnO	PLD	300–650				Antiferromagnetic	134
ZnO:Co	<0.35	<i>r</i> -sapphire	MOCVD	600	40	500 °C, 20 min in vacuum	> 350	Ferromagnetic	135
(ZnO@Co, Fe)	<0.15	SiO <sub>2</sub> /Si	Magnetron sputtering	897	$2 \times 10^{-3}$	600 °C, 10 min, $1 \times 10^{-5}$ Torr	> 300	12–15 emu/cm <sup>3</sup>	33
(ZnO@Cu,Fe)	Fe < 0.07 Cu < 0.01	Bulk	Solid-state reaction				550	0.75 $\mu_B$ /Fe	81
(Zn,Ni)O	0.01–0.25	<i>c</i> -sapphire	PLD	300–700	$1 \times 10^{-5}$			Super para- or ferromagnetic	120
(Zn,V)O	0.05–0.15	<i>r</i> -sapphire	PLD	300	$10^{-5}$ to $10^{-3}$		> 350	0.5 $\mu_B$ /Co	121
ZnO:Mn	0.1	<i>r</i> -sapphire	PLD	650	0.1			0.075 $\mu_B$ /Mn	136
(ZnO@Mn,Cu)	Mn 0.1, Cu 0.05	<i>r</i> -sapphire	PLD	650	0.1		400	0.1 $\mu_B$ /Mn	136
ZnO@Sc,Ti, (V, Fe, Co, Ni)	0.05	<i>r</i> -sapphire	PLD	600	0.1 to 750		> 300	2.6 $\mu_B$ /Co 0.5 $\mu_B$ /Ti 0.3 $\mu_B$ /Sc	85

TABLE V Second phases observed in TM-doped ZnO and their magnetic properties. Curie temperature (for ferro- or ferromagnetic material) or Neel temperature (for antiferromagnetic material) of each possible TM-related phase is given

Phase	Nature of magnetism	Curie temperature or Neel temperature (K)	Reference
MnO	Antiferromagnetic	116	26
MnO <sub>2</sub>	Antiferromagnetic	92	138
Mn <sub>2</sub> O <sub>3</sub>	Antiferromagnetic	76	138
Mn <sub>3</sub> O <sub>4</sub>	Ferromagnetic	43	138
Mn <sub>3</sub> O <sub>4</sub> (distorted spinel)	Ferrimagnetic	46	139
Mn <sub>3</sub> O <sub>4</sub> (Hausmannite)	Ferrimagnetic	40	140
(Zn,Mn)Mn <sub>2</sub> O <sub>4</sub>	Ferrimagnetic	40	141
ZnMnO <sub>3</sub> (cubic)	Spin-glass		142
Zn <sub>3</sub> MnO <sub>6</sub> (hexagonal)			142
Co	Ferromagnetic	1373	131
CoO	Antiferromagnetic	291	119, 143
CuO	Antiferromagnetic (monoclinic)	230	144
Cu cluster	Antiferromagnetic	154	144
FeO (cubic)			81
(Zn, Fe) <sub>3</sub> O <sub>4</sub>	Ferromagnetic	440	143
ZnFe <sub>2</sub> O <sub>4</sub> (bulk)	Nonferromagnetic		145
ZnFe <sub>2</sub> O <sub>4</sub> (invert spinel)	Ferromagnetic		145

Table V lists some second phase precipitates reported in TM-doped ZnO. Although X-ray diffraction (XRD) measurements play an important role in attempts to detect any impurity phases present, the sensitivity may not be good enough to identify minute amounts of precipitates in the samples. Other characterization techniques [146], some more sophisticated, such as scanning electron microscope (SEM), reflection high energy electron diffraction (RHEED), transmission electron microscope (TEM), electron probe microanalysis (EPMA), and secondary ion mass spectrometry (SIMS), possibly more than applied to a given sample, might have to be employed to identify the precipitates down to nanoscale and investigate the uniformity of dopant distribution in the host material. Fukumura *et al.* [137] gave a detailed review of the characterization techniques for oxide-based DMS. It was also pointed out that in the case of magnetic measurement of a thin film on a substrate, the measured signal, which is in proportion to the sample volume, includes the magnetic moment not only from the film but also from the substrate (which is in general diamagnetic) owing to the much larger volume of substrate than that of film. Therefore, a careful analysis of magnetization measurements must be carried out in conjunction with reports of ferromagnetism based simply on magnetic hysteresis. The magnetism measurements would be much more useful if the magnetic moment per magnetic ion in the sample is also determined. Despite the considerable controversy regarding the origin of ferromagnetism in ZnO-based DMSs reported in the literature, in the following section we discuss what has been reported on the experimental side.

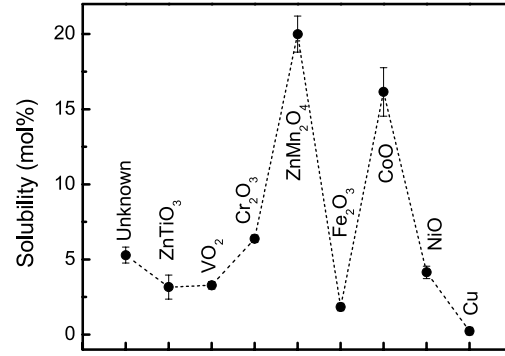


Figure 13 Solubility limit of TM ions in ZnO. The upper and lower limit of the error bars corresponding, respectively, to the lowest  $x$  of the compounds precipitated and the highest  $x$  of the compounds without precipitation. The precipitated phases are also shown (after ref. 123).

#### 4.1. Properties of Mn-doped ZnO

Jin *et al.* [123] determined the solubility limits of transition metal dopants in ZnO thin films grown by laser MBE. Fig. 13 shows these limits determined by the presence of impurity peaks in the X-Ray diffraction patterns. The transition metal compositions were measured by EPMA as well.

The solubility of Mn into ZnO can exceed the equilibrium limit ( $\sim 13\%$ ) and reaches up to 35% [115] as a result of the nonequilibrium PLD film growth process. With increasing Mn content the lattice constants  $a$  and  $c$  of wurtzite  $\text{Zn}_{1-x}\text{Mn}_x\text{O}$  increases due to the fact that the ionic radius of  $\text{Mn}^{2+}$  ( $0.66 \text{ \AA}$ ) is larger than that of  $\text{Zn}^{2+}$  ( $0.60 \text{ \AA}$ ) [119, 124, 125, 138, 141], and the bandgap expands with considerable mid-gap absorption. This mid-gap absorption peak centered around 3 eV in Mn-doped ZnO is usually broad and structureless at room temperature, owing to the overlap of the intra- $d$  shell transitions of  $\text{Mn}^{2+}$  from its ground state  $^6A_1(S)$  to  $^4T_1(G)$ ,  $^4T_2(G)$ ,  $^4A_1(G)$ , and  $^4E(G)$  [147]. Fig. 14(a) shows the optical transmittance at room temperature for  $\text{Zn}_{1-x}\text{Mn}_x\text{O}$  films with different Mn contents. As the Mn content is increased, the gap absorption around 3 eV develops and the absorption edge blueshifts. It should be mentioned any change in the bandgap of Mn doped ZnO depends on whether the Mn atom orbitals hybridize in such a way as to lead to bonding state.

These ZnO thin films with high Mn concentration, however, did not show ferromagnetic behavior. Field-cooled (FC) and zero-field-cooled (ZFC) temperature dependence of the magnetization ( $M$  vs.  $T$ ) for a  $\text{Zn}_{0.64}\text{Mn}_{0.36}\text{O}$  thin film grown by pulsed laser deposition [122] is shown in Fig. 14(b). The nomenclature FC denotes the procedure of cooling the sample in a field,  $H$ , and measuring the magnetization,  $M$ , with the field on. The nomenclature ZFC denotes the procedure of cooling the sample in zero field and measuring the magnetization,  $M$ , upon warming with the field  $H$  on. The magnetization for the ZFC run deviates from that in the FC run at around  $\sim 10 \text{ K}$ . The cusps in the ZFC and FC magnetization are typically interpreted as an indication of spin-glass behavior [1]. The effective Mn content that is linked to the net magnetization compared to the fully saturated magnetization of the  $\text{Mn}^{2+}$  spin is very small ( $0.021 \mu_B$ ), also implying a strong antiferromagnetic exchange coupling. This result is consistent



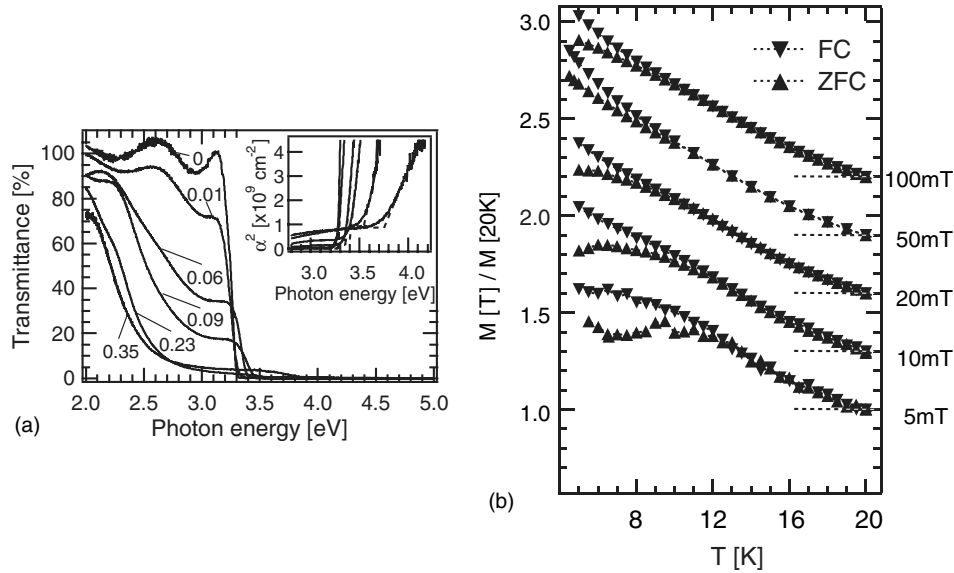


**Figure 14** (a) Transmission spectra of  $\text{Zn}_{1-x}\text{Mn}_x\text{O}$  films measured at room temperature for various  $x$  values. Numbers in the figures denote  $x$ . Inset shows the photon energy dependence of squared absorption constant ( $\alpha^2$ ) around the bandgap ( $E_g$ ). (b) Magnetization normalized at 20 K for a  $\text{Zn}_{0.64}\text{Mn}_{0.36}\text{O}$  film measured during ZFC and FC runs in various magnetic fields. The curves are vertically shifted as represented by the dotted lines (after ref. 122. Courtesy of T. Fukumura).

with the *ab-initio* calculations by Sato and Katayama-Yoshida [4] who predicted a transition from the antiferromagnetic state to the ferromagnetic state only with the introduction of holes.

The blueshift of bandgap energy and the increase of midband absorption have also been observed from  $\text{Zn}_{0.93}\text{Mn}_{0.07}\text{O}$  deposition by RF magnetron sputtering [128]. The Auger electron spectroscopy showed that Mn is uniformly distributed throughout the film. The magnetic property has been concluded as paramagnetic because the field dependent magnetization of (Zn,Mn)O can be described well with Curie-Weiss law. Liu *et al.* [142] studied the structure of Mn-ZnO deposited by RF magnetron sputtering on sapphire substrates. The Mn-doped ZnO showed magnetic hysteresis at 5 K while the magnetization at 300 K is much

weaker. Although the wurtzite crystal structure was maintained, the incorporation of Mn led to a large amount of structural disorder in the crystalline columnar ZnO lattice. The substitutional fraction of Mn was about 25% in the Mn-doped ZnO film as derived from Rutherford backscattering (RBS) measurement, indicating that most of the Mn incorporated in the film was present in other forms. The TEM structure analysis revealed that the Mn-doped ZnO layer included a high density of round-shaped cubic and elongated hexagonal MnZn oxide precipitates. Detailed analyses of the precipitates by energy dispersive spectroscopy (EDS) and lattice spacing measurement identified the round shaped precipitates to be the perovskite phase of  $\text{ZnMnO}_3$  and the elongated hexagonal precipitates to be  $\text{Zn}_3\text{MnO}_6$ . Fig. 15(a) shows the columnar growth mode

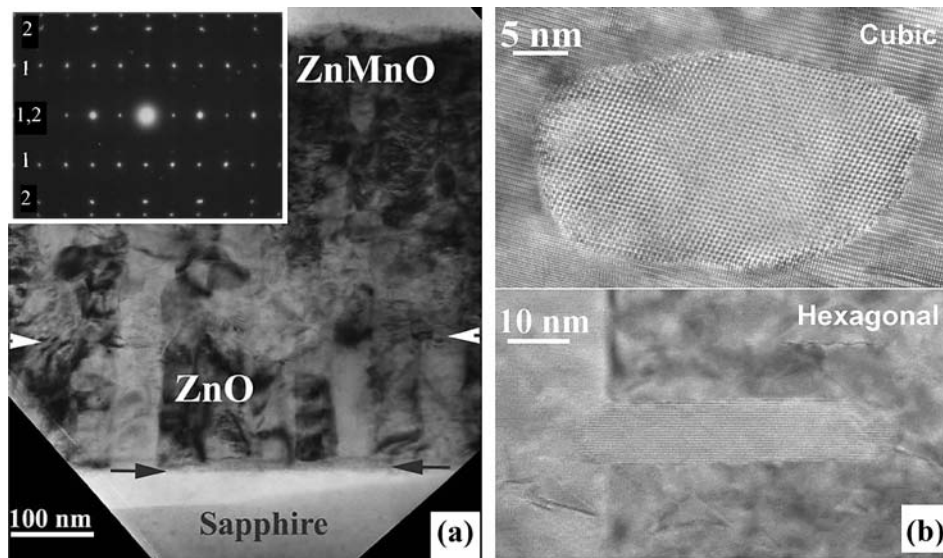


**Figure 15** (a) Bright-field cross-sectional TEM image of the Mn-doped ZnO thin film. The interfaces of undoped ZnO buffer/sapphire and Mn-doped ZnO/undoped ZnO buffer are indicated by arrows. A trimetallic (AlMn) $\text{ZnO}_3$  phase was found in the ZnO/sapphire interface region. The inset is the selective-area electron diffraction pattern from the undoped ZnO buffer layer. (b) Magnified cross-sectional TEM images of the cubic and hexagonal precipitates in the Mn-doped ZnO layer (after ref. 142).

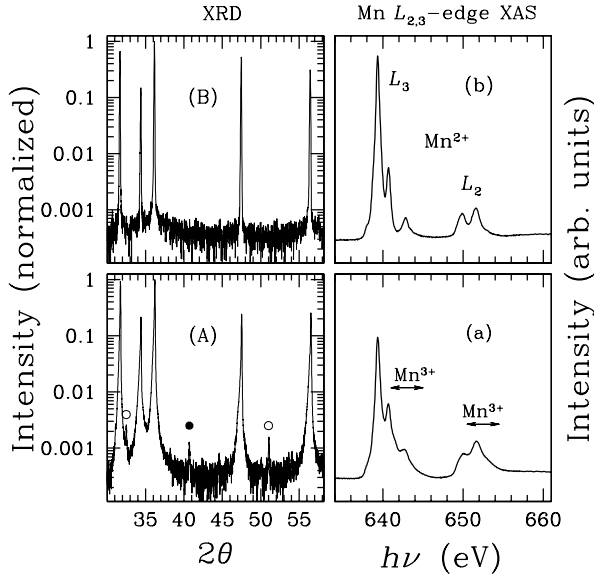


Figure 16 X-ray diffraction pattern is displayed as the left panels (A) and (B) for samples A and B, respectively. The large peaks in (A) and (B) belong to the ZnO structure, while the small peaks in (A) are from secondary phases, MnO (●) and (Mn,Zn)Mn<sub>2</sub>O<sub>4</sub> (○). The right panels (a) and (b) show Mn 2*p*-3*d* X-ray absorption spectrum for samples A and B, respectively. Note that the *L*<sub>2,3</sub>-edge shape of sample A deviates from the Mn<sup>2+</sup> character of sample B at the high energy side as indicated by arrows. This deviation is caused by Mn<sup>3+</sup> (after ref. 141. Courtesy of Y.-H. Jeong).

of the undoped ZnO buffer layer. When the Mn doping is initiated, the crystalline columns are disrupted and the Mn-doped ZnO layer contains a high density of precipitates, some of which appear as dark areas in Fig. 15(a). Fig. 15(b) shows magnified cross-sectional TEM images of one of the round-shaped cubic and elongated hexagonal precipitates.

Han *et al.* [141] demonstrated that in polycrystalline (Zn,Mn)O synthesized by solid state reaction the precipitate (Zn,Mn)Mn<sub>2</sub>O<sub>4</sub> is responsible for the observed ferromagnetic transition. In Fig. 16 the X-ray absorption spectroscopy at Mn *L*<sub>2,3</sub> edges indicates the existence of Mn<sup>3+</sup> charge states in the sample that has (Mn,Zn)Mn<sub>2</sub>O precipitate. The bulk (Zn,Mn)O without second phase precipitate showed paramagnetic behavior.

Lawes *et al.* [125] conducted a study on bulk Zn<sub>1-x</sub>Mn<sub>x</sub>O and Zn<sub>1-x</sub>Co<sub>x</sub>O with  $x = 0.01$  and  $0.15$ . No evidence for a ferromagnetic transition in these systems was observed above 2 K. The authors proposed a model which considers two subsets of spins to explain the observed magnetic properties. One subset of spins, which belongs to the TM ions with no TM nearest neighbors, is completely free (isolated spins). The second subset of spins, which belongs to those TM ions with at least one TM nearest neighbor, is affected by mean field interactions (clustered spins). With increase of Mn concentration, the fraction of Mn ions belonging to the second subset increases, so that the antiferromagnetic interaction reduces the net magnetization. Separating the TM ions into two noninteracting subsets of spins also gives an excellent description of the susceptibility over the temperature range that has been measured, as seen in Fig. 17. The feature of the susceptibility, namely a high

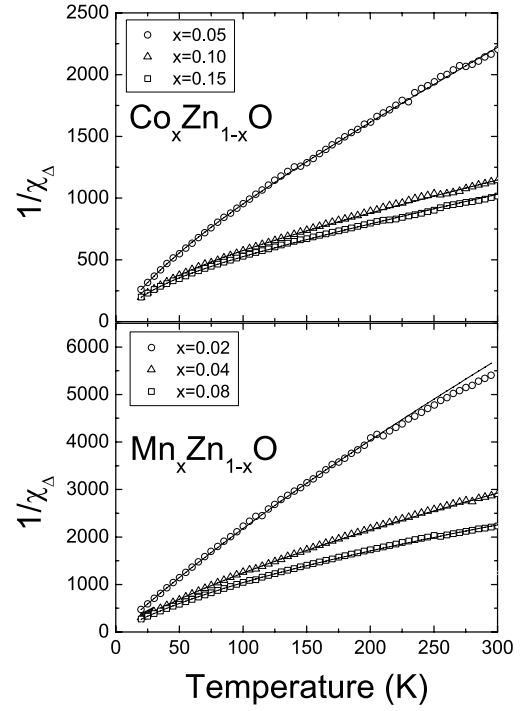


Figure 17 Inverse susceptibility for Co<sub>x</sub>Zn<sub>1-x</sub>O (upper panel) and Mn<sub>x</sub>Zn<sub>1-x</sub>O (lower panel) as a function of temperature. The susceptibility was determined by looking at the difference in magnetization between  $B = 2$  T and  $B = 1$  T. The solid lines show fits to the function defined by separating the TM ions into two subset of spins (after ref. 125. Courtesy of G. Lawes).

temperature regime that appears to be close to linear, followed by significant curvature at lower temperature, is also observed by other researcher [126]. It is desirable to verify the presence of two distinct spin populations in TM-doped ZnO by using techniques such as electron paramagnetic resonance (EPR) or Mössbauer spectroscopy.

In harmony with theoretical predictions that ferromagnetism in (Zn,Mn)O appears mainly in *p*-type materials, a recent study of carrier effect on magnetic properties of (Zn,Mn)O [148] showed that N-capped Mn<sup>2+</sup>:ZnO nanocrystals exhibits strong ferromagnetism with  $T_C > 350$  K. Furthermore, the magnetization of Mn<sup>2+</sup>:ZnO nanocrystal is enhanced with N-containing molecules absorption onto the surface, or reduced with exposure of Zn vapor. Lim *et al.* [129] observed room temperature ferromagnetism from (Zn,Mn)O thin films deposited on GaAs substrate by RF sputtering. A *p*-type conduction is realized when the films were deposited above 530 °C, so that As can be diffused into ZnO as acceptor. The reported hole concentration is in the lower 10<sup>20</sup>/cm<sup>3</sup> range. These observations provide experimental evidence for theoretical studies, and encourage more detailed studies, especially about the chemical identity of N or As in (Zn,Mn)O, toward elucidating the underlying mechanism of ZnO-based ferromagnetic DMSs.

Ferromagnetic behavior has also been observed in (Zn,Mn)O which is *n*-type or insulating. For example, Jung *et al.* [26] observed ferromagnetic ordering in Zn<sub>1-x</sub>Mn<sub>x</sub>O films grown by Laser MBE. The Curie temperatures in this case were  $T_C = 30$  and  $45$  K for Zn<sub>1-x</sub>Mn<sub>x</sub>O of  $x = 0.1$  and  $0.3$ , respectively. Kim *et al.*

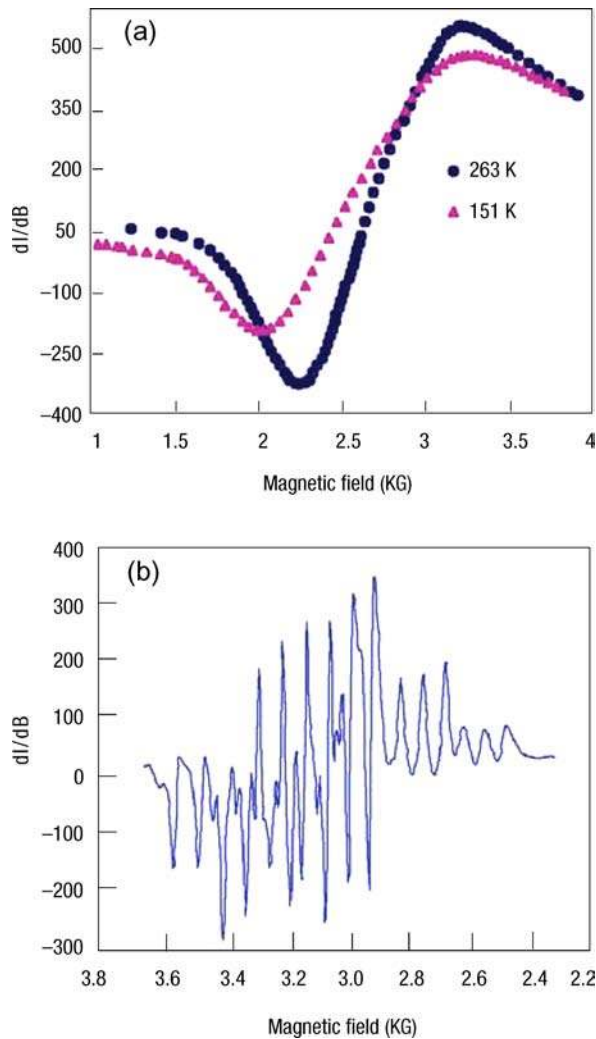


Figure 18 Ferro- and paramagnetic resonance spectra for a nominal 2 at.% Mn doped ZnO pellet. (a) Ferromagnetic resonance spectra sintered at 500 °C. (b) The room temperature paramagnetic resonance spectra for the same sample sintered at 900 °C. (Reprinted with permission from ref. 72. Copyright 2003 Nature Publishing Group.)

[149] also reported  $T_C = 30\text{--}40$  K for  $\text{Zn}_{1-x}\text{Mn}_x\text{O}$  ( $x = 0.1\text{--}0.3$ ) deposited on Si substrate by sol-gel. However, through TEM and EDS measurements the ferromagnetism is considered most probably due to the  $\text{Mn}_3\text{O}_4$  precipitate appeared on the interface between  $\text{Zn}_{1-x}\text{Mn}_x\text{O}$  and Si.

Recently Sharma *et al.* [72] reported ferromagnetism above room temperature in bulk pellets, thin films, and powder form of  $\text{Zn}_{1-x}\text{Mn}_x\text{O}$   $x$  with  $x < 4\%$ . The unique feature of their sample preparation was the low-temperature processing, i.e. sintering temperature less than 700 °C to avoid the formation of secondary phase. Ferromagnetic resonance (FMR) spectra (Fig. 18) showed clear room temperature ferromagnetism for pellets sintered at 500 °C, and  $T_C$  is determined to be well above 425 K although the spectra at 425 K is not shown in their report. Contrary to Sharma *et al.*'s results Kolesnik and coworkers [138] found that  $\text{MnO}_2$  and  $\text{Mn}_2\text{O}_3$  phase exists when the annealing temperature is below 900 °C. Single-phase (Zn,Mn)O fabricated with annealing temperatures higher than 900 °C showed only paramagnetic behavior.

By combining the near-edge X-ray absorption fine structure (NEXAFS) technique and first principles cal-

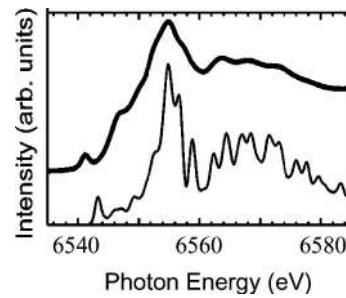


Figure 19 Comparison of NEXAFS spectra between calculations and experiments for polycrystal (Zn,Mn)O with 5% Mn. Thick and thin solid curves are experiments and calculations, respectively. Absolute energies of all theoretical spectra were shifted by  $-20$  eV ( $\Delta E/E = 0.3\%$ ) (after ref. 150. Courtesy of I. Tanaka).

culations, Kunisu *et al.* [150] first studied the local environment of Mn dopant in ZnO. In polycrystalline bulk ZnO NEXAFS at Mn  $K$ -edge was found to remain the same shape as shown in Fig. 19 up to 5%. The experimental spectra is reproduced well by first principles calculation of (Zn,Mn)O solid solution, which confirmed that Mn substituted in Zn sites. For Mn concentration higher than 5%,  $\text{Mn}_3\text{O}_4$  precipitates started to appear.

Based on the idea that Mn provides the localized spins needed for carrier-mediated ferromagnetism, with the additional dopant added to control the carrier concentration in the material, Norton *et al.* [28] reported that ferromagnetic behavior with  $T_C \sim 250$  K is obtained using Mn codoped with Sn in ZnO by PLD. In a more detailed study, Ivill *et al.* [130] investigated the carrier density dependence of saturation magnetization in (Zn,Mn)O with Mn concentration of 3%. Sn is believed to act as a doubly ionized donor introducing deep states in the energy gap. The resistivity of (Zn,Mn)O:Sn films drops from 195  $\Omega\text{cm}$  to 0.185  $\Omega\text{cm}$  as Sn concentration increased from 0 to 0.1 %. The saturation magnetization increases initially with Sn then decreases with increase of Sn concentration, as shown in Fig. 20. This result is interesting but the underlying mechanism between the carrier concentration and magnetic properties observed is not clear, although the authors used the bound magnetron polaron to explain the effect of Sn on the observed magnetization changes by moving up the Fermi energy and changing the hole density.

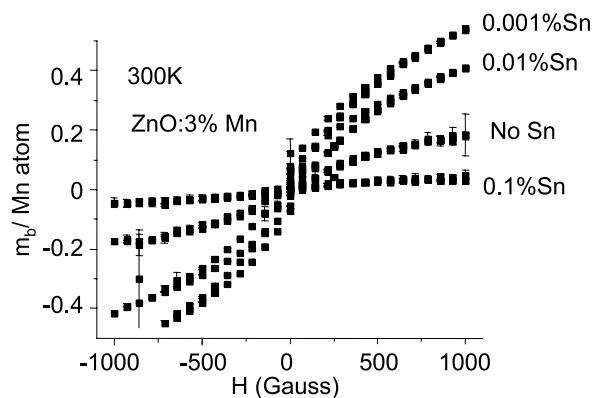


Figure 20 Magnetization measured at 300 K for epitaxial ZnO:3% Mn films that are codoped with 0.001% Sn, 0.01% Sn, 0.1% Sn, and no Sn. There appears to be an inverse correlation of the Sn content with the saturation magnetization (after ref. 130. Courtesy of D. P. Norton).

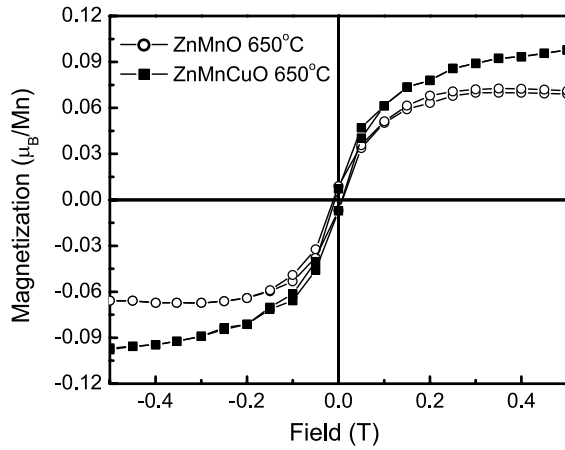


Figure 21 Magnetization vs. magnetic field at 300 K for the  $\text{Zn}_{0.9}\text{Mn}_{0.1}\text{O}$  and  $\text{Zn}_{0.85}\text{Mn}_{0.1}\text{Cu}_{0.05}\text{O}$  thin films fabricated under the same condition (after ref. 136. Courtesy of N. Hong).

In order to confirm the theoretical prediction that Cu-codoping could increase the hole concentration and help induce ferromagnetism in TM-doped ZnO [80],  $\text{Zn}_{0.9}\text{Mn}_{0.1}\text{O}$  and  $\text{Zn}_{0.85}\text{Cu}_{0.05}\text{Mn}_{0.1}\text{O}$  thin films were grown by PLD on *r*-sapphire substrates [136] (Fig. 21). Guided by their results, the authors [136] argued that growth conditions are the very important factors in affecting the magnetic properties of the thin films and Mn doping could indeed induce room temperature FM in ZnO. Codoping with Cu was not found to be very crucial as theories have predicted although it might enhance the magnetic moment in some specific cases. The observed magnetic property changes with growth conditions were attributed to the increase of oxygen vacancies, which act as shallow donors [114] and provide more *n*-type carriers. If this is true, it is clearly opposite to the role of Cu-codoping predicted.

#### 4.2. Properties of Co-doped ZnO

The existence of ferromagnetic ordering in Co-doped ZnO has been first theoretically proposed to be attributed to the double exchange interaction [4, 49] or the RKKY interaction between Co ions [151], but a later calculation also showed that the ground state of Co-doped ZnO is spin glass without doping due to the short range interactions between transition metal atoms [76]. Experimental studies have been carried out in order to verify the predictions. Ueda *et al.* [119] investigated  $\text{Zn}_{1-x}\text{TM}_x\text{O}$  films (*n*-type ( $x = 0.05$ – $0.25$ ) and TM = Co, Mn, Cr, Ni) grown on sapphire substrates by PLD. The Co-doped ZnO films showed the maximum solubility limit of nearly 50%. They first reported the room temperature ferromagnetic feature in  $\text{Zn}_{1-x}\text{Co}_x\text{O}$ , but the reproducibility of the method was less than 10%. Follow up MCD measurements on these samples showed ferromagnetic metal behavior, which indicates that the observed ferromagnetism may be originated from Co-related ferromagnetic precipitates [137]. The ferromagnetism observed in (Zn,Co)O fabricated by ion implantation of Co to (110)-oriented Sn-doped ZnO substrates is also shown to be originated from Co nanoclusters [131].

In a systematic study of magnetism in TM-doped (from Sc to Cu) ZnO, Ventatesan *et al.* [85] reported that the magnetic moment of Co,  $1.9 \mu_B$  per Co, is the largest among all other transition metal elements in (Zn,TM)O with 5% of TM. The films were grown by PLD on *r*-sapphire substrates. Lee *et al.* [29] reported the  $\text{Zn}_{1-x}\text{Co}_x\text{O}$  with  $x = 25\%$  fabricated by sol-gel method exhibits ferromagnetic behavior with  $T_C$  higher than 350 K. The films are insulating with *n*-type carrier concentration in the  $10^{17}\text{cm}^{-3}$  range. In samples with  $x = 20$  and 25% both magnetization and carrier concentration increase with temperature. It is argued that a higher Co concentration could enhance the “trapping” of the electrons, which may induce the ferromagnetic spin-spin interaction between Co atoms. The increase of magnetization with temperature is similar to what is reported for Mn-doped ZnO by Heo *et al.* [27], which has been explained by the effect of randomness and disorder on percolating FM clusters. Tuan *et al.* [135] grew epitaxial  $\text{Zn}_{1-x}\text{Co}_x\text{O}$  ( $x < 35\%$ ) films on *r*-sapphire by MOCVD, and found that a weak ferromagnetic behavior persists even above 350 K. The conductivity was observed increase with post-growth annealing in vacuum instead of Al-doping. The increase of the saturation magnetization with conductivity or carrier concentration observed in these reports [29, 135] seem to agree with some theoretical predictions that electron doping is necessary to induce ferromagnetism in (Zn,Co)O [76]. Ferromagnetism has also been reported by several other groups [132, 152, 153] in (Zn,Co)O with 10–40% of Co.

Similar with the situation in Mn-doped ZnO, there are plenty of reports about the absence of ferromagnetism in Co-doped ZnO as well. Kim *et al.* [35] reported spin-glass behavior for homogeneous  $\text{Zn}_{1-x}\text{Co}_x\text{O}$  films and room temperature ferromagnetism was found only in inhomogeneous films, which led the authors to attribute their observations to the presence of Co clusters. Kane *et al.* [126] investigated bulk  $\text{Zn}_{1-x}\text{Co}_x\text{O}$  and  $\text{Zn}_{1-x}\text{Mn}_x\text{O}$  fabricated by a melt-growth method, and found no evidence of ferromagnetic behavior in any of these nominally noncarrier-doped samples which can be explained by diluted magnetic semiconductor mean-field. The magnetic properties instead showed paramagnetic behavior for  $\text{Zn}_{1-x}\text{Mn}_x\text{O}$  dominated by an anti-ferromagnetic Mn-Mn exchange interaction at low temperatures. Although  $\text{Zn}_{1-x}\text{Co}_x\text{O}$  showed hysteresis, the ZFC and FC magnetization, shown in Fig. 22 revealed that the hysteresis was due to nanoscale paramagnetic Co clusters embedded in a diamagnetic ZnO matrix. The authors concluded that in the bulk single-crystal form, intrinsic and noncarrier-doped  $\text{Zn}_{1-x}\text{TM}_x\text{O}$  is not ferromagnetic; thus creative processing and doping techniques are necessary to achieve practical ferromagnetism in these materials. Paramagnetic behavior has been observed to be dominant in polycrystalline  $\text{Zn}_{1-x}\text{Co}_x\text{O}$  ( $x < 0.15$ ) [154] and bulk  $\text{Zn}_{1-x}\text{Co}_x\text{O}$  ( $x < 0.1$ ) [125].

Consistent with some theoretical predication [80], Lin *et al.* [82] argued that additional Cu doping into bulk  $\text{Zn}_{0.98}\text{Co}_{0.02}\text{O}$  grown by standard solid-state reaction method is essential to achieve room-temperature ferromagnetism. Cu can be doped up to

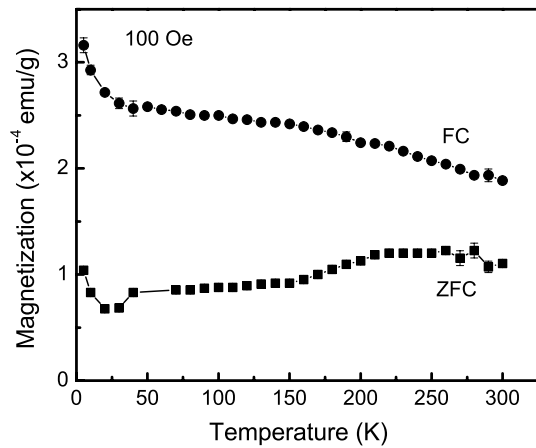


Figure 22 FC and ZFC magnetization vs. the temperature plots taken at 100 Oe for the  $\text{Zn}_{1-x}\text{Co}_x\text{O}$  ( $x = 0.01$ ) sample. Note that the extrapolated slopes versus temperature are of opposite signs in the ZFC and FC curves and there is a significant deviation in these two values. This indicates a superparamagnetic cluster-type behavior (after ref. 126. Courtesy of M. H. Kane).

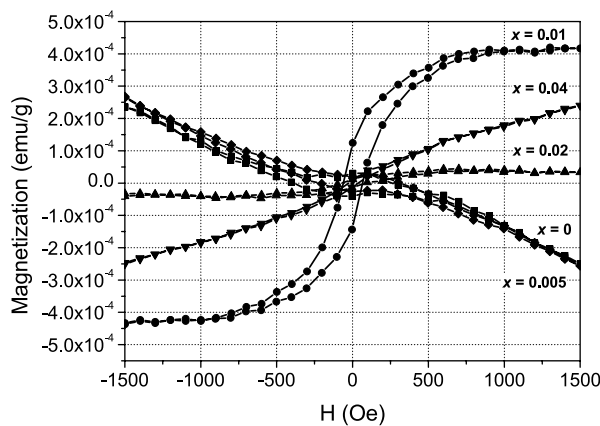


Figure 23 Hysteresis curves measured at room temperature of bulk  $\text{Zn}_{0.98-x}\text{Cu}_x\text{Co}_{0.02}\text{O}$  samples (after ref. 82. Courtesy of T.-S. Chin).

1% ( $\text{Zn}_{0.97}\text{Cu}_{0.01}\text{Co}_{0.02}\text{O}$ ) without forming a secondary phase as confirmed by HRTEM. Saturation magnetization at 300 K increased with Cu concentration (Fig. 23). PL showed increasing peak intensity at 518 nm, which was attributed to defects in ZnO due to the incorporation of Cu and Co, but the UV emission peak diminished with Co or Cu + Co doping.

Substitution of cobalt cations in the tetrahedral sites of the wurtzite structure was confirmed by optical spectroscopy. In its neutral charge state, the  $\text{Co}^{2+}$  ion has an  $[\text{Ar}]3d^7$  electron configuration. The atomic  $^4\text{F}$  ground state splits under the influence of the tetrahedral component of the crystal field into a  $^4\text{A}_2$  ground state and  $^4\text{T}_2 + ^4\text{T}_1$  excited states. The smaller trigonal distortion and spin-orbit interaction split the ground  $^4\text{A}_2$  state into  $\text{E}_{1/2} + \text{E}_{3/2}$ . The existence of the  $\text{Co}^{2+}$  oxidation state has been verified by a series of characteristic optical absorption bands in both the infrared and visible bands that have been correlated with  $d-d^*$  transitions of the high-spin  $\text{Co}^{2+}3d^7(^4\text{F})$  ion in the tetrahedral oxygen coordination. The absorption in the visible band was thought to derive from the  $^4\text{A}_2(^4\text{F}) \rightarrow ^2\text{E}(^2\text{G})$  and  $^4\text{A}_2(^4\text{F}) \rightarrow ^4\text{T}_1(^4\text{P})$  transitions, and those in the infrared from the  $^4\text{A}_2(^4\text{F}) \rightarrow ^4\text{A}_1(^4\text{G})$  transition [155].

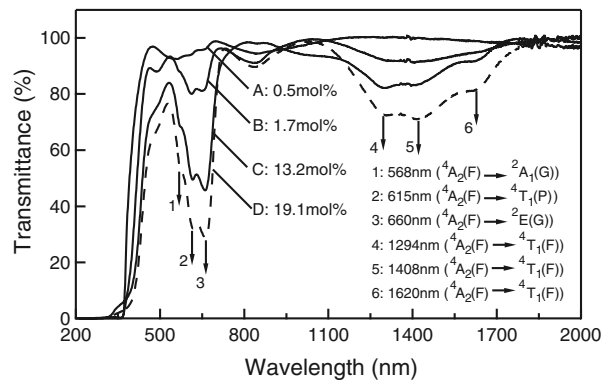


Figure 24 Optical transmission spectrum of  $\text{Zn}_{1-x}\text{Co}_x\text{O}$ . The assignment of the absorption peak is also shown. The dashed line corresponds to the sample showing the solubility limit (after ref. 157).

These  $d-d^*$  adsorption levels of  $\text{Co}^{2+}$  ions have been reported to be around 570, 620, and 660 nm, i.e. 2.18, 2.00, and 1.88 eV, respectively [119, 126, 152, 153, 156, 157]. Fig. 24 shows the optical transmission spectrum for  $\text{Zn}_{1-x}\text{Co}_x\text{O}$  with  $x = 0.05$  to 0.19 [157]. The evidence of  $\text{Co}^{2+}$  state in ZnO lattice has also been obtained from EPR [134] and X-ray photoelectron spectroscopy (XPS) [135] measurements.

#### 4.3. Other TM-doped ZnO

Saeki *et al.* [121] reported Curie temperatures higher than 350 K for V-doped ZnO films [*n*-type  $\text{Zn}_{1-x}\text{V}_x\text{O}$  ( $x = 0.05\text{--}0.15$ )] grown by PLD. They found out that only the samples with carrier concentrations as high as  $10^{18}\text{cm}^{-3}$  showed ferromagnetism, while the insulating samples were not ferromagnetic. The transmittance spectrum for the  $\text{Zn}_{0.95}\text{V}_{0.05}\text{O}$  film was also measured and shows absorption peaks around 480, 560 ( $^4\text{T}_1(e^2t^1) \rightarrow ^4\text{T}_1(e^1t^2)$ ), and 850 nm  $^4\text{T}_1(e^2t^1) \rightarrow ^4\text{A}_2$ , which correspond to typical  $d-d^*$  transitions of  $\text{V}^{2+}$  ions in a tetrahedral crystal field (Fig. 25). Ishida *et al.* [158] investigated the photoemission spectra of ferromagnetic  $\text{Zn}_{0.95}\text{V}_{0.05}\text{O}$ . Fig. 26(a) shows the valence band spectra of  $\text{Zn}_{0.95}\text{V}_{0.05}\text{O}$  recorded in the V 3*p*-3*d* excitation region ( $h\nu \approx 46$  eV). The binding energy structure at 1.8 eV increased considerably on the high binding energy side of the O 2*p* band at the V 3*p*-3*d* absorption edge, which

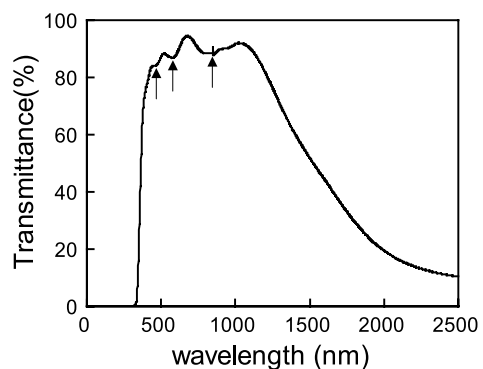


Figure 25 Optical transmission spectra for  $\text{Zn}_{0.95}\text{V}_{0.05}\text{O}$  film. Typical absorption peaks of  $\text{V}^{2+}$  ions are indicated with arrows. (Reprinted with permission from ref. 121. Copyright 2004 Elsevier.)

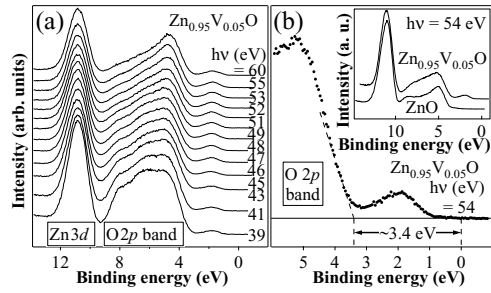


Figure 26 (a) VB spectra of  $\text{Zn}_{0.95}\text{V}_{0.05}\text{O}$  in the  $\text{V}3p\text{-}3d$  excitation region; (b) VB spectra near the Fermi level. In the inset, the VB spectra of  $\text{Zn}_{0.95}\text{V}_{0.05}\text{O}$  and  $\text{ZnO}$  are compared. (Reprinted with permission from ref. 158. Copyright 2004 Elsevier.)

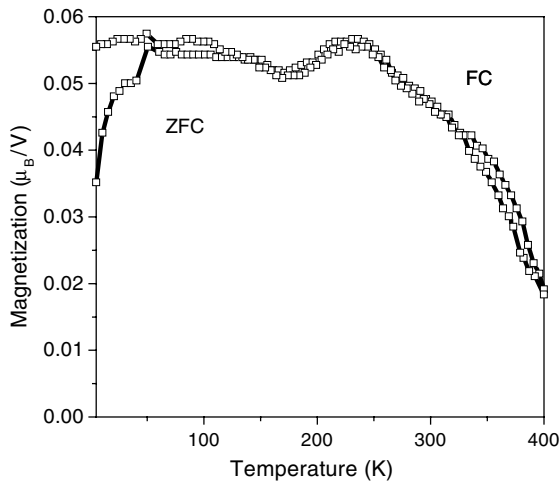


Figure 27 Magnetization of a V-doped film fabricated at  $600^\circ\text{C}$  (a) versus temperature measured at ZFC and FC at 0.2 T (after ref. 159. Courtesy of N. Hong).

indicates the hybridization of  $\text{V } 3d$  into the  $\text{O } 2p$  band. In Fig. 26(b) the 1.8 eV structure is created within the band gap of the host  $\text{ZnO}$ . The Fermi level is estimated to be located near the  $\text{Zn } 4s$  conduction band minimum. It was therefore concluded that the doped electrons in this material which was assumed to induce the ferromagnetism are expected to have strong  $\text{Zn } 4s$  character.

Hong *et al.* [159] reported on magnetic properties of  $\text{Zn}_{1-x}\text{V}_x\text{O}$  thin films deposited on *r*-sapphire substrates by PLD. The films grown below  $650^\circ\text{C}$  (V concentration 8.3 to 11.1%) showed ferromagnetic behavior at room temperature and spin-glass at low temperature, as observed from the ZFC and FC magnetization in Fig. 27. An increase of the substrate temperature above  $650^\circ\text{C}$  seems to favor a secondary phase which is antiferromagnetic.

Magnetic properties of Ni-doped  $\text{ZnO}$  thin films were reported by Wakano *et al.* [120]. Ni was found to dissolve in  $\text{ZnO}$  up to 25% without precipitation. For films doped with 3–25% Ni, ferromagnetism was observed at 2 K. Above 30 K, superparamagnetic behavior was observed. Schwartz *et al.* [160] observed robust ferromagnetism with  $T_C$  above 350 K in Ni-doped  $\text{ZnO}$  nanocrystalline thin films prepared using high-quality colloidal DMS quantum dots as solution precursors. The resultant magnetization hysteresis loops are shown in Fig. 28. In addition to ferromagnetism, substantial superparamagnetism was also evident from the ZFC and

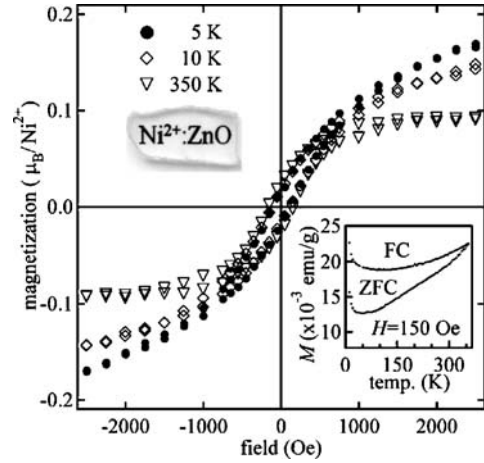


Figure 28 Magnetization hysteresis loops for the spin-coated 1.5%  $\text{Ni}^{2+}:\text{ZnO}$  nanocrystalline thin film at 5, 10, and 350 K. The data have been corrected only for the diamagnetic background of the substrate, measured at 350 K. The optical transparency of the thin film is demonstrated by the image in the upper left inset. The lower right inset shows ZFC and FC magnetization data collected with an applied field ( $H$ ) of 150 Oe (after ref. 160).

FC magnetization data shown in the inset of Fig. 28. When the Ni-doped  $\text{ZnO}$  nanocrystalline was fabricated in a modified process [161], the magnetic properties were influenced remarkably by the aggregation conditions. Distinct ferromagnetism is observed following slow (reaction-limited) aggregation, it is absent or only weakly observed following rapid aggregation.

There were also efforts to produce  $\text{ZnO}$ -based DMS by doping double TM elements such as (Fe, Co) or (Fe, Cu). Cho *et al.* [33] observed room-temperature ferromagnetism for  $\text{Zn}_{1-x}(\text{Fe}_{0.5}\text{Co}_{0.5})_x\text{O}$  films fabricated using reactive magnetron co-sputtering. The samples seem to have the single phase of the same wurtzite structure as pure  $\text{ZnO}$  up to  $x = 0.15$ . A rapid thermal annealing under vacuum led to increases in  $T_C$ , magnetization, and carrier concentration. Han *et al.* [81] also observed ferromagnetism in  $\text{Zn}_{1-x}(\text{Fe}_{1-y}\text{Cu}_y)_x\text{O}$  bulk samples with  $T_C \sim 550$  K. The saturation magnetic moment was determined to be  $0.75 \mu_B$  per Fe, and increases as the Cu-doping ratio increased up to 1%. In addition, a large magnetoresistance was observed below 100 K. The origin of ferromagnetism in  $\text{Zn}_{0.95-x}\text{Fe}_{0.05}\text{Cu}_x\text{O}$  bulk samples mentioned above was investigated using zero-field  $^{57}\text{Fe}$  nuclear magnetic resonance and neutron diffraction [145]. These measurements revealed that at low concentrations Cu doping into  $\text{Zn}_{0.95-x}\text{Fe}_{0.05}\text{Cu}_x\text{O}$  causes the formation of  $\text{ZnFe}_2\text{O}_4$  nanoclusters with inverted spinel structure, which is ferrimagnetic at room temperature. Ferromagnetism in Fe- and Cu-codoped  $\text{ZnO}$  stems from the secondary phase, while the majority of Fe ions substituted into the  $\text{ZnO}$  lattice appears to remain magnetically inert.

Because of a lack of detailed microstructural characterization in some of the reports mentioned above, there is still a good deal of controversy over the fate of these magnetic impurities (nanosize clusters/precipitates and/or individual atoms in substitutional sites) and whether the magnetic behavior is an intrinsic property of the films or due to the presence

of nanoclusters of a magnetic phase or a combination of both. In addition to macroscopic characterization, the detailed lattice structure, especially surrounding the transition metal ion in the lattice, information on the magnetic state of these ions and the electronic state of the TM ions in a high concentration range are of fundamental importance in order to understand the interplay between carrier concentration and magnetic exchange coupling. As seen in the discussion, there are still notable variations in the reported magnetic behavior, with some films exhibiting only paramagnetism and even those with ferromagnetism showing a wide range of apparent Curie temperatures. Although considerable research resulted in the observation of spontaneous magnetic moment at or above room temperature, the magnetic moment is much smaller than that expected from the concentration of the magnetic dopants, for example,  $1.35 \mu_B/\text{Mn}$  [148] as compared to the predicted value of  $\sim 4 \mu_B/\text{Mn}$ . In short, the origin of the observed ferromagnetism needs further clarification.

#### 4.4. Magneto-optical properties of ZnO-based DMSs

As mentioned earlier SQUID magnetization measurements are so sensitive that the results are easily affected by the magnetic participation from the substrate and other magnetic contaminants. On the other hand, magneto-optical spectroscopy probes the magneto-optical signal as a function of photon energy, and can be used to probe the magnetic properties of the DMS materials only. The magneto-optical effect in dilute magnetic semiconductors is directly related to the interaction between the  $d$ -electrons of the transition metal ions and the  $s,p$  electrons of the host semiconductor. Particularly, MCD spectroscopy is useful for thin film study because effect of substrate on the spectrum is negligible contrary to magnetization measurement. The MCD signal is generally enhanced at the absorption edge of DMS host semiconductor [30, 31, 162], as a result of carrier-mediated exchange interaction between localized spins. When the MCD signal is proportional to the applied magnetic field one can surmise paramagnetic behavior.

Ando *et al.* [163, 164] discussed the advantages of magneto-optical spectroscopy for characterizing

DMSs. MCD can be used to detect the difference in optical absorption or reflection for left and right circularly polarized light in the presence of a magnetic field parallel to the light propagation direction. It is well known that an external magnetic field causes Zeeman splitting of the atomic energy levels. In DMS, the magnetic field effect on the  $s,p$ -band electrons is amplified by the magnetic moment of the transition metal ion through the  $s,p$ - $d$  exchange interaction causing enhanced splitting of the band structure. A strong MCD signal indicates a strong  $s,p$ - $d$  exchange interaction, and the polarity (positive or negative) of the MCD signal at critical point energies can be used to interpret the polarity of the exchange constant. To make the point clearly the schematic band splitting of  $\text{Cd}_{1-x}\text{Mn}_x\text{Te}$  at the  $\Gamma$  point, which has been studied in detail, is shown in Fig. 29 [164]. Each material has its own set of critical point (CP) energies reflecting its electronic band structure. The CP of the band structure will clearly show up in the MCD spectrum, which provides a fingerprint for each material. This allows the identification of the material that is responsible for the observed MCD signal.

Intrinsic ferromagnetism in  $\text{In}_{1-x}\text{Mn}_x\text{As}$ ,  $\text{Ga}_{1-x}\text{Mn}_x\text{As}$ , and  $\text{Zn}_{1-x}\text{Cr}_x\text{Te}$  has been confirmed by using MCD spectroscopy [163]. To investigate the magneto-optical properties of ZnO, Ando *et al.* [30] measured the MCD spectra in films alloyed with Sc, Ti, V, Cr, Mn, Co, Ni, and Cu using pulsed laser deposition. Fig. 30 shows the MCD spectra of (0001) oriented (Zn,TM)O films. The high quality of the ZnO film grown on a lattice-matched  $\text{ScAlMgO}_4$  substrate leads to a small but clear MCD structure at the band gap 3.4 eV. Other films were grown on lattice-mismatched  $\text{Al}_2\text{O}_3$  substrates. ZnO films doped with Mn, Fe, Co, Ni and Cu show clear MCD structures near 3.4 eV. Therefore, the authors argued that these TM-doped ZnO are DMSs. The films alloyed with Sc, Ti, V, and Cr did not show any noticeable magneto-optical effect and could therefore be deemed as antiferromagnetic. The magnetic field and temperature dependence of the MCD spectra show that all of these films are paramagnetic. Characterization of the  $s,p$ - $d$  exchange interaction has been one of the main topics for the II–VI based DMSs. The confirmation of the  $s,p$ - $d$  exchange interaction is the most important task to be carried out when new true DMS materials are attempted to be synthesized.

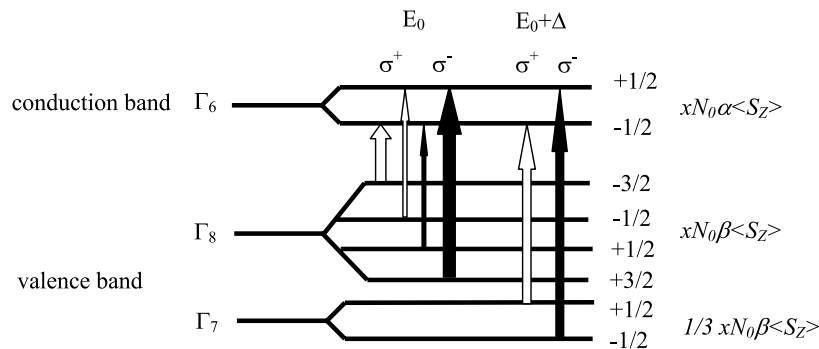


Figure 29 The schematic band splitting of  $\text{Cd}_{1-x}\text{Mn}_x\text{Te}$  at the  $\Gamma$  point. Here  $x$  is the concentration of magnetic ions, and  $\langle S_z \rangle$  is the average component of the spin of the magnetic ion along the external field in the  $z$  direction.  $N_0\alpha$  is the  $s$ - $d$  exchange constant, and  $N_0\beta$  is the  $p$ - $d$  exchange constant.  $\sigma^+$  presents the right circular polarization, and  $\sigma^-$  presents the left circular polarization (after ref. 164).



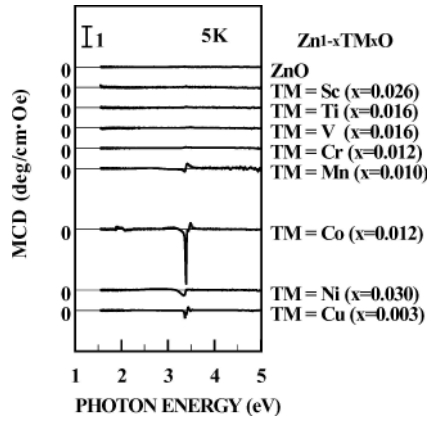


Figure 30 Transmission MCD spectra of ZnO and ZnO:TM (after ref. 30. Courtesy of K. Ando).

Cathodoluminescence (CL) measurements of the TM-doped samples [123] showed two peaks at 2.97 and 3.71 eV for Cr-doped samples at the expense of the exciton emission peak of pure ZnO. The authors argue that these peaks are due to oxygen-rich local structures caused by Cr-doping, since similar but broader peaks were also observed in undoped ZnO thin films treated under oxygen rich conditions [165]. We should mention that this correlation is not necessarily a solid one as material development is in its infancy and there is good deal of variation from wafer to wafer, the cause of which is not yet well understood. Continuing on, CL measurements also revealed that Mn is a quencher of luminescence. Despite all these results, no indication of ferromagnetism was observed for  $\text{Zn}_{1-x}\text{TM}_x\text{O}$  (TM = Sc, Ti, V, Cr, Mn, Fe, Co, Ni, Cu) films down to 3 K. Magneto-optical response (measured by MCD) is consistent with the absorption spectra observed for Mn- and Co-doped samples [123].

## 5. Experimental results of TM-doped GaN

The discovery of ferromagnetism in (Ga,Mn)As and the prediction that high  $T_C$  ferromagnetic DMS could be realized by TM-doped GaN have spawned a great deal of recent experimental interest in examining and understanding the magnetic behavior of GaN-based DMSs. The magnetic properties of recently reported TM-doped GaN are listed in Table VI. In this section, we will give a detailed review on recent progress in experimental studies in Mn-, Cr-, and other transition-metal-doped GaN.

### 5.1. Magnetic properties of Mn-doped GaN

Many of the Mn doped GaN layers have been prepared by MBE at relatively low temperatures in order to increase Mn incorporation. High concentration of magnetic ions, up to a point, is imperative for ferromagnetic behavior. Some researchers [7, 8] have reported single phase (Ga,Mn)N layers by gas-source MBE, which contained 3–9% Mn, showing the room temperature M-H magnetization loops. Of those samples, the material with 3% Mn composition showed the highest degree of magnetic ordering per Mn atom, and a  $T_C$  of 320 K. However, a Mn concentration higher than 9% was found to enhance the antiferromagnetic coupling, resulting in a lower magnetic moment per Mn.

The highest  $T_C$  reported so far in Mn-doped GaN is by Sasaki *et al.* [167] who prepared their (Ga,Mn)N layers on (0001) sapphire by reactive MBE using ammonia for N source. They observed Curie temperatures as high as 940 K, which is astonishing to say the least as the thermal agitations would be substantial at temperature approaching that value, while acknowledging the coexistence of ferromagnetic and paramagnetic phases in their samples.

TABLE VI List of recently reported magnetic properties of ZnO-based DMS. The TM content listed corresponds to the magnetic property and  $T_C$  in the “Note” and “ $T_C$ ” columns. 4H-SiC substrate is one of the polytypes of SiC. For more information about properties of SiC and sapphire substrate, the readers are referred to Ref. 166

Compound	TM content	Substrate (for thin film) or bulk	Fabrication method	Growth temperature (°C)	Post-annealing	$T_C$ (K)	Notes	Reference
(Ga,Mn)N	0.01–0.02	p-GaN	Solid state diffusion		250–800 °C	220–370	Ferromagnetic	14
(Ga,Mn)N	0.03	c-sapphire	MBE	580–720		940	Ferromagnetic	167
(Ga,Mn)N	0.07	c-sapphire	MBE	865		10–25	Ferromagnetic	8
(Ga,Mn)N	0.01–0.03	p-GaN	Ion implantation	350	700–1000 °C	250	Ferromagnetic	6
(Ga,Mn)N	0.02	Bulk	Ammonothermal & resublimation	1200–1250		>425	Para+ ferromagnetic	15
(Ga,Mn)N	0.07–0.14	4H-SiC (0001)	MBE	710		750	Ferromagnetic, from Mn cluster	108
(Ga,Cr)N	0.03	Bulk	Sodium flux growth	750		280	Ferromagnetic	19
(Ga,Fe)N	0.1	p-GaN	Implantation		700–900 °C	>350	Ferromagnetic	24
(Ga,Cr)N		c-sapphire	ECR-MBE	700		>400	Ferromagnetic	20
(Ga,Mn)N	0.07	4H-SiC (0001)	MBE	710			Spin-glass	168
(Ga,Co,V)N	0.03–0.05	p-GaN	Ion implantation	350	5 min at 700 °C		V: paramagnetic Co: spin glass	23
(Ga,Cr)N	0.03–0.05	p-GaN	Ion implantation	350	5 min at 700 °C	>300	Ferromagnetic	23
(Ga,Mn)N	0.01–0.03	p-GaN	Ion implantation	350	5 min at 950 °C in N <sub>2</sub>	>300	Ferromagnetic	169

Dhar *et al.* [106, 108] presented investigations of the magnetic properties of (Ga,Mn)N layers grown on 4H-SiC substrates by reactive MBE. Employing a variety of techniques such as X-ray diffraction and TEM, they confirmed that homogeneous (Ga,Mn)N alloys of high crystallographic quality could be synthesized for Mn concentrations up to 10–12%. Relying on the measurements of temperature-dependent dc magnetization, isothermal remnant magnetization, and frequency and field dependent ac susceptibility, those author concluded that the insulating (Ga,Mn)N alloys behaved as a Heisenberg spin-glass with a spin-freezing temperature around 4.5 K. This was attributed to the deep-acceptor nature of Mn in GaN which in turn resulted in the insulating character of the compound. In other reports by the same group, Dhar *et al.* [108] and Ploog *et al.* [168] also showed evidence for Mn-rich clusters being embedded in the (Ga,Mn)N alloy matrix to which ferromagnetic behavior was ascribed.

Cubic (Ga,Mn)N in its metallic phase has been predicted [170] by Monte Carlo simulations to be ferromagnetic with  $T_C$  in excess of room temperature. Chitta *et al.* [169] reported that a *p*-type cubic (Ga,Mn)N exhibited room temperature ferromagnetism, determined by the M-H hysteresis. The cubic GaN material was grown by MBE on GaAs (001) substrates, followed by Mn ion implantation that translated into Mn composition of 0.7 to 2.8%. After annealing at 950 °C, all samples showed sustained M-H hysteresis up to 300 K. Temperature dependent magnetization measurements for both FC and ZFC conditions confirmed the similarity to hexagonal GaN in terms of magnetic properties. The origin of the observed ferromagnetism was not clearly specified.

Incorporation of Mn into GaN nanowires has also been reported. Deepak *et al.* [171] reported the synthesis of (Ga,Mn)N nanowires with average diameter of two different groups of nanowires to be 25 nm and 75 nm, respectively, and with Mn concentration of 1%, 3%, and 5%. All the layers showed magnetic hysteresis at 300 K. The  $Mn^{2+}$  related peak was observed in PL measurements, with a significant blue shift of this  $Mn^{2+}$  related emission for the 25 nm diameter nanowires as compared to the 75 nm ones. In the same vein, Han *et al.* [13] reported Mn-doped GaN nanowires with 5 at.% of Mn being ferromagnetic with a Curie temperature of at least 300 K, as evidenced by the M-H hysteresis and the temperature dependent FC and ZFC measurements.

In most of the reported experimental results, M-H hysteresis data have been used as a measure of ferromagnetism and Curie temperature. However, it is well known that the magnetization curves alone are not sufficient for a conclusive statement on the matter and could in fact be misleading at times. Pearton *et al.* [43] analyzed three samples, i.e. (Ga,Mn)N with 5% Mn (single phase), 50% Mn (contains multiphase of  $Ga_xMn_y$ ) or 5% Mn (contains small amount of multiphase  $Ga_xMn_y$ ). All of which showed magnetization hysteresis loops at room temperature. But in the temperature behavior under FC and ZFC magnetization, which is more instructive than accurate test of ferromagnetism, three samples showed different be-

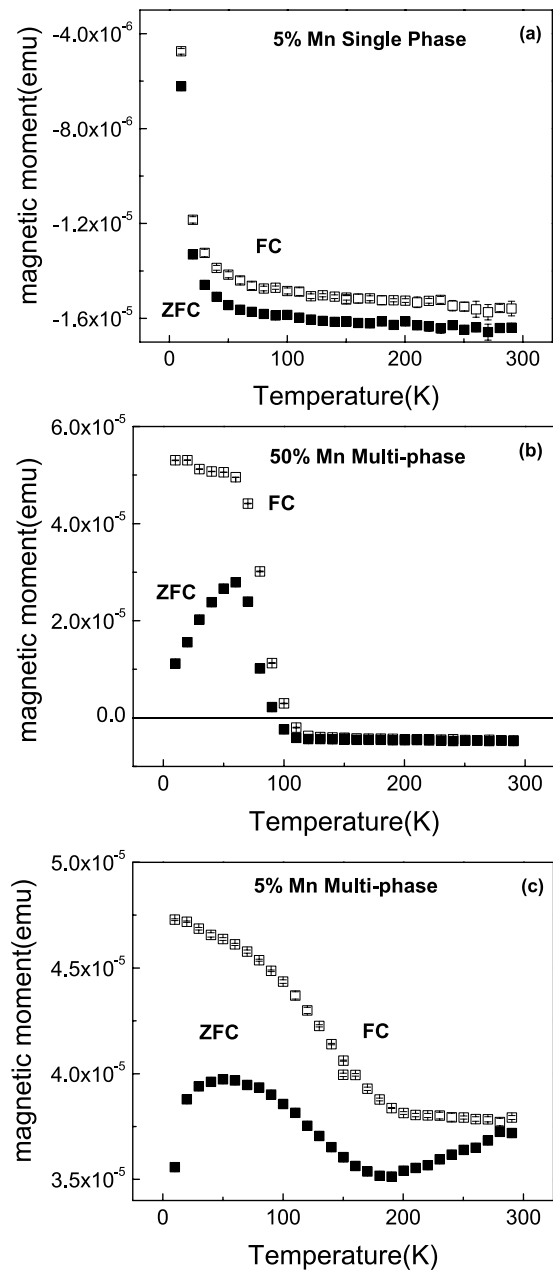


Figure 31 Temperature dependence of field cooled (FC) (top curve in each case) and zero field cooled (ZFC) (bottom curve in each case) magnetic moment for (Ga,Mn)N with (a) 5 at.% Mn (optimized growth), (b) 0.5 at.% Mn or (c) 0.05 at.% Mn (unoptimized growth) (after ref. 43. Courtesy of S. J. Pearton).

haviors as indicated in Fig. 31. Only the single phase (Ga,Mn)N sample with 5% Mn, shown in Fig. 31(a), shows ferromagnetism persisting above 300 K as evidenced by the separation between FC and ZFC curves. In contrast, the  $x = 0.5$  multi-phase (Ga,Mn)N sample (Fig. 31(b)) showed behavior consistent with spin glass behavior below 100 K. The multi-phase  $x = 0.05$  (Ga,Mn)N sample shows behavior consistent with the presence of at least two ferromagnetic phases as shown in Fig. 31(c). These experiments demonstrated that the conclusion of the magnetic properties of DMS materials should not rely only on the magnetization hysteresis. Detailed characterization, especially about the magnetization state of the substitutional transition metal ions, are necessary for a better understanding of the origin of magnetism in these materials.

Despite many reports of evidence for ferromagnetism in Mn-doped GaN, there are also reports to the contrary [15, 172]. In an effort to show that precipitates could be the source of reported ferromagnetism, Zajac *et al.* [15] grew both (Ga,Mn)N and the reference  $\text{Mn}_x\text{N}_y$  samples using similar growth parameters such as temperature and pressure. Then the magnetic properties of the samples were investigated in an attempt to determine whether the ferromagnetism observed in Mn-doped GaN could be due to magnetic material inclusions. Based on the ferromagnetic behavior observed from  $\text{Mn}_x\text{N}_y$ , it was suggested that the ferromagnetic behavior in Mn-doped GaN could be from  $\text{Mn}_x\text{N}_y$  precipitates that could form under the same growth conditions although they may not be *undetectable* by X-ray diffraction.

For the negative column, employing MCD spectra to study a room-temperature ferromagnetic (Ga,Mn)N film, Ando [32] showed that the film contained  $\text{Ga}_{1-x}\text{Mn}_x\text{N}$  in which the band *s,p* electrons interacted with the *d*-electrons of the Mn ions. Further, both the magnetic field dependence and the temperature dependence of the MCD intensity confirmed that  $\text{Ga}_{1-x}\text{Mn}_x\text{N}$  was a paramagnetic diluted magnetic semiconductor and it was thus postulated that the ferromagnetism of the sample arose from some unidentified material which may not be detectable by X-ray diffraction. On an equally serious note, holes have been reported to be at the *d* shell of Mn ( $\text{Mn}^{2+}(d^5)$ ) by several researchers [173–175], implying that magnetization induced by hole exchange interaction may not be plausible in (Ga,Mn)N.

Reed *et al.* [176] proposed that in (Ga,Mn)N when the Fermi position is such that there is a partial occupancy of electrons and holes in this Mn impurity band, ferromagnetic behavior occurs. The (Ga,Mn)N thin films were grown by MOCVD by using  $(\text{EtCp})_2\text{Mn}$  precursor. Their suggestion needs to be considered in terms of Mn induced levels/bands within the bandgap in order to devise a scientific explanation of these observations. The dependence of ferromagnetic properties on the Fermi level was demonstrated by doping (Ga,Mn)N with *n*-type or *p*-type dopants. Shown in Fig. 32 is the effect of silane flow to the saturation magnetization of the (Ga,Mn)N : Si films. The data indicate that high silicon concentrations in (Ga,Mn)N : Si films eliminate the FM behavior determined by magnetization curves, whereas a much stronger FM response was observed for low to moderately Si doped samples. In the case of high Si doping, it is expected that  $E_F$  is close to the conduction band, therefore, the argument goes that the deep Mn band is completely filled with electrons, leaving no available holes to mediate the magnetic exchange interaction. When doped with Mg, electrons in the Mn impurity band are absorbed by the normally empty Mg acceptor states that is  $\sim 1.2$  eV below the Mn band, so that these electrons have nearly zero probability of returning to the Mn energy band where they would facilitate the Mn-Mn exchange interaction. Therefore, the addition of Mg to an otherwise FM (Ga,Mn)N film is expected to reduce the FM response, and the introduction of Mg acceptor states at a same concentration

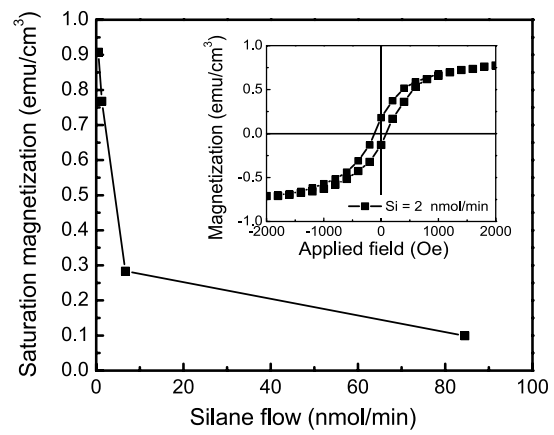


Figure 32 The effect of silane flow on the saturation magnetization of (Ga,Mn)N : Si films. Inset shows the magnetization curve for sample at low magnetic fields, which is typical of the samples used in this study. This sample has a residual magnetization of 0.154 emu/cm<sup>3</sup>, a coercivity of 100 Oe, and saturation magnetization of 0.72 emu/cm<sup>3</sup> at 2.2 kOe, at room temperature (after ref. 176).

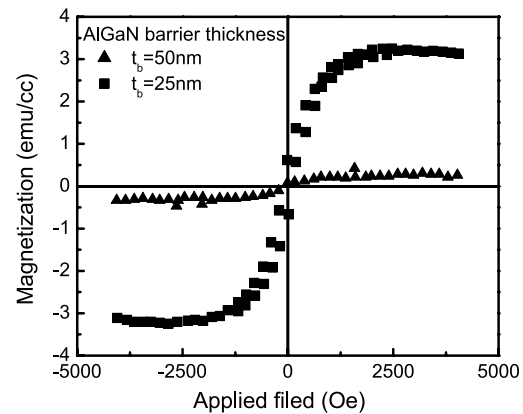


Figure 33 Magnetization vs applied field for GaN:Mg/AlGaN/(Ga,Mn)N/AlGaN/GaN:Mg DHS containing 25- and 50-nm-thick AlGaN barriers. The thickness of the (Ga,Mn)N and GaN : Mg layers are fixed at 0.38 and 0.75  $\mu\text{m}$ , respectively (after ref. 177. Courtesy of F. E. Arkun).

of the Mn nearly eliminates the film's FM response, as it is observed. The same group at North Carolina State University reported on the dependence of ferromagnetic properties of MOCVD grown (Ga,Mn)N films on carrier transfer across adjacent layers [177]. They found that the magnetic properties of (Ga,Mn)N, as part of (Ga,Mn)N/GaN : Mg heterostructures, depend on the thickness of the GaN : Mg layer. These results were explained based on the occupancy of the Mn energy band and how the occupancy can be altered due to carrier transfer at the (Ga,Mn)N/GaN : Mg interfaces. They also found that the magnetic properties of the GaMnN/AlGaN/GaN : Mg depends on the thickness of the AlGaN barrier layer, shown in Fig. 33. The presence of this AlGaN barrier layer thus affects the carrier transfer from the GaMnN film to the GaN : Mg layers. These results agree with the models proposed by Kronik *et al.* [94] and Dalpian *et al.* [99] in that ferromagnetic state can only be stabilized when Mn levels are partially filled, and clearly demonstrated the carrier-mediated ferromagnetism in (Ga,Mn)N.

The question whether Mn-doped GaN is ferromagnetic or not is still unresolved in the literature. In those

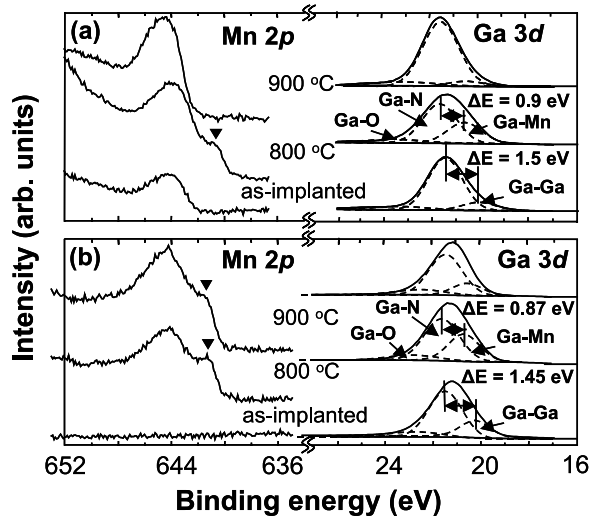


Figure 34 SPRES spectra of Mn  $2p_{3/2}$  and Ga  $3d$  core levels as a function of annealing temperature: (a) Mn-implanted and (b) (Mn + N) co-implanted GaN (after ref. 178. Courtesy of J.-L. Lee).

instances where ferromagnetism has been reported, the Curie temperatures span an interval from 20 K to 940 K. Although the growth mechanism seems to play a vital role, the reason for such a wide variation of  $T_C$  is not understood and it is reasonable to speculate about the likelihood of contributions from materials other than the (Ga,Mn)N proper, if any. There is still a long way to go before a firm ground can be laid for the science regarding ferromagnetism in III-nitride.

## 5.2. Structural properties of Mn-doped GaN

As already touched on, one needs to ascertain that the material under test does not contain second phases, namely some form of Ga-Mn binary that might be responsible for hysteretic M-H curves. In this vein, the

EXAFS technique is very useful. The method has been exploited to probe the local atomic structure involving coordination and chemical environment around atomic sites in *p*-type GaN-based DMS by Baik *et al.* [178, 179], namely GaN thin films implanted with Mn, or co-implanted with Mn and N. After annealing, it was found that the ferromagnetic signal increased and persisted up to room temperature as N ions were implanted into the Mn-implanted GaN. The particular EXAFS analysis showed that Mn ions occupied the Ga sites to form (Ga,Mn)N. By implanting N, the Mn concentration occupying Ga sites increased from 2.5 to 3.8% for the same Mn dose, while the formation of Mn-N compounds was effectively inhibited. However, synchrotron radiation photoemission spectroscopy (SRPES) investigations confirmed that the Ga-Mn phase increased as depicted in Fig. 34, where the peak intensity of Ga-Mn bond increased following N ion implantation. Note that in the figure for the case of Mn implantation alone the Ga-Mn peak vanished after 900 °C annealing. But in the case of Mn and N co-implantation, the Ga-Mn bond remained after 900 °C annealing. As a result, it was assumed that the N-vacancies reduced and the Ga-Mn magnetic phase increased, leading to enhanced ferromagnetic properties. It should be pointed out here that unless the nature of Mn in those GaN samples is determined precisely, it is highly speculative to imply that the samples are *p*-type.

Ploog and co-workers [108, 168] reported detailed microstructural studies of their (Ga,Mn)N layers grown on 4H-SiC substrates by reactive MBE utilizing  $\text{NH}_3$  as the nitrogen source. The high-resolution TEM images shown in Fig. 35 revealed that for lower Mn compositions (7.6% and 10.3%), homogeneous (Ga, Mn)N ternary alloys of high crystalline quality could be formed, while those with higher Mn content (above 12%) contain Mn-rich clusters embedded in the

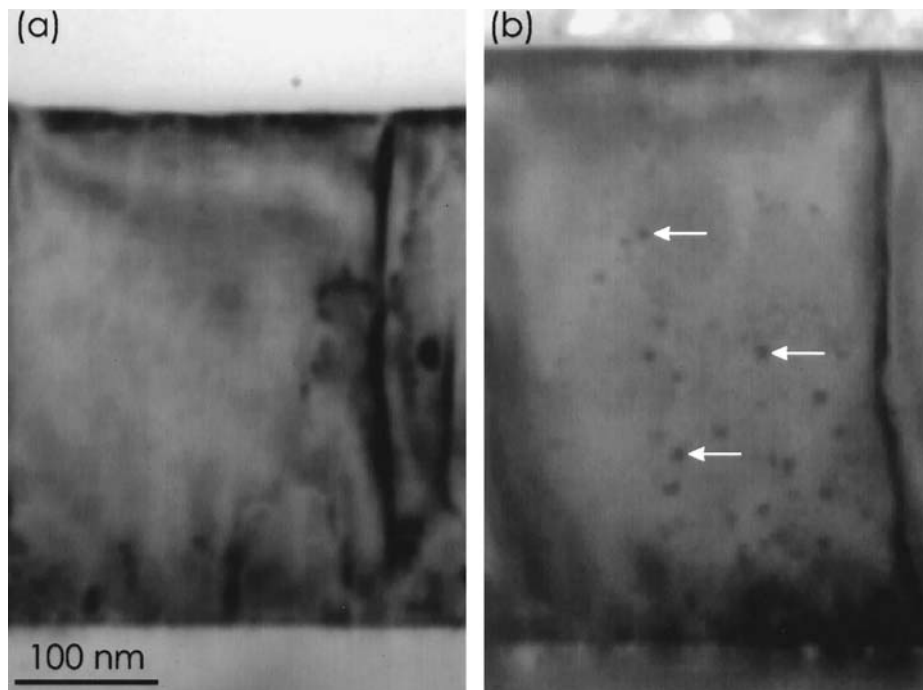


Figure 35 Bright-field TEM micrographs showing (a) homogeneous alloy of  $\text{Ga}_{0.924}\text{Mn}_{0.076}\text{N}$ , and (b) Mn-rich clusters in  $\text{Ga}_{0.863}\text{Mn}_{0.137}\text{N}$  epilayers grown on 4H-SiC by reactive MBE (after ref. 108).

(Ga,Mn)N alloy matrix. Below 10 K, both types of samples are antiferromagnetic, characteristic of a spin-glass transition. The sample containing Mn clusters exhibit ferromagnetic properties even far above room temperature, which was attributed directly to Mn clusters in the alloy. It should also be mentioned that Mn-doped GaN is generically reported as an alloy regardless of whether any attempt has been made to determine if the Mn in the lattice is of the bonding type. This confusion in fact manifests itself in the nomenclature as well as (Ga,Mn)N terminology depicts in general the alloy while Mn-doped GaN depicts Mn to be only a dopant. In fact, both may be present simultaneously in the sample.

Structural properties of (Ga,Mn)N which have been reported to play a critical role in the magnetic properties are often closely tied to growth parameters, such as the nucleation layer, growth temperature, and Mn concentration. A study of the effects of the nucleation layer and growth temperature on the magnetic properties of (Ga,Mn)N showed [104] that the largest magnetic moment ensues in the films prepared at a growth temperature of 700 °C on MOCVD GaN buffers. EXAFS measurements indicate that the improved magnetic quality of the films grown on MOCVD layers versus gas source MBE (GS-MBE) nucleation layers is not due to a change in the lattice position of the Mn but more likely due to a reduction in defect density. The growth temperature was also found to have a significant impact on the magnetic properties, with the optimal growth temperature being around 700 °C. Researchers from the same group also investigated the effect of Mn concentration [180] on the properties of (Ga,Mn)N grown by gas source-MBE by varying the Mn content between 0 to 9 at.%. High-resolution XRD measurements show that the *c*-plane lattice constant initially decreased with increasing Mn concentration, then increased when the Mn content increases above ~3 at.%. The comparison between a single-phase (Ga,Mn)N and Ga<sub>x</sub>Mn<sub>y</sub>-containing (Ga,Mn)N was made in the form of Fourier transform of the Mn K-edge  $\chi$  function versus the lattice position measured by EXAFS, as shown in Fig. 36,

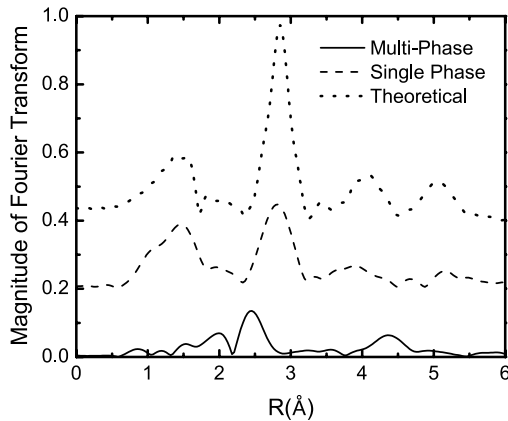


Figure 36 Mn K-edge EXAFS  $\chi$  functions for (Ga,Mn)N films with 5% Mn concentration. The single phase film was grown using optimized nitrogen plasma settings while the multiphase film was not, resulting in the formation of Ga<sub>x</sub>Mn<sub>y</sub>, in addition to the (Ga,Mn)N. The theoretical spectrum for GaN containing 5 at.% substitutional Mn is also shown (after ref. 180. Courtesy of G. Thaler).

together with the theoretical prediction for single-phase (Ga,Mn)N. The peaks obtained from the film known to possess Ga<sub>x</sub>Mn<sub>y</sub> clusters are shifted significantly from the film believed to be single phase. This suggests that the nonsubstitutional Mn in the single-phase (Ga,Mn)N sample is not present in the form of Ga<sub>x</sub>Mn<sub>y</sub> clusters and thus is most likely present as interstitials.

### 5.3. Electrical and optical properties of Mn-doped GaN

Electrical transport measurements can be used to provide dependable information regarding the magnetic ordering in (Ga,Mn)N thin films. The equation of motion in a semiconductor under a magnetic field can be used to determine the conductivity or resistivity matrix elements [166]. Due to the magnetic field, the off diagonal terms are not necessarily zero. The off diagonal term in DMS materials has a normal and a magnetic component expressed as:

$$\rho_{xy} = \rho_{xy}^0 + \rho_{xy}^s = R_o B + R_s \rho_{xx} M$$

where  $\rho_{xy}^0$  and  $\rho_{xy}^s$  represent non magnetic (normal) and magnetic (anomalous) components, of the off-diagonal resistivity matrix element, respectively. The terms  $R_o$  and  $R_s$  represent the normal and anomalous Hall coefficients, and  $M$  is the magnetization of the sample. In decidedly ferromagnetic samples the second term on the right hand side dominates and the first term can be neglected. If additionally, the skew scattering is the dominant process, the anomalous Hall coefficient would be proportional to the sheet resistance of the sample [2]. Thus  $M$  can be calculated from the above expression as being proportional to the ratio of the Hall coefficient to the sheet resistance. Eventually, if ZnO and GaN based DMS advances to the point where reliable Hall measurements can be made, the anomalous Hall effect would be a reliable means of determining whether the material is ferromagnetic and what the Curie temperature is.

Let us now turn our attention to optical properties of Mn-doped GaN. Some background information is necessary to facilitate the discussion as well as getting acquainted with the terminology used. The neutral configuration of Mn in GaN is Mn<sup>3+</sup>(A<sup>0</sup>) when viewed as replacing Ga<sup>3+</sup> in the lattice. In a II–VI material only the 4s<sup>2</sup> electrons would be needed for bonding and as such the Mn<sup>2+</sup>(d<sup>5</sup>) configuration is the neutral state. Owing to the metal oxide compound terminology, this state is also called the oxidation state which is also the neutral state in relation to the lattice. The configuration of Mn in GaN as an ionized acceptor is Mn<sup>2+</sup>(d<sup>5</sup>), with five tightly bound electrons in the Mn *d* shell. The neutral configuration of Mn<sup>3+</sup>(A<sup>0</sup>) may be realized in two ways, as Mn<sup>3+</sup>(d<sup>4</sup>) with four electrons localized in the Mn *d* shell [181] or as a Mn<sup>2+</sup>(d<sup>5</sup>) + hole with five electrons in the Mn *d* shell and a band hole weakly bound in a delocalized orbit [182]. In contrast to GaAs where Mn is a relatively shallow acceptor ( $E_A \sim 0.11$  eV) providing high concentration of free holes at room temperature, the Mn level in GaN is

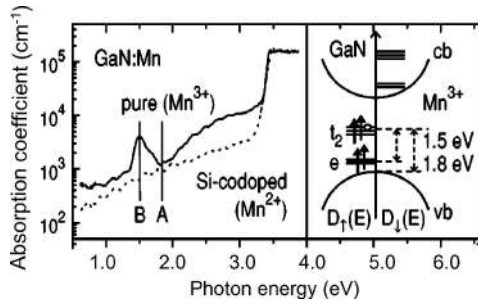


Figure 37 Optical absorption of (Ga,Mn)N and (Ga,Mn)N:Si with  $[Mn] \sim 10^{20} \text{ cm}^{-3}$ . Transition A with the onset around 1.8 eV in GaN is assigned to the direct emission of holes from  $Mn^{3+}$  acceptors to the valence band, and transition B around 1.5 eV to the internal spin-allowed  $^5E \rightarrow ^5T$  transition of the deep neutral  $Mn^{3+}$  state, as shown in the inset with the spinpolarized one-electron densities of states  $D\uparrow(E)$  and  $D\downarrow(E)$  (after ref. [173]).

believed to be almost in the middle of the band gap [173, 174, 183–185], and one cannot expect detectable transport of holes bound to Mn acceptor even at very high concentrations of Mn, unless a band is formed and conduction takes place within that band.

Graf *et al.* [173, 174] have demonstrated that, in contrast to GaAs [186] holes bound to Mn in (Ga,Mn)N are located in the  $d$ -shell. The majority of Mn is present in the neutral  $Mn^{3+}$  state in (Ga,Mn)N with 0.2–0.6% of Mn grown by plasma-enhanced MBE. In samples codoped with Si, electrons are transferred to the Mn acceptors as shown in Fig. 37. The transition associated with  $Mn^{3+}$  and  $Mn^{2+}$  levels, also referred to as  $Mn^{3+/2+}$  or  $(3+/2+)$  acceptor level is located at 1.8 eV above the valence band with accuracy of about 0.2 eV. The deep level of Mn states would hinder the presence of free electrons or holes in (Ga,Mn)N. It was also observed the characteristic absorption spectrum with the zero-phonon-line (ZPL) at 1.42 eV, same as that reported by Korotkov *et al.* [183, 184].

Attempts have been made to determine the nature of Mn ions in GaN in terms of intra ion levels in the GaN environment. One such investigation is the X-ray absorption spectroscopy (XAS). In Mn  $L_{3,2}$  X-ray absorption,  $2p$  core electrons are excited to unfilled  $3d$  states, therefore, this technique is a direct probe of the magnetically active Mn  $2d$  band. Mn  $L_{3,2}$  X-ray absorption is also highly sensitive to the oxidation state of  $3d$  transition metal ions, and thus can yield valuable information when applied to transition-metal doped semiconductors. X-ray absorption (XAS) in (Ga,Mn)As and (Ga,Mn)N showed that the hybridization between Mn states and charge carriers is reduced in (Ga,Mn)N, which is consistent with the absence of ferromagnetism order across the sample [187]. Similar conclusion was drawn recently from electron spin resonance (ESR) studies of (Ga,Mn)N. The multiplet structures in XAS is characteristic of a mostly  $d^5$  ground state, indicating predominantly  $Mn^{2+}$  impurities [187].

Electron paramagnetic resonance (EPR) is a technique which can determine the energy levels associated with magnetic ions in the GaN environment. Wolos *et al.* [175] carried out EPR magnetization, and optical absorption studies in bulk GaN crystals doped with Mn and some samples co-doped with Mg acceptors.

They concluded that the charge state of the Mn ion in GaN depends on the Fermi level. In  $n$ -type samples, Mn is an ionized acceptor  $A^-$  center of  $Mn^{2+}(d^5)$ . In this case, the third electron needed for tetrahedral bonding is provided by a donor impurity and is bound tightly to the Mn ion. However, in the highly resistive samples, with lowered Fermi level (in samples co-doped with Mg), Mn is most probably in neutral configuration  $A^0$ , either in the form of a localized  $Mn^{3+}(d^4)$ , or a delocalized  $Mn^{2+}(d^5) + \text{hole center}$ . Optical absorption spectra of Mn-doped and Mn/Mg co-doped samples show the typical Mn-related absorption bands, which were interpreted as arising from photoionization of  $Mn^{2+}(d^5)$  to GaN conduction band in  $n$ -type samples and from photoionization of neutral Mn  $A^0$  to GaN valence band in highly resistive samples, respectively. The location of the Mn acceptor level  $A^- [Mn^{2+}(d^5)]$  was derived as  $1.8 \text{ eV} \pm 0.1 \text{ eV}$ . Given the fact that GaN has a low temperature bandgap of 3.5 eV, this result agrees with the previous discussion [173]. The observations were interpreted with the help of a coordination diagram [175] as shown in Fig. 38 describing the valence band to  $Mn^{2+}(d^5)$  level and  $Mn^{2+}(d^5)$  level to the conduction band. Relevant to the dilute magnetic semiconductor properties, the magnetization data reveal Brillouin-type magnetization with  $Mn^{2+}(d^5)$ , whereas the highly resistive samples show magnetic anisotropy characteristics. As mentioned in the previous paragraph, the  $d^5$  ground state of Mn was also observed by Edmonds *et al.* [187] via their Mn  $L_{3,2}$  X-ray absorption study. The change of Mn ion configuration may be used to explain the effect of Fermi level position on magnetic property reported by Reed *et al.* [176] although the Mn charge state was not investigated in their study. The change of Fermi level changes the configuration of Mn ions, which will directly affect the magnetic property observed for the material. It is desirable to study the nature of the neutral Mn in GaN, i.e., whether an extra hole is localized on the Mn  $d$  shell center for  $Mn^{3+}(d^4)$

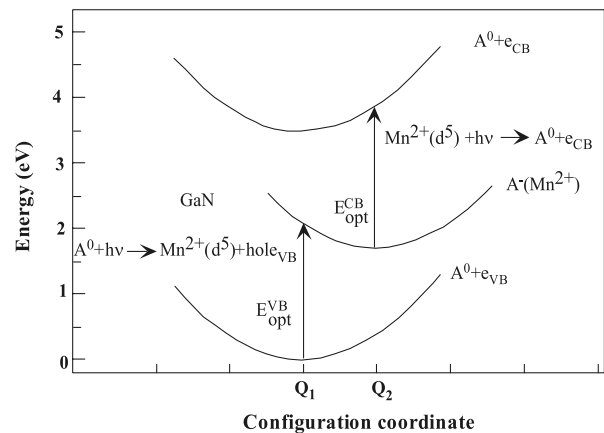


Figure 38 Configuration-coordinate diagram showing Mn-related optical transitions in GaN where parabolas represent the energy levels. The optical transitions occur without changing the configuration coordinate. For example at point  $Q_1$  the direct  $E_{opt}^{VB}$  optical transition represents  $A^0 + h\nu \rightarrow Mn^{2+}(d^5) + \text{hole}_{VB}$  and at point  $Q_2$  the direct  $E_{opt}^{CB}$  transition represents  $Mn^{2+}(d^5) + h\nu \rightarrow A^0 + e_{CB}$ . The thermal energies are determined by the minima in the configuration parabola which are indirect. The relaxation energy is then the difference between the optical transition energy and the thermal energy (after ref. [175]).

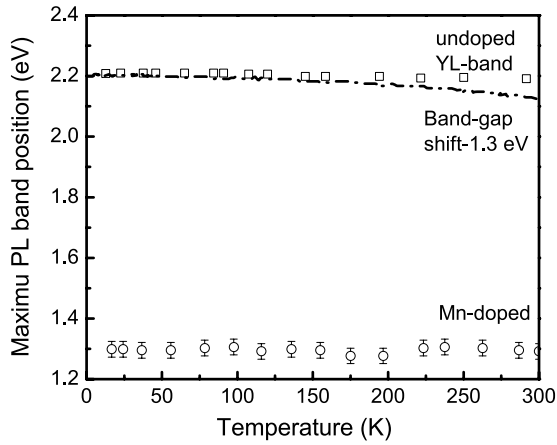


Figure 39 Temperature dependence of the 1.27 eV peak and YL band. For comparison the band edge variation with temperature is shown (after ref. 189).

or on a delocalized orbit for  $\text{Mn}^{2+}(d^5) + \text{hole}$  configuration, so that more direct relationship between the Mn state and magnetic property can be established.

Wolos *et al.* [188] also investigated the magneto-optical properties of intra-center absorption band related to neutral Mn acceptor in GaN bulk crystal. Magnetic field strengths of up to 22T were employed. The absorption band is built of a zero-phonon line at 1.4166 eV followed by GaN phonon spectrum. No splitting of the zero-phonon line was observed. The only characteristic feature recorded for high magnetic fields was a step-like behavior of the spectral position of zero-phonon line measured in Faraday configuration. The step appeared at a magnetic field of about 7 T, with a shift in energy of about 1.3 meV. The behavior of the band in magnetic field may be reasonably explained in terms of a model of  $\text{Mn}^{3+}(d^4)$  ion in trigonal crystal field, undergoing Jahn-Teller distortion and spin-orbit coupling, strongly supporting the localized character of Mn neutral acceptor in GaN.

Turning our attention to standard photoluminescence measurements, Korotkov *et al.* [189] observed PL transition as a broad and structureless band with a maximum at 1.27 eV and FWHM of about 0.26 eV, at  $T = 20$  K due to Mn acceptor. The temperature behavior of this transition differs from that of the bandgap, as shown in Fig. 39. Over the temperature range studied, the band gap shifted by 80 meV, whereas the 1.27 eV peak remained nearly temperature independent. This is typical of deep level defects with strong electron-phonon coupling [190], or an intra-atomic emission [191]. Transient PL study of this band by the same group revealed a very slow exponential decay of the PL intensity with a characteristic lifetime of about 8 ms [183]. The slow exponential decay of PL is typical of internal transitions. Most probably the 1.27 eV band is caused by transitions of holes from the excited states of  $\text{Mn}^{3+}$ , located close to the valence band, to its ground  $^5T$  level.

The Mn-related optical properties in GaN have also been studied as a function of Mn concentration [192] by elastic recoil detection. In this experiment, the Mn-doping level was varied between  $5 \times 10^{19}$  and  $2.3 \times 10^{20} \text{ cm}^{-3}$ . The optical absorption spectra recorded at 2 K of nominally undoped GaN, (Ga,Mn)N, and

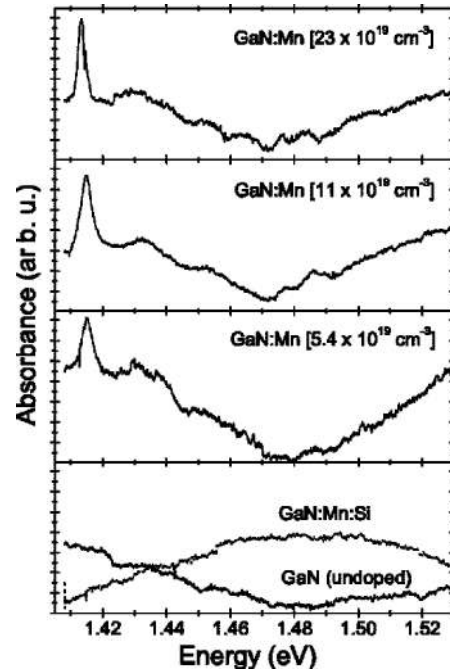


Figure 40 Optical absorption spectra at 2 K for MBE-grown undoped, Mn-doped, and Mn + Si co-doped GaN. The Mn concentration varied from  $5.4$  to  $23 \times 10^{19} \text{ cm}^{-3}$  (after ref. 192).

(Ga,Mn)N:Si are replotted in Fig. 40. The absorption peak at 1.414 eV can be attributed to an internal  $^5T_2 \rightarrow ^5E$  transition of the neutral  $\text{Mn}^{3+}$  state. The intensity of this peak was found to scale with the  $\text{Mn}^{3+}$  concentration in transmission spectroscopy measured at 2 K. In addition, the CL measurements showed that Mn-doping concentrations of around  $10^{20} \text{ cm}^{-3}$  reduced the near band edge emission intensity by about one order of magnitude. A complete quenching of the donor-acceptor-pair band at 3.27 eV and strong decrease of the yellow luminescence centered at 2.2 eV were attributed to a reduced concentration of  $V_{\text{Ga}}$ . In the infrared spectral range of 0.8–1.4 eV, three broad Mn-doping related CL emission bands centered at 1.01, 1.09, and 1.25 eV were observed, the origin of which may be from deep donor complexes generated as a result of the heavy Mn-doping.

The electronic states of (Ga,Mn)N co-doped with Mg acceptors have also been investigated utilizing both PL [193] and PLE [194] spectroscopies. It was found that by adding Mg acceptors in (Ga,Mn)N, the weak Mn-related PL band at 1.3 eV was quenched. The change in PL spectra indicates that the Mg addition stabilizes the  $\text{Mn}^{4+}$  charge state by decreasing the Fermi level. A series of sharp PL peaks were observed at 1 eV in co-doped epilayers and were attributed to the intra  $d$ -shell transition  $^4T_2(F) - ^4T_1(F)$  of  $\text{Mn}^{4+}$  ions and their phonon replicas are believed to be involved as well. The relative intensities of the sharp peaks were found to be strongly dependent on the excitation wavelength, indicating that the optically active  $\text{Mn}^{4+}$  centers involved in the separate peaks are different. The temperature dependence of the PL spectrum suggests the presence of at least three distinct  $\text{Mn}^{4+}$  complex centers. Based on the optical studies of Han *et al.* [194], the energy levels of  $\text{Mn}^{4+}$  ions in the GaN band diagram are depicted in Fig. 41.



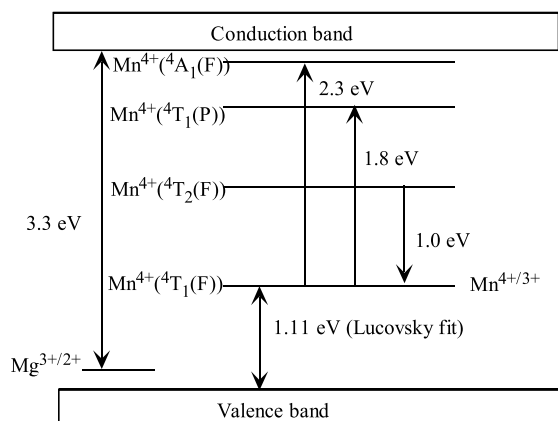
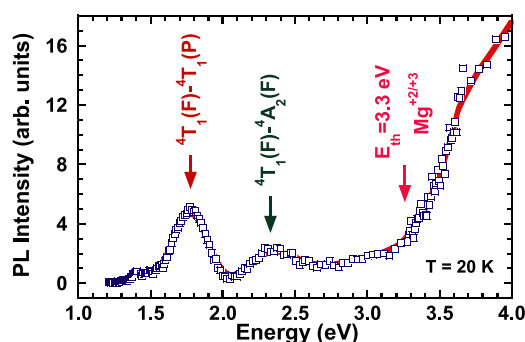


Figure 41 Energy levels of  $\text{Mn}^{4+}$  ions in wurtzite GaN. The energies are given for a crystal temperature of 20 K (after ref. 194).



*Figure 42* The 20 K PLE spectrum of (Ga,Mn)N co-doped with Mg after subtracting the Lucovsky fit (after ref. 194. Courtesy of B. Han).

The energy levels in Fig. 41 can be used to understand the PLE spectrum (shown in Fig. 42) of the  $\text{Mn}^{4+}[^4T_2(\text{F}) - ^4T_1(\text{F})]$  transition, which reveals intracenter excitation processes via the excited states of  $\text{Mn}^{4+/3+}$  ions. PLE peaks observed in Fig. 42 at 1.79 and 2.33 eV are attributed to the intra- $d$ -shell transitions from the ground  $^4T_1(\text{F})$  state to the  $^4T_1(\text{P})$  and  $^4A_2(\text{F})$  excited states, respectively. In addition to the intrashell excitation processes, a broad PLE band involving charge-transfer transition of the  $\text{Mn}^{4+/3+}$  (or  $4+/3+$ ) was observed. As determined from the onset of this PLE band, the position of the  $\text{Mn}^{4+/3+}$  deep level is 1.11 eV above the valence band maximum, which is consistent with *ab initio* calculations by Gertsman *et al.* [195] where the  $\text{Mn}^{4+/3+}$  transition level is calculated to be 1.1 eV above the VBM (see Fig. 43 for a summary of GaN transition metal transition levels). PLE results further indicate  $4+$  as the predominant oxidation state of Mn ions in  $p$ -type GaN : Mn when the Fermi energy is below 1.11 eV as measured from the top of the valence band maximum

The optical and electrical properties of GaN films implanted with Mn have been jointly studied [196] by means of optical transmission spectra, micro-cathodoluminescence spectra, capacitance-voltage and capacitance-frequency curves, temperature dependence of resistivity, and deep level transient spectroscopy (DLTS) with both electrical and optical injection. Optical transmission on *n*-type GaN samples implanted with high doses of Mn ( $\sim 3 \times 10^{16} \text{ cm}^{-2}$ )

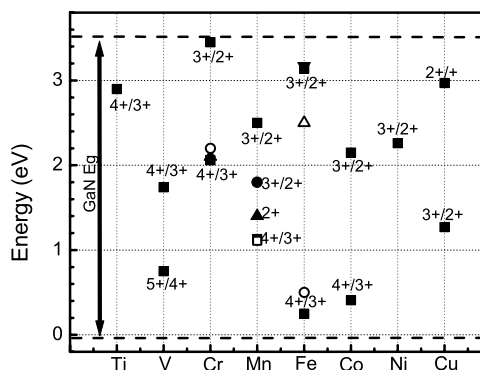


Figure 43 Charge transfer levels of transition metal impurities in GaN. Data in this figure include the results from Gerstman *et al.* [195] (■), Mahadevan and Zunger [97, 98] (▲), Heitz *et al.* [198] (▼), Graf *et al.* [173] (●), Baur *et al.* [199] (△), Van Schilfgarde and Myrasov [89] (○), and Han *et al.* [194] (□).

shows that Mn forms a deep acceptor near  $E_v + 1.8$  eV. The Mn complexes formed with native defects are deep electron traps with a level near  $E_c - 0.5$  eV, which are most likely responsible for a strong blue luminescence band with energy near 2.9 eV.

It is worth noting that, apart from Mn forming deep acceptor levels in (Ga,Mn)N as reported in the literature, an optical study by Yoon *et al.* [197] pointed out the presence of a Mn acceptor level at about  $E = 3.08$  eV for a low Mn content (Ga,Mn)N. This suggests that the Mn-bound holes in III-nitride exhibit the shallow impurity states. Arrhenius plots of the intensity of the Mn acceptor give an activation energy of  $E = 310$  meV, indicating that the observed thermal quenching of the Mn-related PL peak is due to the dissociation of an acceptor-bound hole. The observation by Yoon *et al.* [197] is consistent with predictions based on effective mass theory of the shallow hydrogenic impurity state model.

Before closing the discussion of (Ga,Mn)N, in Fig. 43 we summarize the charge transfer levels of transition metal impurities in GaN as reported in the literature. These are of fundamental interest in interpreting and predicting the magnetic properties of GaN-based DMSs. They are also naturally critical in interpreting the optical transitions in TM doped GaN. It is believed that combination of optical, magneto-optical, EPR, ESR, electrical and magnetic measurements, not necessarily in that order, may be required for a full characterization of the state of these impurities in GaN, also applicable to ZnO, and their participation in any magnetization.

#### 5.4. Magnetic, structural, optical, and electrical properties of Cr-doped GaN

Before delving into Cr doped GaN, it is instructive to revisit the section on the theoretical simulations. Cr-doped GaN was found to have the most stable ferromagnetic state in transition metal-doped GaN by Sato *et al.* [88] and Das *et al.* [5] performed a first principles calculation within the framework of linearized muffin-tin orbital tight binding method and gradient-corrected density-functional theory. They predicted the

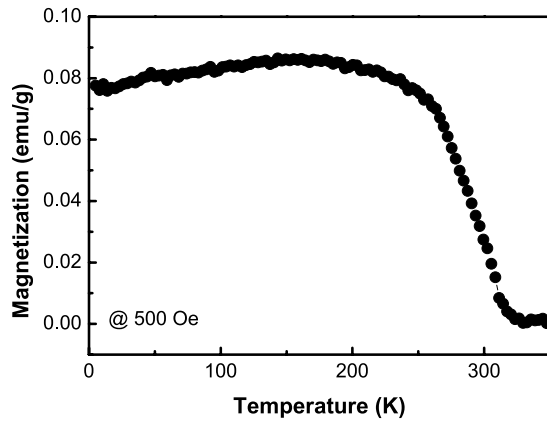


Figure 44 Temperature-dependent magnetization of Cr-doped GaN single crystal in an applied magnetic field of 500 Oe (after ref. 19. Courtesy of S.-Y. Jeong).

coupling between Cr atoms to be ferromagnetic with a magnetic moment of  $2.69 \mu_B$  for the case of bulk GaN, and  $4 \mu_B$  for the case of GaN clusters. Prior to the above mentioned theoretical work, Cr-doped GaN single crystals [19] and thin films [20] had been grown and studied for their magnetic properties. Single crystal (Ga,Cr)N samples fabricated by adding Cr to GaN single crystal by flux method showed ferromagnetic  $T_C$  at 280 K, whereas the thin films grown by ECR MBE were reported to display ferromagnetic behavior with a Curie temperature higher than 400 K. The temperature dependence of magnetization for a (Ga,Cr)N single crystalline sample is plotted in Fig. 44. The ferro- to paramagnetic transition at  $\sim 280$  K was also observed in the temperature-dependent resistance measurement in a zero-magnetic field. The M-H hysteresis loops yield coercive fields of 54 and 92 Oe at 250 K and 5 K, respectively. The carrier density in this crystal is about  $9 \times 10^{18} \text{ cm}^{-3}$  (*n*-type), and the mobility is about  $150 \text{ cm}^2/\text{Vs}$ . On the other hand, (Ga,Cr)N thin films grown by MBE were deemed very encouraging, because they showed ferromagnetism with  $T_C$  above 400 K, and remarkable M-H hysteresis loops with a saturation field of about 2000 Oe and a coercive field of about 55 Oe at 300 K as shown in Fig. 45. Again, caution must be exercised here as to the characterization of the observed magnetism.

Hashimoto *et al.* [200] studied the structural and optical properties of (Ga,Cr)N layers grown by ECR-MBE, which purportedly exhibited ferromagnetic behavior at room temperature. From XRD and EXAFS measurements, those authors could not detect any second-phase material. Some common compounds of Cr with Ga or N include  $\text{CrGa}_4$ , CrN,  $\text{Cr}_2\text{N}$ . Among them,  $\text{CrGa}_4$  and CrN have been shown to be non-ferromagnetic [201–203], and the magnetic properties of  $\text{Cr}_2\text{N}$  are not yet known. From the optical emission point of view, strong PL emission at 3.29 eV (10 K) was observed in  $\text{Ga}_{0.985}\text{Cr}_{0.015}\text{N}$  film as shown in Fig. 46. This PL emission was attributed a band-to-band transitions in (Ga,Cr)N. The assignment was done from temperature- and excitation-power-density dependent PL measurements. It was also found that the PL emission peak energy in (Ga,Cr)N decreases with increasing temper-

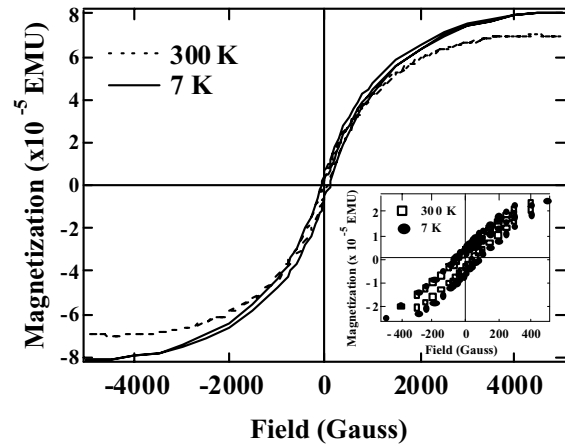


Figure 45 M-H hysteresis loops at 7 and 300 K for (Ga, Cr)N thin film on sapphire grown by MBE. Inset shows the expanded curves. (Reprinted with permission from ref. 20. Copyright 2002 Elsevier.)

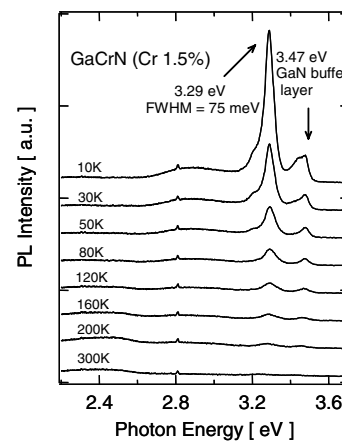


Figure 46 Temperature dependence of PL spectrum for the (Ga,Cr)N layer with the Cr concentration of 1.5% in the range of 10 to 300 K (after ref. 200. Courtesy of H. Asahi).

ature in accordance with the Varshni formula similar to the GaN excitonic transition peak. If truly confirmed Cr-doped GaN may provide new hope for spintronic applications at room temperature and above. However, as for other transition metal doped GaN further research is needed to be certain of the observed results as being due to carrier mediated ferromagnetism. At the very least the basis for the observations need to be determined.

Takeuchi *et al.* [204] studied the electronic structure of (Ga,Cr)N grown on ZnO substrates by MBE. The XAS spectra of N 1s spectra for  $\text{Ga}_{1-x}\text{Cr}_x\text{N}$  ( $x = 0.06$ ) show similar features with wurtzite GaN, but with additional peak indicating the hybridization of N 2p states with Cr 3d states. For higher Cr concentration ( $x = 0.29$ ), the CrN impurity phase exists in the film. Singh *et al.* [205] studied the effect of substitutional incorporation of Cr on the magnetic properties of (Ga,Cr)N. (Ga,Cr)N films with identical Cr concentration (3%) were grown at different temperatures by MBE. The fraction of Cr at the substitutional site ( $\text{Cr}_{\text{Ga}}$ ) was determined from the RBS channeling angular distribution of Cr and Ga in the  $\langle 0001 \rangle$  axial direction, as shown in Fig. 47. The results indicate that 78–90% of Cr did indeed occupy the substitutional sites for GaN grown in the temperature range of 700–775 °C, and

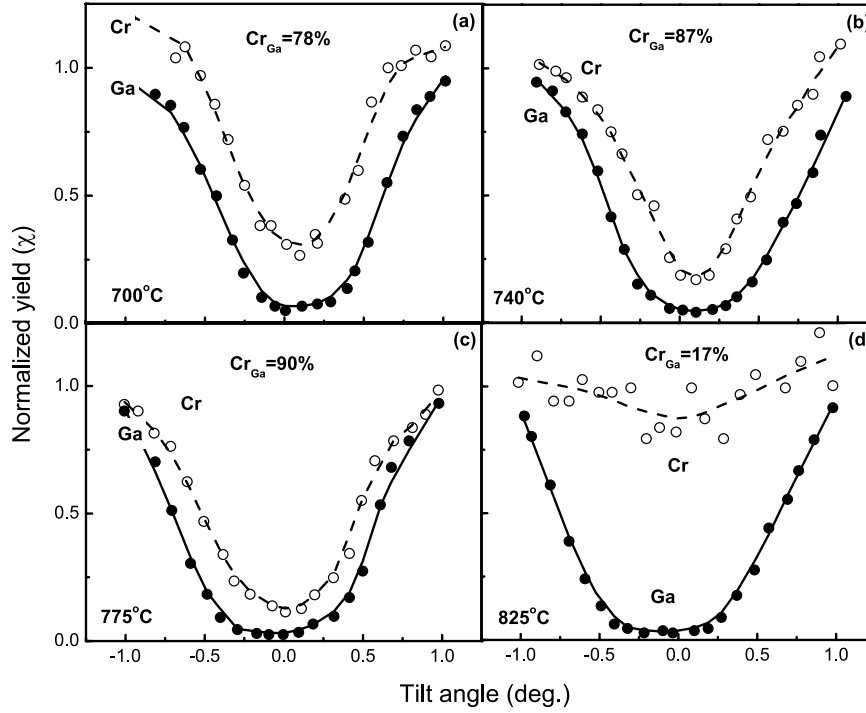


Figure 47 Channeling angular scans in (0001) axial direction for (Ga,Cr)N films grown at (a) 700, (b) 740, (c) 775, and (d) 825 °C (after ref. 205).

HRTEM showed that Cr distributed uniformly in the lattice. However, only a small fraction of Cr (<20%) was found to be located at the substitutional sites for films grown at 825°C, and a significant Cr clustering is revealed from energy-filtered TEM. A higher magnetic moment ( $0.35 \mu_B/\text{Cr}$  vs.  $0.13 \mu_B/\text{Cr}$ ) and higher percentage of magnetically active Cr ions ( $\sim 12$  vs. 4%) were found in the films with high substitutional concentration as compared to those with lower substitutional concentration. These results serve to establish that the location of Cr in the (Ga,Cr)N lattice plays a crucial role in determining its magnetic properties.

Related to Cr-doped GaN, Cr-doped AlN has also been observed to exhibit high temperature ferromagnetism. Liu *et al.* [18] have reported  $T_C$  over 900 K in both (Ga,Cr)N and (Al, Cr)N films prepared by reactive MBE on 6H-SiC substrates. Cr-doped GaN was found to have the highest saturation magnetic moment ( $M_s$ ) at a Cr content of 3%, which corresponds to  $\sim 70\%$  of Cr impurities on the substitutional sites for (Ga,Cr)N by channeling Rutherford backscattering. Cr-doped AlN displayed the same trend but with the highest  $M_s$  for a Cr content of 7%. Liu *et al.* [18] suggested that substitutional Cr defects were involved in the observed magnetic behavior. In the same study, electrical transport and magnetotransport properties of Cr-doped GaN have also been measured, as shown in Fig. 48. The thermally activated process follows  $R = R_o \exp[(T_o/T)^{1/2}]$ , which is characteristic of variable range hopping between localized states with a Coulomb gap [206] which in this case is the variable range hopping in the Cr impurity bands. As far as the deep level traps, Cr is known experimentally [207], and predicted theoretically [208], to form a deep level at an energy of  $\sim 2.0$  eV above the GaN valence band. The negative magnetoresistance (MR) seen in Fig. 48(b) in the range of 2 and 300 K can be attributed to a mech-

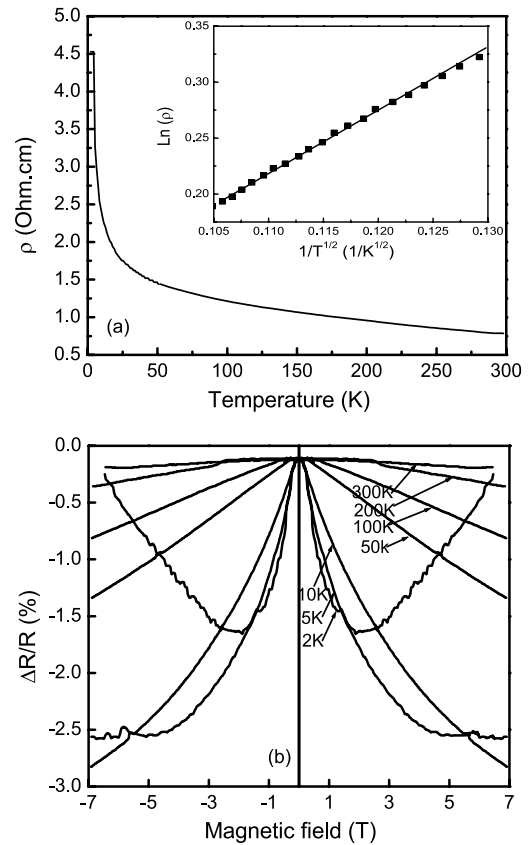


Figure 48 Temperature dependent transport measurements of (Ga, Cr)N deposited on sapphire (a) Resistivity ( $\rho$ ). Inset shows comparison between experimental data and functional relationship expected for variable range hopping. (b) Magnetoresistance ( $\Delta R/R$ ), the relative exchange of sheet resistance in a magnetic field (after ref. 18. Courtesy of H. X. Liu).

anism, originally proposed by Sivan, Entin-Wohlman, and Imry [209] for nonmagnetic semiconductors, that takes into account the influence of the magnetic field on the quantum interference between the many paths

linking two hopping sites [210]. In the variable-range hopping regime and at small magnetic fields, the MR is consistent with the temperature dependence results. The above experimental results strongly suggest that ferromagnetism in (Ga, Cr)N and (Al, Cr)N can be attributed to the double exchange mechanism as a result of hopping between near-midgap substitutional Cr impurity bands.

### 5.5. Other TM and rare earth doped GaN : (Co, Fe, Gd, V, etc.)

In Co-implanted *n*-type GaN [196] it was found from optical transmission that Co, similar to Mn, also form a deep acceptor at about  $E_v + 1.9$  eV. The Co complexes formed with native defects act as deep electron traps with a level near  $E_c - 0.5$  eV, which are most likely responsible for a strong blue luminescence band with energy near 2.9 eV. The other deep level electron traps at  $E_c - 0.25$  eV and  $E_c - 0.7$  eV are probably associated with a defective region adjacent to the implant region, due to out-diffusion during the post-implant annealing treatment.

Utilizing another magnetic metal, Shon *et al.* [24] reported implantation of  $\text{Fe}^+$  ions into *p*-type GaN, which gives rise to ferromagnetism based on their observations of apparent ferromagnetic hysteresis loops in individual measurements performed at 10 and 300 K. Ferromagnetism was confirmed by temperature-dependent magnetization measurements which yield persistent ferromagnetism above 350 K. Optical transitions were observed in PL measurements at 2.5 eV and around 3.1 eV, which were linked to the presence of Fe. Further, the luminescence peak at 2.5 eV has been identified as a “donor-Fe acceptor” transition, while the 3.1 eV peak as a “conduction band-Fe acceptor” transition. Vanadium, on the other hand, when implanted into *p*-type GaN films at doses of  $3 \times 10^{16}$  and  $5 \times 10^{16} \text{ cm}^{-2}$ , has been found experimentally [23] to be paramagnetic up to 300 K, contradicting the theoretical prediction [88] that V-doped GaN has ferromagnetic states even without any additional carrier doping treatment.

Doping with rare-earth metal, such as Gd in GaN, has been reported to lead to ferromagnetism above room temperature. Teraguchi *et al.* [211] prepared  $\text{Ga}_{0.94}\text{Gd}_{0.06}\text{N}$  ternary alloy on 6H-SiC substrates by RF-MBE. Those authors observed hysteresis in M-H curves at all measurement temperatures ranging from 7 to 400 K, with coercivity  $H_c \sim 70$  Oe at 300 K. Accordingly, an emission peak around 645 nm was observed in the CL spectra believed to originate from  $\text{Gd}^{3+}$ , in analogy to Eu-doped GaN [212]. In the GaN environment, there are several phases which could be formed with participation by Gd. Of particular importance to the present topic, Gd element and the rocksalt structure of GdN can form ferromagnetic materials with Curie temperatures of 307.7 K (or some reported as 289 K [25]) and 72 K [213], respectively. The Curie temperature for both materials is lower than that of  $\text{Ga}_{0.94}\text{Gd}_{0.06}\text{N}$  observed in this measurement ( $>400$  K). Therefore, the higher Curie temperature of  $\text{Ga}_{0.94}\text{Gd}_{0.06}\text{N}$  was attributed to neither the Gd element nor the rocksalt struc-

ture of GdN, rather, it was plausibly associated with the formation of (Ga,Gd)N ternary alloy.

Later on, an investigation on a series of Gd-doped GaN samples with Gd concentration ranging from  $7 \times 10^{15}$  to  $2 \times 10^{19} \text{ cm}^{-3}$  demonstrated consistent results. Dhar *et al.* [25] reported above-room-temperature ferromagnetism for all (Ga,Gd)N samples even with Gd concentration less than  $10^{16} \text{ cm}^{-3}$ , for both MBE grown (Ga,Gd)N and ion-implanted (Ga,Gd)N films. From the M-H curves as well as the M-T curves measured under both FC and ZFC conditions, displayed in Fig. 49, the inferred Curie temperature is above 360 K. Further, the Curie temperature continually increased with increasing Gd concentration to well above room temperature.

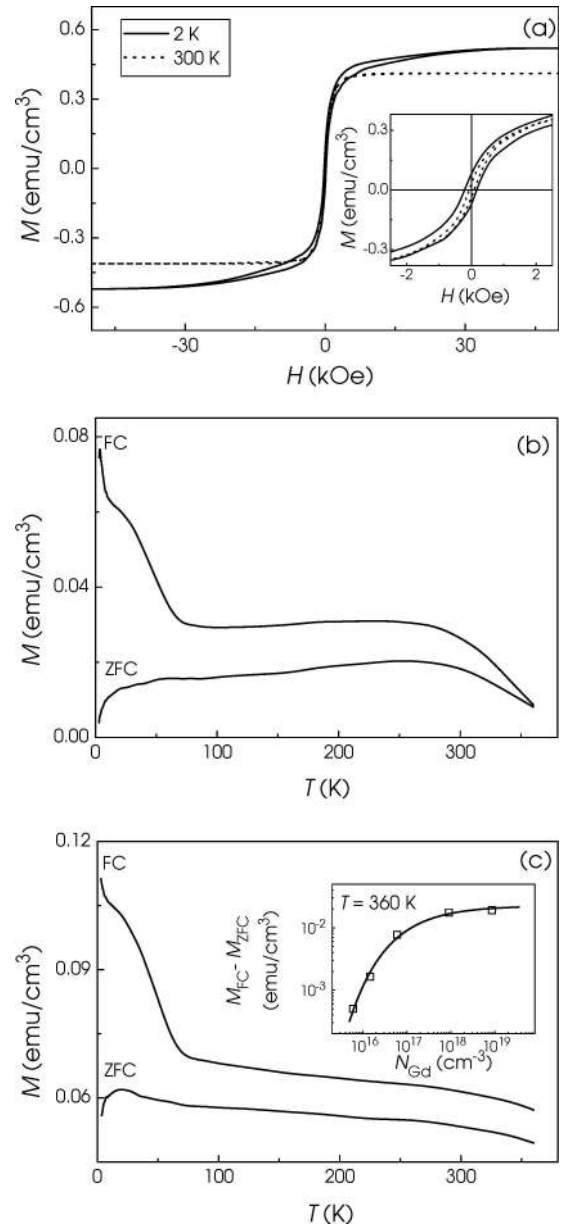


Figure 49 (a) M-H curves showing hysteresis loops at 2 K (solid line) and 300 K (dotted line), for sample with Gd concentration  $\sim 6 \times 10^{16} \text{ cm}^{-3}$ . The inset of (a) is a zoom of small fields. M-T curves at FC and ZFC conditions at  $H = 100$  Oe are plotted for (b) sample with Gd concentration  $7 \times 10^{15} \text{ cm}^{-3}$  and (c) sample with Gd concentration  $\sim 6 \times 10^{16} \text{ cm}^{-3}$ . The difference between FC and ZFC magnetization measured at 360 K is plotted as a function of  $N_{\text{Gd}}$  in the inset of (c). The solid curve through the data is a guide to the eye (after ref. 25. Courtesy of S. Dhar).

Due to the large Gd-Gd distance in GaN, the microscopic origin of the magnetic coupling leading to ferromagnetism could not be explained simply in terms of the direct exchange, double exchange, or superexchange interactions amongst the Gd atoms. Nor could it be accounted for by the free-carrier mediated RKKY type long-range coupling, given the electrically highly resistive nature of the alloy after doping with Gd. Dhar *et al.* [25] believe that the high  $T_C$  ferromagnetism is closely related to their observation of colossal magnetic moments of Gd in GaN, which may be explained by the long-range spin polarization of the GaN matrix induced by Gd atoms. The  $T_C$  dependence on Gd concentration can be also qualitatively explained within the framework of percolation theory [214]. These findings are very promising, since (Ga,Gd)N may be easily doped with donors (acceptors) with a concentration exceeding that of Gd, to generate spin-polarized electrons (holes) in the conduction band (valence band). Gd-doped GaN with its  $T_C$  above room temperature might thus be a very attractive candidate for future semiconductor-based spintronics.

## 6. Applications and devices

The realization of high  $T_C$  ferromagnetic DMS might promote the development of spintronic devices, the premise of which is exploitation of electron spin, in addition to its charge, for creating a new class of devices with unprecedented functionality. Devices utilizing spin transport rather than charge transport have the advantages of faster data processing and operation at much less power consumption [215]. In order to realize spintronic devices of practical applications, spin-polarized carriers need to be first efficiently injected into semiconductors. Spin injection across a semiconductor-ferromagnetic material interfaces can be adversely affected by the presence of defects at the interface, which results in low injection efficiency [216]. Diluted magnetic semiconductors with ferromagnetism above room temperature could pave the way for achieving spin polarization and high efficiency spin injection necessary for realization of spintronic technologies.

The prospects are very exhilarating for device applications utilizing ferromagnetic properties of TM-doped GaN and ZnO. As discussed earlier in the theoretical studies of TM-doped GaN, Kronik *et al.* [94] found that the introduction of Mn, in its ordered ferromagnetic phase, results in the formation of a 100% spin polarized  $\sim 1.5$  eV-wide impurity band, primarily due to hybridization of Mn  $3d$  and N  $2p$  orbitals, which renders the material half metallic and supports effective-mass transport. This unique feature, in conjunction with possibly above-room temperature  $T_C$  and the inherent compatibility with GaN technology, makes (Ga,Mn)N a potentially significant material for spin-injection applications for modern spintronic devices. ZnO is also promising in achieving high spin polarized injection efficiencies and carriers due to the fact that  $3d$ -transition metals have high solubility (up to  $\sim 30\%$  for Mn and Co). The addition of ferromagnetism to the already

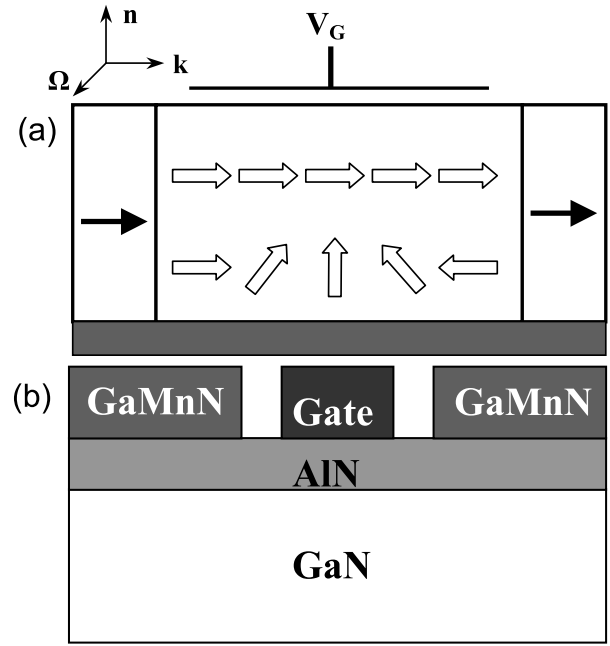


**Figure 50** (a) Scheme of spin field-effect transistor (SFET). The source (spin injector) and the drain (spin detector) are ferromagnetic metals or semiconductors, with parallel magnetic moments. The injected spin-polarized electrons with wave vector  $\mathbf{k}$  move ballistically along a quasi-one-dimensional channel in a plane normal to  $\mathbf{n}$ . Electron spins precess about the precession vector  $\Omega$ , which arises from spin-orbit coupling and which is defined by the structure and the materials properties of the channel. The magnitude of  $\Omega$  is tunable by the gate voltage  $V_G$  at the top of the channel. The current is large if the electron spin at the drain points in the initial direction (top row)—for example, if the precession period is much larger than the time of flight—and small if the direction is reversed (bottom) (after ref. 44). (b) Schematic diagram of a proposed spin FET based on the GaN semiconductor system. InGa<sub>0.5</sub>N can be substituted for GaN if the Rashba coupling is too small in GaN.

unique optical and electric properties of GaN and ZnO could result in many novel multifunctional spintronic devices.

Spin light emitting diode (LED) and spin tunneling junctions based on the current achievements in research of DMSs have already been reported. Fig. 50(a) shows a schematic diagram of the spin FET based on the idea first proposed by Datta and Das [44, 217]. In this device, carriers are injected into the channel from a spin-polarizing electrode (called *polarizer* or source), which can be either a ferromagnetic metal or a dilute magnetic semiconductor, through a channel to be collected by another magnetically polarized electrode (called *analyzer* or drain). The current through the transistor depends on the relative orientation of the electron spins and the source and drain magnetic moments, the current being maximum when they all align. In a spin FET, application of a relatively low gate voltage causes an interaction between the electric field and the spin precession of the carriers [218, 219] via the so-called Rashba spin-orbit coupling effect [218]. It is equivalent to the action of an effective magnetic field  $B_{\text{eff}}$  which lies within the plane of the 2D electron gas perpendicularly to the instantaneous wave-vector. This results in spatial modulation of the net spin polarization of the current, which can be controlled by an applied gate voltage. If this is sufficient to render the spin orientation of the carriers out of alignment in relation to

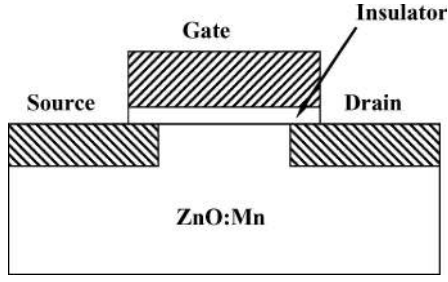


Figure 51 A schematic of a spin-FET based on transition metal-doped ZnO. Co-doped ZnO can be used as the source and drain contacts (after ref. 221).

that of the drain contact (analyzer), then the current is effectively shut off and this can occur at much lower bias than needed to shut off the current in a charge-controlled FET. Fig. 50(b) represents the schematic of a proposed spin FET based on the GaN material system. Challenges to fabricate a spin FET in the GaN-based system include efficient spin polarized injection, transport, control and manipulation, and detection of spin polarization as well as spin-polarized current. Devices are required to generate coherent spin injection, with dimensions comparable if not less than the spin coherence length. This in the case of GaN means that the channel length must be shorter than some 200 nm. Mn-doped GaN nanotube arrays [220] which have been favorably predicted to enhance spin polarization or to increase the dephasing length should be developed.

Sato and Katayama-Yoshida [221] proposed a ZnO-based spin-FET, as shown in Fig. 51. The authors did first principles calculations for the ground state of transition metal-doped ZnO, and concluded that (Zn, Mn)O is of antiferromagnetic ground state, and ferromagnetism can be induced by hole doping. In this proposed structure, holes can be injected into Mn-doped ZnO by applying a negative bias gate voltage, and the system changes to a half-metallic ferromagnet. When ferromagnetic (Zn, Co)O is used for source and drain contacts, spin polarized electrons can flow in half-metallic (Zn, Mn)O. The same authors also proposed a structure to realize optically controlled ferromagnetism based on transition metal-doped ZnO grown on GaAs substrates [221]. With appropriate composition, paramagnetic ZnO : Mn<sub>1-x</sub>Cr<sub>x</sub> or ZnO : Mn<sub>1-x</sub>Fe<sub>x</sub> can be rendered ferromagnetic by hole doping or electron doping, respectively. The electrons and holes can be generated by photo-excitation at the interface between ZnO : Mn<sub>1-x</sub>Cr<sub>x</sub> (or ZnO : Mn<sub>1-x</sub>Fe<sub>x</sub>) and the GaAs substrate, then injected into ZnO : Mn<sub>1-x</sub>Cr<sub>x</sub> (or ZnO : Mn<sub>1-x</sub>Fe<sub>x</sub>) by using positive or negative bias voltage. The realization of these devices will critically depend on the stability of carrier-mediated ferromagnetism. Provided that the carrier-mediated ferromagnetism in GaN and ZnO is realized unambiguously, it will offer a variety of new control over not only the semiconducting properties but also over magnetism leading to new possibilities for magneto-electronics devices. Electric-field control of ferromagnetism has been demonstrated in a (In,Mn)As-based FET at reduced temperatures [222], and optically-controlled ferromagnetism has been reported in GaAs with Fe particles.

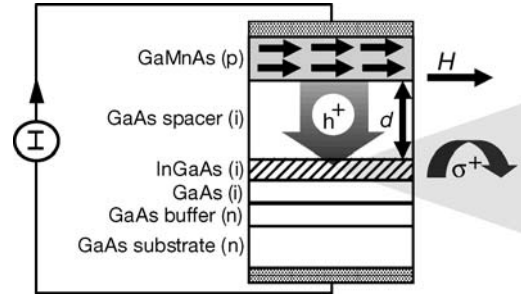


Figure 52 Injection of spin-polarized holes into a light-emitting *p-n* diode using a ferromagnetic semiconductor (Ga,Mn)As. (a) Sample structure. Spin-polarized holes  $h^+$  travel through the nonmagnetic GaAs and recombine with spin-unpolarized electrons in the (In,Ga)As quantum well.  $I$  represents the current, and  $\sigma^+$  represents circularly polarized light emitted from the edge of the quantum well. (Reprinted with permission from ref. 224. Copyright 1999 Nature Publishing group).

Spin light emitting diode (spin LED) allows modulating the polarization of the light emitted by the spin LED by application of an external magnetic field, which is of interest to optical switching and optical communication with increased bandwidth. Spin polarized light emission has been demonstrated in II–VI semiconductors [223] and III–V GaAs [224]. In order to give the reader a synopsis of the operation of spin LED, the GaAs device is discussed here, particularly since the GaN varieties are not yet available and there are some fundamental issues whether one circular polarization over the other is promoted. The sample structure of a GaAs-based spin LED is depicted in Fig. 52. The structure contains a *p*-type ferromagnetic semiconductor (Ga, Mn)As and *n*-type nonmagnetic semiconductor GaAs, which were epitaxially grown by MBE. The use of ferromagnetic (Ga, Mn)As allows one to inject spins in the absence of magnetic field. Spontaneous magnetization develops below the Curie temperature in the ferromagnetic *p*-type (Ga, Mn)As semiconductor, indicated by the arrows in the (Ga, Mn)As layer. Under forward bias, spin polarized holes are injected from the (Ga, Mn)As side into the nonmagnetic region and recombine with spin unpolarized electrons injected from the *n*-type GaAs substrate in a nonmagnetic quantum well made of (In, Ga)As (hatched region), as shown in Fig. 52, through a spacer layer with thickness  $d$  producing polarized electroluminescence (EL). Due to the crystal symmetry of GaAs, injected spin-polarized electrons have been detected in the form of circularly polarized light emission from the quantum well, which corresponds to the magneto-optical Kerr effect loops and can be directly related to spin-polarization. The presence of spin polarization has been confirmed by the observation of hysteresis in the polarization of the emitted light as a function of the magnetic field. The Curie temperature of (Ga, Mn)As is 52 K.

Intuitively, GaN has a smaller lattice constant than conventional III–Vs such as GaAs, thus the magnetic coupling strength is expected to be higher. However, optical experiments performed on GaN/InGaAs quantum wells [225] show that the electron spin relaxation time in these structures is shorter than in bulk GaN as well as in GaAs/InGaAs quantum wells. The approach requiring the least semiconductor technology



for achieving spin LED in GaN would be to implant Mn into the top contact  $p$ -GaN layer of the standard GaN/InGaN LED. Polyakov *et al.* [226] reported such spin LED. Although, the device produced EL of low intensity, its series resistance and the turn-on voltage are much higher than those of ordinary LED due to the difficulty in annealing out all radiation damage. The same group of authors studied the inverted spin LED structure grown by MBE with  $n$ -type GaMnN on the top also [227]. However, this approach was found not to be successful due possibly to the higher series resistance caused by the lower lateral conductivity of  $p$ -GaN inherent to these inverted structures. In addition, obtaining high quality layers on top of a very heavily doped  $p$ -GaN is not trivial. The parasitic diode formed with the lower  $p$ -GaN layer has been reported to be detrimental to device performance [228]. Furthermore, ferromagnetism in GaMnN is found to be unstable against the type of high temperature anneals used to minimize contact resistance.

Similar spin LED structures [229] have also been reported albeit without spin polarized light emission, wherein the device was grown by a hybrid of OMVPE and MBE techniques. It contains four main regions, namely, (1) a *spin injector* of a 120 nm-thick  $n$ -Ga<sub>0.97</sub>Mn<sub>0.03</sub>N layer, (2) a *spin detector* made up of 5 periods of nonmagnetic In<sub>0.4</sub>Ga<sub>0.6</sub>N quantum wells (3 nm) separated by Si-doped GaN barriers (10 nm each), (3) a nonmagnetic Si-doped GaN spacer (20 nm) (inserted between the aforementioned two regions to avoid direct overlap of electron and hole wave functions from the two regions and thus to ensure a predominant role of the spin injection as the source of spin polarization as monitored in the InGaN MQW spin detector), (4) a 2- $\mu$ m-thick layer of Mg-doped  $p$ -type GaN for electrical injection of holes into the spin detector. The structure was grown on sapphire substrates starting with a 2- $\mu$ m thick undoped semi-insulating GaN and also has a top layer of  $n$ -type Si-doped GaN (100 nm). The structure shows none or very low optical (spin) polarization at zero field or 5 T, respectively. The weak polarization observed is attributed to the intrinsic optical polarization of the InGaN MQW associated with population distribution between spin sublevels at low temperatures. The device shows loss of efficiency of spin polarization generated by optical spin orientation or electrical spin injection. The I-V characteristics also suffer from a parasitic junction between the (Ga, Mn)N and the  $n$ -GaN in the top contact layer due to low conductivity of the  $p$ -type layer. Transient and circularly polarized PL analyses of the spin injection dynamics [230] of a GaMnN/InGaN MQW LED structure suggest that the spin loss is most likely due to fast spin relaxation within the InGaN MQW which destroys any spin polarization generated by either optical or electrical spin injection. In the wurtzite III-nitride system, biaxial strain at the interfaces of heterostructures gives rise to large piezoelectric fields directed along the growth axis which ultimately breaks the reflection symmetry of confining potential, leading to the presence of large Rashba term in the conduction band Hamiltonian. It is this effect that is assumed to adversely contribute to the

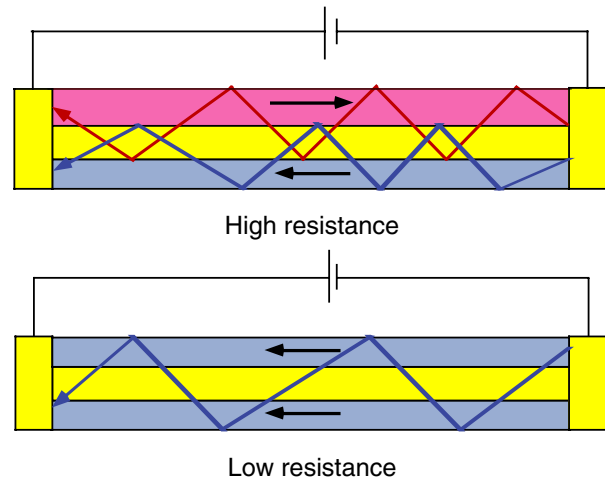


Figure 53 Schematic representations of transport that is parallel to the plane of a layered magnetic metal sandwich structure for aligned (low resistance) and antialigned (high resistance) orientations (Reprinted with permission from ref. 47. Copyright 1998 AAAS).

short spin relaxation times. The adoption of additional stressor layers or even cubic phase of nitrides has been suggested as a cure for larger spin splitting.

In addition to spin-FET and spin LED, spintronics-based ultra sensitive magnetic sensors could also have great impact in magnetic recording and the development of nonvolatile memory, and greatly increase the magnetic recording density of hard disk drives. The simple concept is illustrated in Fig. 53 as a “spin valve” [47]. When the magnetic moments of two ferromagnetic layers are antialigned, spin polarized electrons experience high resistance due to the high interfacial scattering and channeling of the current into narrow pathways. When the films become aligned, the device resistance decreases. If the magnetic moment of one of the ferromagnetic layers is very difficult to reverse in an applied magnetic field, whereas the moment of the other layer is very easy to reverse (“soft layer”), the soft layer then acts as the valve control and is sensitive to manipulation by an external field. The significant change in resistance in response to relatively small magnetic field in layered magnetic thin-film structures is called giant magnetoresistance effect (GMR), and is realized by using metallic layers or tunnel junctions in practical applications. Large tunnel magnetoresistance (TMR) has been observed in (Ga,Mn)As-AlAs-(Ga,Mn)As tri-layer structures (Fig. 54) [231]. In the stepped part where the magnetization is antiparallel, the tunneling resistance increases. When the AlAs film that constitutes the tunneling barrier was made thin (1.6 nm), a TMR ratio over 70% was obtained. A spin-valve transistor with an epitaxial ferromagnetic Fe/Au/Fe (001) base has been integrated on  $n$ -GaAs [232].

The spin coherence length (or dephasing length) is a critical parameter for such a device to function correctly. The initially spin-polarized electrons are subject to depolarization with distance, and the depolarization strongly depends on the material characteristics such as spin-orbit interaction. In this sense, the use of III-nitride may be beneficial in terms of longer spin



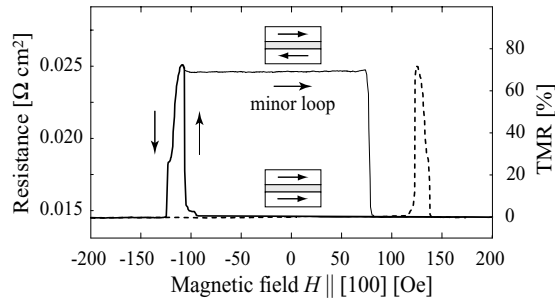


Figure 54 Tunnel magnetoresistance effect in a (Ga, Mn)As-AlAs-(Ga, Mn)As tri-layer structure, measured at a temperature of 8 K. The solid and dotted arrows indicate positive and negative magnetic field sweeping directions, respectively. The (Ga, Mn)As layers are 50 nm thick, and the Mn composition in these layers are 0.04 and 0.033. The AlAs layer is 1.6 nm thick. Since the easy axis of magnetization lies within the plane of the sample, a magnetic field is applied parallel to the sample surface. When a magnetic field is applied along the [100] direction, a tunneling magnetoresistance effect of over 70% is observed, and when a magnetic field is applied along the [110] direction, this effect is approximately 30% (after ref. 231. Courtesy of M. Tanaka).

coherence time, owing to their weak spin-orbit interaction compared to other III–V materials. Besides, due to the pronounced piezoelectric and pyroelectric effect in GaN based materials, the spin splitting of electrons and holes at GaN/Al<sub>x</sub>Ga<sub>1-x</sub>N heterojunctions may be optimized. It is worth to mention that although the Rashba coupling strength in GaN or InGaN is not really known, approaches have been proposed for measuring the zero-field spin splitting in the 2-DEG structure in III-nitride using the beating patterns in Shubnikov-deHaas oscillations [233], considering the spin splitting as the combined effects of Rashba, and Dresselhaus [234] interactions. A spin valve structure can be used to measure the coherence length.

Other potential spintronic applications include integration of magneto-optical effect in semiconductor optical isolators by using the Faraday effect to control the spin relaxation time and coherence for optical switches and quantum information processing. It has been shown that electron spin coherence is maintained for periods of at least a few nanoseconds in GaN [235], which raises the possibility of applications of confined electronic states to spin memory and manipulation.

## 7. Conclusions

The potential of room temperature ferromagnetism has rejuvenated the field of dilute magnetic semiconductors. While the devices are the eventual driving force, the importance of understanding and producing ferromagnetic diluted semiconductor materials with above room temperature Curie temperature, not to mention the junction temperature which is typically well above room temperature, cannot be overstated. The efforts on this topic could also potentially provide an opportunity for mainstream semiconductor device researchers to gain some insight into the world of magnetism, seen as a first and critical step towards realization of devices.

Due to small spin orbit coupling and small inter-atomic spacing, in addition to more intricate reasons,

GaN and ZnO could potentially exhibit ferromagnetism when doped with transition metals (TM) or rare earths with unpaired partially empty 3*d* and 4*f* shells, respectively. Intuitively, the smaller lattice constant of GaN and ZnO, compared to the conventional II–VI and III–V semiconductors, would serve to increase the magnetic coupling strength among the magnetic ions through indirect exchange interaction. However, the caveat is that, at least in the modified mean-field theory of Dietl *et al.*, TM concentrations near 5% or higher and acceptor concentrations above 10<sup>20</sup> cm<sup>-3</sup> are needed to observe above room temperature Curie temperatures. We must mention that mean field theory might overestimate the Curie temperature, particularly for low magnetic ion concentrations. While the above room temperature Curie temperature aspect of that theory is cited often, the conditions on which that temperature hinges are often left out of the critical discussion.

On the experimental side it is still not sufficiently clear if the uniformly doped host or some other phase is responsible for the observed magnetic hysteresis persisting in some cases up to 940 K. Moreover, the transition energies induced by transition elements, particularly in GaN, are not yet well understood. It is reasonable to expect that only certain states of the TM element (after they are split by crystal field splitting and Zeeman splitting which is to be enhanced by large spin exchange interaction) contribute to interactions supporting the ferromagnetic state. The same to a varying degree holds for ZnO as well. Data in favor and against ferromagnetism in both GaN and ZnO have been reported. Arguments and counter arguments for or against have been made. At least for the time being, the field still appears too controversial and confusing, as the local environment and energy levels of magnetic ions are too sketchy and mechanism(s) leading to ferromagnetism are too many, not to mention the ever varying sample quality. In this review, an attempt was made to discuss those reports with short comments regarding any inconsistencies and difficulties as far as the mechanisms and experimental methods are concerned. In short, not only are the various reported experiments inconsistent, the same also holds for the effort on the theoretical side.

On the theoretical side, it is not clear which of the many mechanisms put forth is applicable and in what kind of samples. For example direct superexchange between magnetic ions is antiferromagnetic in the realm of the Zener theory, but indirect exchange interaction between the magnetic ions can lead to ferromagnetism in the realm of Zener and Ruderman-Kittel-Kasuya-Yoshida (RKKY) theories. In one electron systems, the *d* wavefunctions of the transition metals and *s* wavefunctions of the host (conduction electrons) are orthogonal and could not hybridize in a cubic system. However, the hybridization of *d* wavefunctions of the transition elements and *p*-states of the host (valence band) is strong and can lead to ferromagnetism. The picture in wide bandgap semiconductors is complex in that the level splitting and associated hybridization are dopant and doping level dependent. As such simple arguments, while instructive, may not strictly apply. Mean-field theory, expanded by Dietl *et al.* to include

the anisotropy of the valence band spin orbit interaction, indicates holemediated mechanism to be dominant. In the realm of this theory, ZnO has to be convincingly *p*-type and yet ferromagnetism in *n*-type samples has been reported. In fact, donor doped samples along with TM doping have been reported to be ferromagnetic and the constructive role of conduction electrons have been touted. In contrast, doping with elements which would tend to reduce the background electron concentration, have also been touted to be the mechanism for the experimentally observed ferromagnetism. Moreover, magnetization in electron co-doped samples has been attributed to bound polarons. A bound polaron is formed when the magnetic moment of the ion is aligned with the spin of an exciton and the magnetic ion within its radius. The exciton in turn renders the spin of nearby excitons to align, which in turn is parallel to the spin of a nearby magnetic ion, and so on.

Clearly, the field is in its infancy and the picture is rather complex. It is quite possible that the strict theories mentioned above are not necessarily applicable to all samples. *ab initio* calculations are more likely to provide a guiding light for experimentalists to focus on exploring those transition or rare earth elements which are more likely to be ferromagnetic in GaN and ZnO hosts. A case in point is Mn in these two hosts. For example, some theories suggest Mn not leading to ferromagnetism in ZnO, and yet this TM in ZnO has been extensively investigated by experimentalist and reported to be ferromagnetic. A similar situation applies to GaN doped with Mn in that the theory indicates that in lightly and heavily doped samples the ferromagnetic phase is not stabilized. The doping levels which lead to a particular class of levels splitting are required for (Ga, Mn)N to be stabilized in the ferromagnetic state. This simply means that more detailed and probing investigations are necessary to sort out the various experimental data that have been reported.

In closing, it is not an overstatement that the expected advantages of GaN-and ZnO-based spintronics are truly exciting although the efforts in materials science and devices are still in their embryonic stage. Moreover, there are many challenges to consider including whether high ferromagnetic transition temperature and carrier-mediated ferromagnetism can be realized. In addition to a ferromagnetic semiconductor, successful operation of spintronic devices also requires the support of spin-polarized transport in the device and the amplification and detection of spin polarization (or spin polarized current). With accelerated research efforts toward room temperature ferromagnetism in GaN and ZnO, and perhaps other oxide based DMS materials, it might be possible to realize semiconductor magnetoelectronics. Perhaps the “real” utilization of the spin degree of freedom in spin-based all-semiconductor multifunctional devices such as spin-FETs, spin-LEDs, spin resonant tunneling device (RTD), sensitive magnetic sensor, high density nonvolatile memory, and quantum bits for quantum processing will be a reality even if to some limited degree of present expectations. If so, this would represent a truly new chapter in the annals of semiconductor based devices.

## Acknowledgments

The work at VCU is supported by grants from Air Force Office of Scientific Research (Drs. G. L. Witt, G. Pomrenke, and T. Steiner), Office of Naval Research (Dr. C. E. C. Wood), National Science Foundation (Dr. L. Hess), and American Petroleum Institute, and Missile Defense Agency (MDA) through Air Force Laboratory (Wright Patterson under the direction of Dr. C.W. Litton). The authors would like to recognize their collaborations with Cermet Inc., especially Dr. R. Varatharajan and Jeff Nause, discussions with Professors G. P. Das, the late B. K. Rao, P. Jena, and Dr. Q. Wang at VCU Physics department, and Prof. J. K. Furdyna. The authors also acknowledge their collaborators, Prof. P. Ruterana, and W. Walukiewicz. Finally, preprints/presentations provided by and or discussions with Dr. S-H Wei, Prof. Chia-Ling Chien, Prof. S. Pearton, Prof. N. Newman, Prof. N. El-Masry, Prof. H. Katayama-Yoshida, and W. M. Chen are greatly acknowledged. Last but not least, supply of high quality figures from many of referenced authors is gratefully acknowledged. Constructive comments by reviewers enhanced the clarity of the paper.

## Appendices

### A. List of acronyms

DMS	diluted magnetic semiconductor
FM	ferromagnetic
AFM	antiferromagnetic
FC	field-cooled
ZFC	zero-field-cooled
MBE	molecular beam epitaxy
MOCVD	metalorganic chemical vapor deposition
PLD	pulsed laser deposition
RKKY	Ruderman-Kittel-Kasuya-Yoshida
DFT	density functional theory
LDA	local (spin) density approximation
GGA	generalized gradient approximation
CPA	coherent potential approximation
LAPW	linearized augmented plane wave
DOS	density of states
CFR	crystal-field resonance
DBH	dangling bond hybrid
VBM	valence band maximum
MCD	magnetic circular dichroism
SQUID	superconducting quantum interference device
PL	photoluminescence
PLE	PL excitation
CL	Cathodoluminescence
EXAFS	extended X-ray absorption fine structure
NEXAFS	near-edge X-ray absorption fine structure
SEM	scanning electron microscope
RHEED	reflection high energy electron diffraction
TEM	transmission electron microscope
EPMA	electron probe microanalysis
SIMS	secondary ion mass spectrometry
RBS	Rutherford backscattering
EDS	energy dispersive spectroscopy
EPR	electron paramagnetic resonance
XPS	X-ray photoelectron spectroscopy
XAS	X-ray absorption spectroscopy

**B. Units of magnetic properties.**  
**Multiplication of a number in Gaussian units by the conversion factor  $C$  to converts it to the SI unit.**

Quantity	Symbol	Gaussian & CGS emu	Conversion factor $C$	SI unit
Magnetic flux	$\Phi$	maxwell, (Mx), $G \cdot cm^2$	$10^{-8}$	Weber (Wb)
Magnetic flux density	$B$	gauss (G)	$10^{-4}$	Tesla (T), $Wb/m^2$
Magnetic field strength	$H$	oersted (Oe)	$10^3/4\pi$	A/m
(Volume) magnetization	$M$	emu/cm <sup>3</sup>	$10^3$	A/m
(Mass) magnetization	$M$	emu/g	1	A·m <sup>2</sup> /kg
			$4\pi \times 10^{-7}$	Wb·m/kg
Magnetic moment	$m$	emu	$10^{-3}$	A·m <sup>2</sup> , J/T

**References**

1. J. K. FURDYNA, *J. Appl. Phys.* **64** (1988) R29.
2. H. OHNO, *Science* **281** (1998) 951.
3. T. DIETL, H. OHNO, F. MATSUKURA, J. CIBERT and D. FERRAND, *ibid.* **287** (2000) 1019.
4. K. SATO and H. KATAYAMA-YOSHIDA, *Jpn. J. Appl. Phys.* **40** (2001) L334.
5. G. P. DAS, B. K. RAO and P. JENA, *Phys. Rev. B* **69** (2004) 214422.
6. N. THEODOROPOULOU, A. F. HEBARD, M. E. OVERBERG, C. R. ABERNATHY, S. J. PEARTON, S. N. G. CHU and R. G. WILSON, *Appl. Phys. Lett.* **78** (2001) 3475.
7. G. T. THALER, M. E. OVERBERG, B. GILA, R. FRAZIER, C. R. ABERNATHY, S. J. PEARTON, J. S. LEE, S. Y. LEE, Y. D. PARK, Z. G. KHIM, J. KIM and F. REN, *ibid.* **80** (2002) 3964.
8. M. E. OVERBERG, C. R. ABERNATHY, S. J. PEARTON, N. A. THEODOROPOULOU, K. T. MCCARTHY and A. F. HEBARD, *ibid.* **79** (2001) 1312.
9. K. H. KIM, K. J. LEE, D. J. KIM, H. J. KIM, Y. E. IHM, D. DJAYAPRAWIRA, M. TAKAHASHI, C. S. KIM, C. G. KIM and S. H. YOO, *ibid.* **82** (2003) 1775.
10. M. C. PARK, K. S. KUH, J. M. MYOUNG, J. M. LEE, J. Y. CHANG, K. I. LEE, S. H. HAN and W. Y. LEE, *Solid State Commun.* **124** (2002) 11.
11. J. Y. CHANG, G. H. KIM, J. M. LEE, S. H. HAN, W. Y. LEE, M. H. HAN, K. S. HUH and J. M. MYOUNG, *J. Appl. Phys.* **93** (2003) 7858.
12. S. SONODA, S. SHIMIZU, T. SASAKI, Y. YAMAMOTO and H. HORI, *J. Cryst. Growth* **237** (2002) 1358.
13. D. S. HAN, J. PARK, K. W. RHIE, S. KIM and J. CHANG, *Appl. Phys. Lett.* **86** (2005) 032506.
14. M. L. REED, N. A. EL-MASRY, H. H. STADELMAIER, M. E. RITUMS, M. J. REED, C. A. PARKER, J. C. ROBERTS and S. M. BEDAIR, *ibid.* **79** (2001) 3473.
15. M. ZAJAC, J. GOSK, E. GRZANKA, M. KAMIŃSKA, A. TWARDOWSKI, B. STROJEK, T. SZYSZKO and S. PODSIADŁO, *J. Appl. Phys.* **93** (2003) 4715.
16. M. B. HAIDER, C. L. CONSTANTIN, H. ALBRITEN, H. YANG, E. TRIFAN, D. INGRAM, A. R. SMITH, C. V. KELLY and Y. IJIRI, *ibid.* **93** (2003) 5274.
17. R. FRAZIER, G. THALER, M. OVERBERG, B. GILA, C. R. ABERNATHY and S. J. PEARTON, *Appl. Phys. Lett.* **83** (2003) 1758.
18. H. X. LIU, S. Y. WU, R. K. SINGH, L. GU, D. J. SMITH, N. NEWMAN, M. R. DILLEY, L. MONTES and M. B. SIMMONDS, *ibid.* **85** (2004) 4076.
19. S. E. PARK, H.-J. LEE, Y. C. CHO, S.-Y. JEONG, C. R. CHO and S. CHO, *ibid.* **80** (2002) 4187.
20. M. HASHIMOTO, Y.-K. ZHOU, M. KANAKURA and H. ASAHII, *Solid State Commun.* **122** (2002) 37.
21. S. Y. WU, H. X. LIU, L. GU, R. K. SINGH, L. BUDD, M. VAN SCHILFGAARDE, M. R. MCCARTNEY, D. J. SMITH and N. NEWMAN, *Appl. Phys. Lett.* **82** (2003) 3047.
22. S. Y. WU, H. X. LIU, L. GU, R. K. SINGH, M. VAN SCHILFGAARDE, D. J. SMITH, M. DILLEY, L. MONTES, M. B. SIMMONDS and N. NEWMAN, *Mat. Res. Soc. Symp. Proc.* **798** (2004) Y10.57.
23. J. S. LEE, J. D. LIM, Z. G. KHIM, Y. D. PARK, S. J. PEARTON and S. N. G. CHU, *J. Appl. Phys.* **93** (2003) 4512.
24. Y. SHON, Y. H. KWON, Y. S. PARK, SH. U. YULDASHEV, S. J. LEE, C. S. PARK, K. J. CHUNG, S. J. YOON, H. J. KIM, W. C. LEE, D. J. FU, T. W. KANG, X. J. FAN, Y. J. PARK and H. T. OH, *ibid.* **95** (2004) 761.
25. S. DHAR, O. BRANDT, M. RAMSTEINER, V. E. SAPEGA and K. H. PLOOG, *Phys. Rev. Lett.* **94** (2005) 037205.
26. S. W. JUNG, S.-J. AN, G.-C. YI, C. U. JUNG, S.-I. LEE and S. CHO, *Appl. Phys. Lett.* **80** (2002) 4561.
27. Y. W. HEO, M. P. IVILL, K. IP, D. P. NORTON and S. J. PEARTON, *ibid.* **84** (2004) 2292.
28. D. P. NORTON, S. J. PEARTON, A. F. HEBARD, N. THEODOROPOULOU, L. A. BOATNER and R. G. WILSON, *ibid.* **82** (2003) 239.
29. H.-J. LEE, S.-Y. JEONG, C. R. CHO and C. H. PARK, *ibid.* **81** (2002) 4020.
30. K. ANDO, H. SAITO, Z. JIN, T. FUKUMURA, M. KAWASAKI, Y. MATSUMOTO and H. KOINUMA, *J. Appl. Phys.* **89** (2001) 7284.
31. K. ANDO, H. SAITO, Z. JIN, T. FUKUMURA, M. KAWASAKI, Y. MATSUMOTO and H. KOINUMA, *Appl. Phys. Lett.* **78** (2001) 2700.
32. K. ANDO, *ibid.* **82** (2003) 100.
33. Y. M. CHO, W. K. CHOO, H. KIM, D. KIM and Y. E. IHM, *ibid.* **80** (2002) 3358.
34. S. W. YOON, S.-B. CHO, S. C. WE, S. YOON, B. J. SUH, H. K. SONG and Y. J. SHIN, *J. Appl. Phys.* **93** (2003) 7879.
35. J. H. KIM, H. KIM, Y. E. IHM and W. K. CHOO, *ibid.* **92** (2002) 6066.
36. C. ZENER, *Phys. Rev.* **81** (1951) 440.
37. *Idem.*, *ibid.* **82** (1951) 403.
38. *Idem.*, *ibid.* **83** (1951) 299.
39. J. S. BLAKEMORE, "Solid State Physics", 2nd Edition, (Cambridge University Press, New York 1985).
40. N. W. ASHCROFT and N. D. MERMIN, "Solid State Physics" (Holt-Reinhart-Winston, New York 1976).
41. H. OHNO, H. MUNEKATA, S. VON MOLNAR and L. L. CHANG, *J. Appl. Phys.* **69** (1991) 6103.
42. S. J. PEARTON, C. R. ABERNATHY, M. E. OVERBERG, G. T. THALER, D. P. NORTON, N. THEODOROPOULOU, A. F. HEBARD, Y. D. PARK, F. REN, J. KIM and L. A. BOATNER, *ibid.* **93** (2003) 1.
43. S. J. PEARTON, C. R. ABERNATHY, G. T. THALER, R. M. FRAZIER, D. P. NORTON, F. REN, Y. D. PARK, J. M. ZAVADA, I. A. BUYANOVA, W. M. CHEN and A. F. HEBARD, *J. Phys.: Condens. Mater.* **16** (2004) R209.
44. IGOR ŽUTIĆ, JAROSLAV FABIAN and S. DAS SARMA, *Rev. Mod. Phys.* **76** (2004) 323.
45. S. J. PEARTON, C. R. ABERNATHY, B. P. GILA, F. REN, J. M. ZAVADA and Y. D. PARK, *Solid-State Electron.* **48** (2004) 1965.
46. T. GRAF, S. T. B. GOENNENWEIN and M. S. BRANDT, *Phys. Stat. Sol. (b)* **239** (2003) 277.
47. G. PRINZ, *Science* **282** (1998) 1660.
48. T. STORY, R. R. GALAZKA, R. B. FRANKEL and P. A. WOLFF, *Phys. Rev. Lett.* **56** (1986) 777.
49. K. SATO and H. KATAYAMA-YOSHIDA, *Jpn J. Appl. Phys.* **39** (2000) L555.

50. H. AKAI and P. H. DEDERICH, *Phys. Rev. B* **47** (1993) 8739.
51. H. AKAI, *Phys. Rev. Lett.* **81** (1998) 3002.
52. P. HOHENBERG and W. KOHN, *Phys. Rev.* **136** (1964) 864.
53. W. KOHN and L. J. SHAM, *ibid.* **140** (1965) 1133.
54. K. SATO and H. KATAYAMA-YOSHIDA, *Physica B* **308** (2001) 904.
55. M. BERCIU and R. N. BHATT, *Phys. Rev. Lett.* **87** (2001) 107203.
56. A. KAMINSKI and S. DAS SARMA, *ibid.* **88** (2001) 247201.
57. T. DIETL, F. MATSUKURA and H. OHNO, *Phys. Rev. B* **66** (2002) 033203.
58. S. DAS SARMA, E. H. HWANG and A. KAMINSKI, *ibid.* **67** (2003) 155201.
59. J. WARNOCK and P. A. WOLFF, *ibid.* **31** (1985) 6579.
60. M. SAWICKI, T. DIETL, J. KOSSUT, J. IGALSON, T. WOJTIWICZ and W. PLESIEWICZ, *Phys. Rev. Lett.* **56** (1986) 508.
61. J. M. D. COEY, M. VENKATESAN and C. B. FITZGERALD, *Nat. Mater.* **4** (2005) 73.
62. T. DIETL and J. SPALEK, *Phys. Rev. Lett.* **48** (1982) 355.
63. T. DIETL, H. OHNO and F. MATSUKURA, *Phys. Rev. B* **63** (2001) 195205.
64. T. DIETL, *J. Appl. Phys.* **89** (2001) 7437.
65. *Idem.*, *Semicond. Sci. Technol.* **17** (2002) 377.
66. T. JUNGWIRTH, W. A. ATKINSON, B. LEE and A. H. MACDONALD, *Phys. Rev. B* **59** (1999) 9818.
67. K. SATO and H. KATAYAMA-YOSHIDA, *Jpn. J. Appl. Phys.* **40** (2001) L651.
68. *Idem.*, *Physica E* **10** (2001) 251.
69. T. YAMAMOTO and H. KATAYAMA-YOSHIDA, *Jpn. J. Appl. Phys.* **38** (1999) L166.
70. H. KATAYAMA-YOSHIDA and K. SATO, *Physica B* **327** (2003) 337.
71. K. SATO and H. KATAYAMA-YOSHIDA, *Semicond. Sci. Technol.* **17** (2002) 367.
72. P. SHARMA, A. GUPTA, K. V. RAO, F. J. OWENS, R. SHARMA, R. AHUJA, J. M. OSORIO GUILLEN, B. JOHANSSON and G. A. GEHRING, *Nat. Mater.* **2** (2003) 673.
73. T. MIZOKAWA, T. NAMBU, A. FUJIMORI, T. FUKUMURA and M. KAWASAKI, *Phys. Rev. B* **65** (2002) 085209.
74. C.-H. CHIEN, S. H. CHIOU, G. Y. GUO and Y.-D. YAO, *J. Magnetism Magnetic Mater.* **282** (2004) 275.
75. S. Y. YUN, G.-B. CHA, Y. KWON, S. CHO, S. C. SOON and C. HONG, *ibid.* **272–276**, Supplement 1 (2004) E1563.
76. E.-C. LEE and K. J. CHANG, *Phys. Rev. B* **69** (2004) 085205.
77. Q. WANG and P. JENA, *Appl. Phys. Lett.* **84** (2004) 4170.
78. Q. WANG, Q. SUN, B. K. RAO and P. JENA, *Phys. Rev. B* **69** (2004) 233310.
79. Q. WANG, Q. SUN, P. JENA and Y. KAWAZOE, *ibid.* **70** (2004) 052408.
80. X. FENG, *J. Phys.: Condens. Matter* **16** (2004) 4251.
81. S.-J. HAN, J. W. SONG, C.-H. YANG, S. H. PARK, J.-H. PARK, Y. H. JEONG and K. W. RHIE, *Appl. Phys. Lett.* **81** (2002) 4212.
82. H.-T. LIN, T.-S. CHIN, J.-C. SHIH, S.-H. LIN, T.-M. HONG, R.-T. HUANG, F.-R. CHEN and J.-J. KAI, *ibid.* **85** (2004) 621.
83. N. A. SPALDIN, *Phys. Rev. B* **69** (2004) 125201.
84. M. S. PARK and B. I. MIN, *ibid.* **68** (2003) 224436.
85. M. VENKATESAN, C. B. FITZGERALD, J. G. LUNNEY and J. M. D. COEY, *Phys. Rev. Lett.* **93** (2004) 177206.
86. V. I. LITVINOV and V. K. DUGAEV, *ibid.* **86** (2001) 5593.
87. H. KATAYAMA-YOSHIDA, R. KATO and T. YAMAMOTO, *J. Cryst. Growth* **231** (2001) 428.
88. K. SATO and H. KATAYAMA-YOSHIDA, *Jpn. J. Appl. Phys.* **40** (2001) L485.
89. M. VAN SCHILFGAARDE and O. N. MYRASOV, *Phys. Rev. B* **63** (2001) 233205.
90. T. JUNGWIRTH, W. A. ATKINSON, B. H. LEE and A. H. MACDONALD, *ibid.* **59** (1999) 981.
91. G. P. DAS, B. K. RAO and P. JENA, *ibid.* **68** (2003) 035207.
92. Q. WANG, Q. SUN and P. JENA, *Phys. Rev. Lett.* **93** (2004) 155501.
93. K. SATO, W. SCHWEIKA, P. H. DEDERICH and H. KATAYAMA-YOSHIDA, *Phys. Rev. B* **70** (2004) 201202.
94. L. KRONIK, M. JAIN and J. R. CHELIKOWSKY, *ibid.* **66** (2002) 041203.
95. E. KULATOV, H. NAKAYAMA, H. MARIETTE, H. OHTA and YU. A. USPENSKII, *ibid.* **66** (2002) 045203.
96. B. SANYAL, O. BENGONE and S. MIRBT, *ibid.* **68** (2003) 205210.
97. P. MAHADEVAN and A. ZUNGER, *Appl. Phys. Lett.* **85** (2004) 2860.
98. *Idem.*, *Phys. Rev. B* **69** (2004) 115211.
99. G. M. DALPIAN, SU-HUAI WEI, X. G. GONG, A. J. R. DA SILVA and A. FAZZIO (to be published).
100. G. M. DALPIAN and S.-H. WEI, "Transition from Ferromagnetism to Antiferromagnetism in GaMnN", to be published.
101. J. J. KIM, H. MAKINO, K. KOBAYASHI, Y. TAKATA, T. YAMAMOTO, T. HANADA, M. W. CHO, E. IKENAGA, M. YABASHI, D. MIWA, Y. NISHINO, K. TAMASAKU, T. ISHIKAWA, S. SHIN and T. YAO, *Phys. Rev. B* **70** (2004) 161315.
102. J. HONG and R. Q. WU, *ibid.* **68** (2003) 233306.
103. G. M. DALPIAN and S.-H. WEI, "Electron-induced stabilization of ferromagnetism in GaGdN", to be published.
104. G. THALER, R. FRAZIER, B. GILAR, J. STAPLETON, M. DAVIDSON, C. R. ABERNATHY, S. J. PEARTON and C. SEGRE, *Appl. Phys. Lett.* **84** (2004) 2578.
105. S. S. A. SEO, M. W. KIM, Y. S. LEE, T. W. NOH, Y. D. PARK, G. T. THALER, M. E. OVERBERG, C. R. ABERNATHY and S. J. PEARTON, *ibid.* **82** (2003) 4749.
106. S. DHAR, O. BRANDT, A. TRAMPERT, K. J. FRIEDLAND, Y. J. SUN and K. H. PLOOG, *Phys. Rev. B* **67** (2003) 165205.
107. F. MATSUKURA, E. ABE, Y. OHNO and H. OHNO, *Appl. Surf. Sci.* **159–160** (2000) 265.
108. S. DHAR, O. BRANDT, A. TRAMPERT, L. DÄWERITZ, K. J. FRIEDLAND, K. H. PLOOG, J. KELLER, B. BESCHOTEN and G. GÜNTHERODT, *Appl. Phys. Lett.* **82** (2003) 2077.
109. B. GRANDIDIER, J. P. NYS, C. DELERUE, D. STIEVENARD, Y. HIGO and M. TANAKA, *ibid.* **77** (2000) 4001.
110. K. M. YU, W. WALUKIEWICZ, T. WOJTIWICZ, I. KURLISZYN, X. LIU, Y. SASAKI and J. K. FURDYNA, *Phys. Rev. B* **65** (2002) 201303.
111. T. DIETL, *Nat. Mater.* **2** (2003) 646.
112. B. A. BUNKER, W.-F. PONG, V. DEBSKA, D. R. YODER-SHORT and J. F. FURDYNA, "Diluted Magnetic (Semimagnetic) Semiconductors", edited by R. L. Aggarwal, J. K. Furdyna, and S. von Molnar (Materials Research Society, Pittsburgh, PA, 1987), vol. 89, p. 231.
113. A. TSUKAZAKI, A. OHTOMO, T. ONUMA, M. OHTANI, T. MAKINO, M. SUMIYA, K. OHTANI, S. F. CHICHIBU, S. FUKU, Y. SEGAWA, H. OHNO, H. KOINUMA and M. KAWASAKI, *Nat. Mater.* **4** (2005) 42.
114. Ü. ÖZGÜR, YA. I. ALIVOV, C. LIU, A. TEKE, M. RESHCHIKOV, S. DOČAN, V. AVRUTIN, S.-J. CHO and H. MORKOÇ, *J. Appl. Phys. Review* (2005), in press.
115. T. FUKUMURA, Z. JIN, A. OHTOMO, H. KOINUMA and M. KAWASAKI, *Appl. Phys. Lett.* **75** (1999) 3366.
116. For details of MBE growth, see M.A. Herman and H. Sitter, "Molecular Beam Epitaxy: Fundamentals and Current Status", 2nd edition (Springer, Berlin, 1996).
117. For details of MOCVD growth, see G. B. Stringfellow, "Organometallic Vapor-Phase Epitaxy: Theory and Practice", 2nd edition (Academic, London, 1999).
118. For details of PLD growth, see Douglas B. Chrisey and Graham K. Hubler, "Pulsed laser deposition of thin films" (J. Wiley, New York, 1994).
119. K. UEDA, H. TABATA and T. KAWAI, *Appl. Phys. Lett.* **79** (2001) 988.
120. T. WAKANO, N. FUJIMURA, Y. MORINAGA, N. ABE, A. ASHIDA and T. ITO, *Physica E* **10** (2001) 260.

121. H. SAEKI, H. TABATA and T. KAWAI, *Solid State Commun.* **120** (2001) 439.
122. T. FUKUMURA, Z. JIN, M. KAWASAKI, T. SHONO, T. HASEGAWA, S. KOSHIHARA and H. KOINUMA, *Appl. Phys. Lett.* **78** (2001) 958.
123. Z. JIN, T. FUKUMURA, M. KAWASAKI, K. ANDO, H. SAITO, T. SEKIGUCHI, Y. Z. YOO, M. MURAKAMI, Y. MATSUMOTO, T. HASEGAWA and H. KOINUMA, *ibid.* **78** (2001) 3824.
124. A. TIWARI, C. JIN, A. KVIT, D. KUMAR, J. F. MUTH and J. NARAYAN, *Solid State Commun.* **121** (2002) 371.
125. G. LAWES, A. S. RISBUD, A. P. RAMIREZ and R. SESHADRI, *Phys. Rev. B* **71** (2005) 045201.
126. M. H. KANE, K. SHALINI, C. J. SUMMERS, R. VARATHARAJAN, J. NAUSE, C. R. VESTAL, Z. J. ZHANG and I. T. FERGUSON, *J. Appl. Phys.* **97** (2005) 023906.
127. S. J. PEARTON, D. P. NORTON, K. IP and Y. W. HEO, *J. Vac. Sci. Technol. B* **22** (2004) 932.
128. X. M. CHENG and C. L. CHIEN, *J. Appl. Phys.* **93** (2003) 7876.
129. S. LIM, M. JEONG, M. HAM and J. MYOUNG, *Jpn. J. Appl. Phys.* **2B** **43** (2004) L280.
130. M. IVILL, S. J. PEARTON, D. P. NORTON, J. KELLY and A. F. HEBARD, *J. Appl. Phys.* **97** (2005) 053904.
131. D. P. NORTON, M. E. OVERBERG, S. J. PEARTON, K. PRUESSNER, J. D. BUDAI, L. A. BOATNER, M. F. CHISHOLM, J. S. LEE, Z. G. KHIM, Y. D. PARK and R. G. WILSON, *Appl. Phys. Lett.* **83** (2003) 5488.
132. K. RODE, A. ANANE, R. MATTANA, J.-P. CONTOUR, O. DURAND and R. LEBOURGEOIS, *J. Appl. Phys.* **93** (2003) 7676.
133. S. G. YANG, A. B. PAKHOMOV, S. T. HUNG and C. Y. WONG, *IEEE Trans. Magn.* **38** (2002) 2877.
134. N. JEDRECY, H. J. VON BARDELEBEN, Y. ZHENG and J.-L. CANTIN, *Phys. Rev. B* **69** (2004) 041308.
135. A. C. TUAN, J. D. BRYAN, A. B. PAKHOMOV, V. SHUTTHANANDAN, S. THEVUTHASAN, D. E. MCCREADY, D. GASPARD, M. H. ENGELHARD, J. W. ROGERS, JR., K. KRISHNAN, D. R. GAMELIN and S. A. CHAMBERS, *ibid.* **70** (2004) 054424.
136. N. HONG, V. BRIZE and J. SAKAI, *Appl. Phys. Lett.* **86** (2005) 082505.
137. T. FUKUMURA, Y. YAMADA, H. TOYOSAKI, T. HASEGAWA, H. KOINUMA and M. KAWASAKI, *Appl. Surf. Sci.* **223** (2004) 62.
138. S. KOLESNIK and B. DABROWSKI, *J. Appl. Phys.* **96** (2004) 5379.
139. L. W. GUO, D. L. PENG, H. MAKINO, K. INABA, H. J. KO, K. SUMIYAMA and Y. YAO, *J. Magn. Magn. Mater.* **213** (2000) 321.
140. A. CHARTIER, P. D'ARCO, R. DOVESI and V. R. SAUNDERS, *Phys. Rev. B* **60** (1999) 14042.
141. S.-J. HAN, T.-H. JANG, Y. B. KIM, B.-G. PARK, J.-H. PARK and Y. H. JEONG, *Appl. Phys. Lett.* **83** (2003) 920.
142. C. LIU, F. YUN, B. XIAO, S.-J. CHO, Y.-T. MOON, H. MORKOÇ, M. ABOUZAIID, P. RUTERANA, K. M. YU and W. WALUKIEWICZ, *J. Appl. Phys.* (2005) in the press.
143. S. KOLESNIK, B. DABROWSKI and J. MAIS, *J. Appl. Phys.* **95** (2004) 2582.
144. W. H. BRUMAGE, C. F. DORMAN and C. R. QUADE, *Phys. Rev. B* **63** (2001) 104411.
145. J. SHIM, T. HWANG, S. LEE, J. PARK, S. HAN and Y. H. JEONG, *Appl. Phys. Lett.* **86** (2005) 082503.
146. For more specific information of these characterization methods, the readers are referred to C. R. Brundle, C. A. Evans, Jr., and S. Wilson, "Encyclopedia of materials characterization: Surfaces, Interfaces, Thin Films" (Butterworth-Heinemann, London, 1992).
147. Z. JIN, Y.-Z. YOO, T. SEKIGUCHI, T. CHIKYOW, H. OFUCHI, H. FUJIOKA, M. OSHIMA and H. KOINUMA, *Appl. Phys. Lett.* **83** (2003) 39.
148. K. R. KITTLSTVED, N. S. NORBERG and D. R. GAMELIN, *Phys. Rev. Lett.* **94**, (2005) 147209.
149. Y. M. KIM, M. YOON, I.-W. PARK, Y. J. PARK and JONG H. LYOU, *Solid State Commun.* **129** (2004) 175.
150. M. KUNISU, F. OBA, H. IKENO, I. TANAKA and T. YAMAMOTO, *Appl. Phys. Lett.* **86** (2005) 121902.
151. A. F. JALBOUT, H. CHEN and S. L. WHITTENBURG, *ibid.* **81** (2002) 2217.
152. S. RAMACHANDRAN, A. TIWARI and J. NARAYAN, *ibid.* **84** (2004) 5255.
153. S.-W. LIM, D.-K. HWANG and J.-M. MYOUNG, *Solid State Commun.* **125** (2003) 231.
154. A. S. RISBUD, N. A. SPALDIN, Z. Q. CHEN, S. STEMMER and RAM SESHADRI, *Phys. Rev. B* **68** (2003) 205202.
155. P. KOIDL, *ibid.* **15** (1977) 2493.
156. Z. JIN, M. MURAKAMI, T. FUKUMURA, Y. MATSUMOTO, A. OHTOMO, M. KAWASAKI and H. KOMUMA, *J. Cryst. Growth* **214–215** (2000) 55.
157. Z.-W. JIN, T. FUKUMURA, K. HASEGAWA, Y.-Z. YOO, K. ANDO, T. SEKIGUCHI, P. AHMET, T. CHIKYOW, T. HASEGAWA, H. KOINUMA and M. KAWASAKI, *ibid.* **237** (2002) 548.
158. Y. ISHIDA, J.-I. HWANG, M. KOBAYASHI, A. FUJIMORI, H. SAEKI, H. TABATA and T. KAWAI, *Physica B* **351** (2004) 304.
159. N. H. HONG, J. SAKAI and A. HASSINI, *J. Phys.: Condens. Matter.* **17** (2005) 199.
160. D. A. SCHWARTZ, K. R. KITTLSTVED and D. R. GAMELIN, *Appl. Phys. Lett.* **85** (2004) 1395.
161. P. V. RADOVANOVIC and D. R. GAMELIN, *Phys. Rev. Lett.* **91** (2003) 157202.
162. K. ANDO, T. HAYASHI, M. TANAKA and A. TWARDOWSKI, *J. Appl. Phys.* **83** (1998) 6548.
163. K. ANDO, H. I. SAITO, V. ZAYETS and M. C. DEBNATH, *J. Phys.: Condens. Matter.* **16** S5541 (2004) S5541.
164. K. ANDO, "Magneto-optics (Springer Series in Solid-State Science)", edited by S. Sugano and N. Kojima (Springer, Berlin, 2000) vol. 128, p. 211.
165. T. SEKIGUCHI, K. HAGA and K. INABA, *J. Cryst. Growth.* **214** (2000) 68.
166. See for example H. Morkoç, "Nitride Semiconductors and Devices", 2nd edition (Springer, New York, 2006).
167. T. SASAKI, S. SONODA, Y. YAMAMOTO, K. SUGA, S. SHIMIZU, K. KINDO and H. HORI, *J. Appl. Phys.* **91** (2002) 7911.
168. K. H. PLOOG, S. DHAR and A. TRAMPERT, *J. Vac. Sci. Technol. B* **21** (2003) 1756.
169. V. A. CHITTA, J. A. H. COAQUIRA, J. R. L. FERNANDEZ, C. A. DUARTE, J. R. LEITE, D. SCHIKORA, D. J. AS, K. LISCHKA and E. ABRAM, *Appl. Phys. Lett.* **85** (2004) 3777.
170. M. A. BOSELLI, I. C. DA CUNHA LIMA, J. R. LEITE, A. TROPER and A. GHAZALI, *ibid.* **84** (2004) 1138.
171. F. L. DEEPAK, P. V. VANITHA, A. GOVINDARAJ and C. N. R. RAO, *Chem. Phys. Lett.* **374** (2003) 314.
172. M. ZAJAC, R. DORADZINSKI, J. GOSK, J. SZCZYTKO, M. LEFELD-SOSNOWSKA, M. KAMINSKA, A. TWARDOWSKI, M. PALCZEWSKA, E. GRZANKA and W. GEBICKI, *Appl. Phys. Lett.* **78** (2001) 1276.
173. T. GRAF, M. GJUKIC, M. S. BRANDT, M. STUTZMANN and O. AMBACHER, *ibid.* **81** (2002) 5159.
174. T. GRAF, M. GJUKIC, M. HERMANN, M. S. BRANDT, M. STUTZMANN, L. GÖRGENS, J. B. PHILLIP and O. AMBACHER, *J. Appl. Phys.* **93** (2003) 9697.
175. A. WOLOS, M. PALCZEWSKA, M. ZAJAC, J. GOSK, M. KAMINSKA, A. TWARDOWSKI, M. BOCKOWSKI, I. GRZEGORY and S. POROWSKI, *Phys. Rev. B* **69** (2004) 115210.
176. M. J. REED, F. E. ARKUN, E. A. BERKMAN, N. A. ELMASRY, J. ZAVADA, M. O. LUEN, M. L. REED and S. M. BEDAIR, *Appl. Phys. Lett.* **86** (2005) 102504.
177. F. E. ARKUN, M. J. REED, E. A. BERKMAN, N. A. EL-MASRY, J. M. ZAVADA, M. L. REED and S. M. BEDAIR, *ibid.* **85** (2004) 3809.

178. J. M. BAIK, Y. SHON, T. W. KANG and J.-L. LEE, *ibid.* **84** (2004) 1120.
179. J. M. BAIK, S. U. KIM, Y. M. KOO, T. W. KANG and J.-L. LEE, *Solid State Lett.* **7** (2004) G313.
180. G. THALER, R. FRAZIER, B. GILA, J. STAPLETON, M. DAVIDSON, C. R. ABERNATHY, S. J. PEARTON and C. SEGREGRE, *Appl. Phys. Lett.* **84** (2004) 1314.
181. J. KREISSL, W. ULRICI, M. EL-METOU, A. M. VASSON, A. VASSON and A. GAVAIX, *Phys. Rev. B* **54** (1996) 10508.
182. J. SCHNEIDER, U. KAUFMANN, W. WILKENING, M. BAEUMLER and F. KOHL, *Phys. Rev. Lett.* **59** (1987) 240.
183. R. Y. KOROTKOV, J. M. GREGIE and B. W. WESSELS, *Physica B* **308-310** (2001) 30.
184. *Idem.*, *Appl. Phys. Lett.* **80** (2002) 1731.
185. T. GRAF, M. GJUKIC, M. HERMANN, M. S. BRANDT, M. STUTZMANN and O. AMBACHER, *Phys. Rev. B* **67** (2003) 165215.
186. N. S. AVERKIEV, A. A. GUTKIN, N. M. KOLCHANOVA and M. A. RESHCHIKOV, *Fiz. Tekh. Poluprovodn.* **18** (1984) 1629 [*Sov. Phys. Semicond.* **18** (1984) 1019].
187. K. W. EDMONDS, N. R. S. FARLEY, T. K. JOHAL, R. P. CAMPION, B. L. GALLAGHER, C. T. FOXON and G. VAN DER LAAN, *J. Appl. Phys.* **95** (2004) 7166.
188. A. WOLOS, A. WYSMOLEK, M. KAMINSKA, A. TWARDOWSKI, M. BOCKOWSKI, I. GRZEGORY, S. POROWSKI and M. POTEMSKI, *Phys. Rev. B* **70** (2004) 245202.
189. R. Y. KOROTKOV, J. M. GREGIE and B. W. WESSELS, *Mat. Res. Soc. Symp. Proc.* **639** (2001) G3.7.
190. M. A. RESHCHIKOV, F. SHAHEDIPOUR, R. Y. KOROTKOV, B. W. WESSELS and M. P. ULMER, *J. Appl. Phys.* **87** (2000) 3351.
191. D. S. MCCLURE, *Solid State Phys.* **9** (1954) 488.
192. O. GELHAUSEN, E. MALGUTH, M. R. PHILLIPS, E. M. GOLDBY, M. STRASSBURG, A. HOFFMANN, T. GRAF, M. GJUKIC and M. STUTZMANN, *Appl. Phys. Lett.* **84** (2004) 4514.
193. B. HAN, R. Y. KOROTKOV, B. W. WESSELS and M. P. ULMER, *ibid.* **84** (2004) 5320.
194. B. HAN, B. W. WESSELS and M. P. ULMER, *ibid.* **86** (2005) 042505.
195. U. GERSTMANN, A. T. BLUMENAU and H. OVERHOF, *Phys. Rev. B* **63** (2001) 075204.
196. A. Y. POLYAKOV, N. B. SMIRNOV, A. V. GOVORKOV, N. Y. PASHKOV, J. KIM, F. REN, M. E. OVERBERG, G. THALER, C. R. ABERNATHY, S. J. PEARTON and R. G. WILSON, *J. Appl. Phys.* **92** (2002) 3130.
197. I. Y. YOON, T. W. KANG, M. C. JEONG, M. H. HAM and J. M. MYOUNG, *Appl. Phys. Lett.* **85** (2004) 4878.
198. R. HEITZ, P. MAXIM, L. ECKEY, P. THURIAN, A. HOFFMANN, I. BROSER, K. PRESSEL and B. K. MEYER, *Phys. Rev. B* **55** (1997) 4382.
199. J. BAUR, K. MAIER, M. KUNZER, U. KAUFMANN and J. SCHNEIDER, *Appl. Phys. Lett.* **65** (1994) 2211.
200. M. HASHIMOTO, H. TANAKA, R. ASANO, S. HASEGAWA and H. ASAH, *ibid.* **84** (2004) 4191.
201. L. M. CORLISS, N. ELLIOTT and J. M. HASTINGS, *Phys. Rev.* **79** (1950) 350.
202. U. HAUSSELMANN, P. VIKLUND, M. BOSTROM, R. NORRESTAM and S. I. SIMAK, *Phys. Rev. B* **63** (2001) 125118.
203. K. INUMARU, H. OKAMOTO and S. J. YAMANAKA, *J. Cryst. Growth.* **237-239** (2002) (2050).
204. T. TAKEUCHI, M. TAGUCHI, Y. HARADA, T. TOKUSHIMA, Y. TAKATA, A. CHAINANI, J. KIM, H. MAKINO, T. YAO, T. TSUKAMOTO, S. SHIN and K. KOBAYASHI, *Jpn. J. Appl. Phys.* **44** (2005) L153.
205. R. K. SINGH, STEPHEN Y. WU, H. X. LIU, LIN GU, D. J. SMITH and N. NEWMAN, *Appl. Phys. Lett.* **86** (2005) 012504.
206. S. G. YANG, A. B. PAKHOMOV, S. T. HUNG and C. Y. WONG, *ibid.* **81** (2002) 2418.
207. A. Y. POLYAKOV, N. B. SMIRNOV, A. V. GOVORKOV, N. V. PASHKOVA, A. A. SHLENSKY, S. J. PEARTON, M. E. OVERBERG, C. R. ABERNATHY, J. M. ZAVADA and R. G. WILSON, *J. Appl. Phys.* **93** (2003) 5388.
208. A. OIWA, A. ENDO, S. KATSUMOTO, Y. IYE, H. OHNO and H. MUNEKATA, *Phys. Rev. B* **59** (1999) 5826.
209. U. SIVAN, O. ENTIN-WOHLMAN and Y. IMRY, *Phys. Rev. Lett.* **60** (1988) 1566.
210. Y. ZHANG and M. P. SARACHIK, *Phys. Rev. B* **43** (1991) 7212.
211. N. TERAGUCHI, A. SUZUKI, Y. NANISHI, Y.-K. ZHOU, M. HASHIMOTO and H. ASAH, *Solid State Commun.* **122** (2002) 651.
212. T. MARUYAMA, S. MORISHITA, H. KAGATSUME, Y. NANISHI and K. AKIMOTO, IPAP Conference Series **1** (2000) p.482 (Proceeding of the International Workshop on Nitride Semiconductors, Institute of Pure and Applied Physics, Tokyo, 2000).
213. P. JUNOD, A. MENTH and O. VOGT, *Phys. Kondens. Materie* **8** (1969) 323.
214. R. CONSIGLIO, D. R. BAKER, G. PAUL and H. E. STANLEY, *Physica A* **319** (2003) 49.
215. S. A. WOLF, D. D. AWSCHALOM, R. A. BUHRMAN, J. M. DAUGHTON, S. VON MOLNÁR, M. L. ROUKES, A. Y. CHTELKANNOVA and D. M. TREGER, *Science* **294** (2001) 1488.
216. R. M. STROUD, A. T. HANBICKI, Y. D. PARK, G. KIOSEOGLOU, A. G. PETUKHOV, B. T. JONKER, G. ITSKOS and A. PETROU, *Phys. Rev. Lett.* **89** (2002) 166602.
217. S. DATTA and B. DAS, *Appl. Phys. Lett.* **56** (1990) 665.
218. YU. BYCHKOV and E. L. RASHBA, *J. Phys. C* **17** (1984) 6093.
219. V. I. LITVINOV, *Phys. Rev. B* **68** (2003) 155314.
220. S. HAO, G. ZHOU, J. WU, W. DUAN and B.-L. GU, *ibid.* **69** (2004) 113403.
221. K. SATO and H. KATAYAMA-YOSHIDA, *Mat. Res. Soc. Symp. Proc.* **666** (2001) F4.6.
222. H. OHNO, D. CHIBA, F. MATSUKURA, T. OMIYA, E. ABE, T. DIETL, Y. OHNO and K. OHTANI, *Nature* **408** (2000) 944.
223. R. FIEDERLING, M. KEIM, G. REUSCHER, W. OSSAU, G. SCHMIDT, A. WAAG and L. W. MOLENKAMP, *ibid.* **402** (1999) 787.
224. Y. OHNO, D. K. YOUNG, B. BESCHOTEN, F. MATSUKURA, H. OHNO and D. D. AWSCHALOM, *ibid.* **402** (1999) 790.
225. I. A. BUYANOVA, M. IZADIFARD, W. M. CHEN, J. KIM, F. REN, G. THALER, C. R. ABERNATHY, S. J. PEARTON, C. PAN, G. CHEN, J. CHYI and J. M. ZAVADA, *Appl. Phys. Lett.* **84** (2004) 2599.
226. A. Y. POLYAKOV, N. B. SMIRNOV, A. V. GOVORKOV, J. KIM, F. REN, M. E. OVERBERG, G. T. THALER, C. R. ABERNATHY, S. J. PEARTON, C.-M. LEE, J.-I. CHYI, R. G. WILSON and J. M. ZAVADA, *Solid-State Electron.* **47** (2003) 963.
227. A. Y. POLYAKOV, A. V. GOVORKOV, N. B. SMIRNOV, N. Y. PASHKOVA, G. T. THALER, M. E. OVERBERG, R. FRAZIER, C. R. ABERNATHY, S. J. PEARTON, JIHYUN KIM and F. REN, *J. Appl. Phys.* **92** (2002) 4989.
228. A. Y. POLYAKOV, N. B. SMIRNOV, A. V. GOVORKOV, J. KIM, F. REN, M. E. OVERBERG, G. T. THALER, R. M. FRAZIER, C. R. ABERNATHY, S. J. PEARTON, I. A. BUYANOVA, G. Y. RUDKO, W. M. CHEN, C. C. PAN, G. T. CHEN, J.-I. CHYI and J. M. ZAVADA, *J. Electron. Mater.* **33** (2004) 241.
229. I. A. BUYANOVA, M. IZADIFARD, L. STORASTA, W. M. CHEN, J. KIM, F. REN, G. THALER, C. R. ABERNATHY, S. J. PEARTON, C.-C. PAN, G.-T. CHEN, J.-I. CHYI and J. M. ZAVADA, *ibid.* **33** (2004) 467.
230. I. A. BUYANOVA, J. P. BERGMAN, W. M. CHEN, G. THALER, R. FRAZIER, C. R. ABERNATHY, S. J. PEARTON, J. KIM, F. REN, F. V. KYRYCHENKO,

- C. J. STANTON, C.-C. PAN, G.-T. CHEN, J.-I. CHYI and J. M. ZAVADA, *J. Vac. Sci. Technol. B* **22** (2004) 2668.
231. M. TANAKA and Y. HIGO, *Phys. Rev. Lett.* **87** (2001) 26602.
232. D. J. MONSMA, R. VLUTTERS and J. C. LODDER, *Science* **281** (1998) 407; R. SATO and K. MIZUSHIMA, *Appl. Phys. Lett.* **79** (2001) 1157.
233. B. DAS, S. DATTA and R. REIFENBERGER, *Phys. Rev. B* **41** (1990) 8278.
234. G. DRESSELHAUS, *Phys. Rev.* **100** (1955) 580.
235. B. BESCHOTEN, E. JOHNSON-HALPERIN, D. K. YOUNG, M. POGGIO, J. E. GRIMALDI, S. KELLER, S. P. DENBAARS, U. K. MISHRA, E. L. HU and D. AWSCHALOM, *Phys. Rev. B* **63** (2001) 121202.

*Received 24 March  
and accepted 30 May 2005*